From Single-Cell Migration to the Emergence of Collective Motion using Microstructured Surfaces

Felix J. Segerer

München 2016

From Single-Cell Migration to the Emergence of Collective Motion using Microstructured Surfaces

Felix J. Segerer

Dissertation
an der Fakultät für Physik
der Ludwig-Maximilians-Universität
München

vorgelegt von
Felix J. Segerer
aus München

München, den 29. Juni 2016

Erstgutachter: Prof. Dr. Joachim O. Rädler

Zweitgutachter: Prof. Dr. Erwin Frey

Tag der mündlichen Prüfung: 1. August 2016

ZUSAMMENFASSUNG

Zellmigration ist ein essenzieller Prozess in der Entwicklung und Erhaltung vielzelliger Organismen. Ein tiefgreifendes Verständnis der involvierten Mechanismen und phänomenologischen Charakteristika ist folglich von zentralem Interesse für die Zellforschung. Allerdings ist die involvierte Maschinerie komplex, was sich in Bewegungsmustern wiederspiegelt, die schon für vereinzelte Zellen schwer zu fassen sind. Zusätzlich führen auf der Skala größerer Zellansammlungen Interaktionsmechanismen, deren genaue Funktionsweise noch nicht geklärt ist, zu langreichweitigen Korrelationen und vielfältigen kollektiven Phänomenen in den Bewegungsmustern.

Eine Möglichkeit diese Komplexität im Experiment herunterzubrechen bietet die räumliche Begrenzung der Migration durch Mikrostrukturierung. Durch die Wahl geeigneter Strukturgeometrien können auf diese Weise die Freiheitsgrade der Zellen so eingeschränkt werden, dass spezifische Merkmale der Zellmigration gezielt adressiert und untersucht werden können. Zusätzlich können mit geeigneten Techniken weite Oberflächenbereiche strukturiert werden, was die automatisierte und parallelisierte Auswertung großer Anzahlen standardisierter Einzelexperimente ermöglicht. Im Zuge dieser Arbeit wurden daher neue Verfahren zur Mikrostrukturierung entwickelt und verwendet, um Einzelzellmigration wie auch die Interaktion kleiner Zellgruppen systematisch zu untersuchen.

Die hier entwickelte Mikrostrukturierungsmethode, genannt “microscale plasma-induced protein patterning” (µPIPP), ist einfach in der Anwendung und produziert homogene Proteinstrukturen auf verschiedenen biokompatiblen Oberflächen wie Glas, Zellkultur Polystyrol, Cyclo-Olefin-Copolymeren, und Parylen C. Darüber hinaus wurde das µPIPP-Protokoll erweitert, um die Generierung von oberflächengebundenen Proteingradienten sowie Strukturen bestehend aus mehreren Proteinkomponenten zu ermöglichen.

Um das Migrationsverhalten von Einzelzellen zu untersuchen, wurden ringförmige Mikrostrukturen verwendet. Im Kontrast zu klassischen Beschreibungen der Zellmigration zeigte die quasi-eindimensionale Bewegung der Zellen in diesen Systemen ausgeprägte Bimodalität, alternierend zwischen Phasen persistenter Migration und Phasen der Zufallsbewegung. Durch Einführung eines Algorithmus’ zum Erfassen charakteristischer Änderungen im Migrationsverhalten wurden die typischen Lebensdauern beider Zustände bestimmt. Zusammen mit der Zellgeschwindigkeit im persistenten Zustand ergaben diese einen charakteristischen Parametersatz um das Bewegungsverhalten einer Zelle zu beschreiben. Durch das Einbinden einer zellabweisenden Barriere in das System wurde dieser noch um die Umkehrwahrscheinlichkeiten in Abwesenheit und Anwesenheit chemischer Grenzflächen erweitert. Zusammengenommen wurden diese fünf Parametern gleich einem Fingerabdruck des Migrationsverhaltens einer Zelle verwendet, um die Bewegungsmuster von Zelltypen verschiedener Invasivität und den Effekt verschiedener Pharmazeutika auf diese detailiert zu charakterisieren und zu quantifizieren. Die verwendete Untersuchungsmethode gibt somit ein umfassendes Bild des Migrationsverhaltens von Einzelzellen und hat zudem Potential im Hinblick auf die Entwicklung eines Standardverfahrens zur vergleichenden Analyse von Zellmotilität in Zellbiologie und Pharmakologie.

In einer zweiten Versuchsanordnung wurde das Auftreten kollektiven Verhaltens in der Migration kleiner Zellgruppen untersucht. Hierfür wurden kreisförmige Mikrostrukturen von verschiedenem Durchmesser eingesetzt, in welchen kollektive Bewegung in der Form kohärenter Rotation aller Zellen innerhalb einer Kreisstruktur auftritt. Die Zellbewegung innerhalb der Systeme wurden in Abhängigkeit der enthaltenen Zellenanzahl untersucht, wobei immer sowohl Phasen kohärenter Rotation als auch Phasen ungeordneter Bewegung zu beobachten waren. Die Persistenz der Rotationszustände stieg dabei zwar generell mit steigender Zellenzahl an, dieser Trend wurde jedoch durch einen starken Abfall der Persistenz zwischen Systemen mit vier und Systemen mit fünf Zellen unterbrochen. Das Auslesen der relativen Zellpositionen innerhalb der Einzelsysteme zeigte, dass dieser Abfall mit einer Veränderung der Zellkonformation einherging. Numerische Simulationen basierend auf dem zellulären Potts-Modell, welche sowohl intrazelluläre Polarisation als auch interzelluläre Koppelung durch Mechanotransduktion berücksichtigen, reproduzierten diese Ergebnisse und lassen somit den Schluss zu, dass das Wechselspiel von relativer räumlicher Anordnung und der Ausrichtung der internen Polarisationsachsen benachbarter Zellen die Lebensdauer kollektiver Rotationszustande in der Zellmigration bestimmt. Die Untersuchung der verschiedenen Bewegungszustände innerhalb der Mikrostrukturen gibt somit Einblick in die, der kollektiven Zellbewegung zugrundeliegenden, Interaktionsmuster.

Zusammengefasst liefern die Ergebnisse dieser Arbeit somit tiefere Erkenntnis über den Prozess der Zellmigration und stellen einen weiteren Schritt dar, Mikrostrukturierung als Standardverfahren zur Analyse und Quantifizierung von Zellbewegung zu etablieren.

SUMMARY

Cell migration is a fundamental process that is essential for the development, maintenance, and functionality of multicellular organisms. A detailed understanding of the underlying mechanisms and phenomenological characteristics of cell migration is hence of central interest in life sciences. However, the bio-mechanical machinery propelling the cell is highly complex and its emergent migration patterns are difficult to grasp, even in the case of individually migrating cells. Additionally, at the scale of multi-cellular assemblies, interaction mechanisms that are not entirely understood result in long-ranged correlations and a rich set of collective phenomena in cell motion.

A possible approach to break down this complexity is to restrict cell adhesion and migration to predefined areas by using micropatterning techniques. By choosing suitable pattern geometries, the degrees of freedom of the confined cells can be diminished so that specific features of cell migration can be addressed and studied selectively. Furthermore, micropatterning techniques allow to create large arrays of standardized microenvironments, thereby enabling the automated analysis of multiple experimental systems in parallel. In the course of this work, micropatterning techniques were developed and employed to systematically study single-cell migration and the emergence of collective motion in small cell assemblies.

The developed micropatterning technique termed "microscale plasma-induced protein patterning" (µPIPP) is easy to implement and produces homogeneous protein patterns on various biocompatible substrates such as glass, tissue culture polystyrene, cyclic olefin copolymers, and parylene C. Moreover, the µPIPP protocol was extended to enable the formation of surface-bound protein gradients as well as of pattern designs featuring multiple proteins.

Utilizing the controlled environment provided by micropatterning, we studied single-cell migration within arrays of ring-shaped microlanes. In contrast to conventional descriptions of cell migration, the resulting quasi-one-dimensional motion showed pronounced bimodality, exhibiting states of directionally persistent migration ("run states") as well as states of localized erratic motion ("rest states"). Applying a change-point analysis based on cumulative sum statistics, the lifetimes of both states were identified to be exponentially distributed. The corresponding characteristic persistence times together with the cell velocity in the run state provided a set of parameters characterizing cell motion. By introducing cell-repellent barriers of different width into the setup, this parameter set was extended by quantifying the turning probability both in the presence and in the absence of chemical barriers. Similar to a migrational "fingerprint", these five phenomenological measures were used to thoroughly quantify and compare the migration behavior of different cell types as well as the effect of different pharmaceutics. The corresponding results illustrate that micropattern-based assays in combination with detailed, multi-parameter assessment of cell motion have potential applications in

cell biology as well as in sophisticated drug screening.

In a second assay, the emergence of collective behavior in the motion of small cell assemblies was studied. As pattern geometry, we chose circles of different diameters, in which collective migration manifests in form of a coherent angular motion (CAMo) of the confined cells. Analyzing the dynamics in dependence on the number of cells, N, within a system, periods of CAMo as well as periods of disordered motion (DisMo) were identified. Both states showed exponential lifetime distributions. The persistence of CAMo was found to increase with N but exhibited a pronounced discontinuity between systems containing four and systems containing five cells. An assessment of the cell conformations within the patterns revealed that this discontinuity was accompanied by a geometric rearrangement of cells towards a configuration containing a central cell. Numerical simulations, which are based on the cellular Potts model and account for intracellular polarization as well as intercellular coupling via mechanotransduction, reproduced these features and hence confirmed our finding that the persistence of rotational states depends on the interplay of spatial arrangement and internal polarization of neighboring cells. The distinct migration states within confined environments hence provides significant insights into the local interaction rules guiding collective migration.

Taken together, the results of this thesis shed new light on the process of cell migration and illustrate how the controlled and standardized microenvironments provided by micropatterning techniques can be used to systematically assess and examine cell migration on a quantitative basis. Furthermore, the introduced techniques and assays are a step towards establishing micropatterning as a standard tool for cell science.

CONTENTS

CHAPTER 1

INTRODUCTION

Cells are the basic building blocks of all known living organisms. Their inherent complexity and versatility in form and function provides the foundation for the diversity of life itself. Among the great number of different cell functions, one of the most important is a cell's ability to propel itself. This process, called cell migration, is not only found in bacteria and other unicellular life forms, but is also an essential process for the development, the maintenance, and the functionality of multi-cellular organisms. In fact, its respective manifestations range from the individual migration of cells in processes like immune response[1,2] or the development of the nervous system[3,4] to the multi-cellular motion involved in processes like morphogenesis[5–8], tissue repair[9,10], or cancer growth[11,12]. A detailed understanding of the underlying mechanisms, as well as of the phenomenological characteristics of cellular migration is hence of central interest in life sciences.

However, the bio-mechanical machinery propelling the cell is a highly complex system and its emergent migration patterns are difficult to predict. This applies already to the migration of individual cells, for which the observed motion patterns depend on the cell type, on cell-internal switches with regards to gene expression levels, as well as on their surrounding environment.[13–17] On the scale of multi-cellular assemblies and tissues, this complexity is not diminished. On the contrary, the interactions between adjacent cells induce a rich set of collective phenomena, exhibiting correlation lengths of several cell sizes[18–20] and it still remains unclear how such collectivity emerges from the rather erratic motion observed for individually migrating cells.

Due to this inherent complexity, a multitude of different theoretical models aiming to describe and to understand the process of cell migration have been proposed over the last years. In order to grasp the migration machinery of individual cells as well as the collective motion within large assemblies and tissues, these approaches cover multiple levels of complexity. The different implementations hence range from models based on the description of sub-cellular processes like intracellular reaction diffusion dynamics[21–24] to coarse grained approaches in which individual cells are represented by simple, self-propelled geometrical objects following specific sets of interaction rules[25–27]. Many of these models are able to reproduce certain features of the migration process. However, in order to find suitable parameter sets for these models, to test their predictive power, and to finally gain a more comprehensive understanding of cell migration, the migration patterns emerging *in silico* need to be compared to experimental observations. To this end, cell migration needs to be assessed and characterized on a quantitative basis.

In addition, such an assessment of cell migration holds the advantage that once characterized, deviations from the typical migration behavior of a cell type can be detected and quantified. Since such deviations often indicate either pathological conditions or the effect of applied pharmaceutics, their detailed characterization and interpretation are of great interest for life sciences.

However, to find suitable metrics describing and quantifying cell migration is a challenging task. On the one hand, this is because the migration patterns described by individual cells as well as by collectively moving assemblies are quite complex and not easy to capture. On the other hand, this is due to the fact that the heterogeneities within cell populations and the liability of cellular behavior to subtle changes in the surrounding environment demand high statistical sample sizes to draw significant conclusions.

A technique which has recently proven highly useful as an experimental method addressing both of these issues is surface functionalization in form of micropatterning. The basic idea behind this approach is to restrict cell adhesion and migration to predefined parts of a surface, while other surface parts are rendered cell-repellent. This way reducing the degrees of freedom in cell motion, the rich phenomena emerging cellular migration can be broken down and, by choosing appropriate pattern geometries, particular features of cellular behavior can be addressed and studied more specifically. Furthermore, micropatterning techniques allow to create large arrays of standardized microenvironments, thereby enabling the automated analysis of multiple microscopic experimental setups in parallel.

Due to these benefits, micropatterning techniques have found widespread application in cell research. Over the last years, a variety of different pattern geometries has been applied to study phenomena such as gene expression[28], the emergence and orientation of the axes of cell polarization, division, and coupling[29–33], as well as the migration of single cells[13,34–37] and collectively migrating cell assemblies[38–40]. In the context of locomotion of single cells, narrow lane patterns have proven useful, as they virtually restrict cell motion to one dimension and hence facilitate the assessment of migration-related measures. These benefits enabled the automated analysis and comparison of the migration behavior of great numbers of different cell types.[13,40–42] In the field of collective migration, the confinement of cell assemblies into micropatterns of circular shape has been shown to induce the emergence of a coherent angular motion of all cells within the pattern.[43–45] Since the circular pattern geometry largely restricts collective motion to this coherent rotation, the emergence and decay of collectivity in such systems is more easy to capture than for unconfined cell layers. Both of these examples hence show how the restriction provided by a suitable micropattern geometry can serve to break down the complex behavior of migrating cells such that characteristic properties and measurable parameters can more readily be extracted. However, despite these benefits, micropatterning approaches have not yet established as a standardized and easily accessible tool in cell research. Partly, this is due to the fact that many of the techniques in the field are tricky to implement, require advanced equipment, or are very limited with regards to the achievable pattern designs. To another part, this is due to the fact that there is still a lack of standardized pattern assays and corresponding data evaluation approaches.

The focus of this thesis is twofold. Firstly, it aims to increase the accessibility and versatility of micropattern assays in cell science by introducing a new, versatile, and easy to handle patterning technique. Secondly, micropattern-based assays are employed to systematically study the process of cell migration in the form of single-cell motion as well as in the form of the collective migration of small cell assemblies.

The thesis is hence organized as follows:
In **Chapter 2**, the fundamental concepts behind cell migration and micropatterning assays are introduced. Therefore, the major components involved in the migration of eukaryotic cells are described and the basic mechanism of the migration machinery is discussed. Furthermore, the chapter gives a brief introduction into the different micropatterning approaches as well as in theoretical descriptions of cell motion.
In **Chapter 3**, microscale plasma-induced protein patterning (µPIPP), a novel technique for micropatterning that was developed in the course of this thesis, is introduced and discussed. It is shown that the method produces homogeneous patterns of controlled protein density, which are able to confine cells on various substrates such as glass, tissue culture polystyrene, cyclic olefin copolymers, and parylene C. Furthermore, it is illustrated that the technique can be extended to allow the formation of surface bound protein gradients as well as of patterns composed of multiple proteins.
Chapter 4 introduces ring-shaped micropatterns as an assay to characterize and quantify single-cell migration and the interaction with chemical interfaces. In a first set of experiments, cell migration on circular lanes is analyzed and found to exhibit distinct periods of directed migration (run states) interrupted by periods of reorientation (rest states). Applying a classification scheme dissecting these periods based on a change-point analysis, the lifetimes of both states are found to be exponentially distributed, revealing characteristic persistence times. In a second set of experiments, chemical barriers of different width are introduced into the setup and their effect on cell migration is evaluated. Upon an encounter with the interface, the probability for a cell to overcome the obstacle is found to decrease exponentially with the width of the corresponding barrier. Taken together, the experimental assay yields five parameters characterizing single-cell migration similar to a “migratory fingerprint”. This characterization scheme is applied to compare the migration of different cell types as well as to analyze the effects of different pharmaceutics on cell migration.
In **Chapter 5**, circular micropatterns are introduced to study the emergence and persistence of collective migration in form of coherent rotational motion as a function of the number of confined cells. Analyzing cell tracks within systems containing two to eight cells, distinct

states of disordered motion (DisMo) and coherent angular motion (CAMo) are revealed. The lifetimes of both states are found to be exponentially distributed. The typical persistence time of the CAMo state increases with cell number but shows a pronounced drop between systems containing four and systems containing five cells. By comparing the experimental results to numerical simulations, this drop in persistence can be attributed to a change in the topological arrangement of the cells within the system, hence revealing the decisive role of the interplay between the local arrangement of neighboring cells and the internal cell polarization in collective migration. **Chapter 6** summarizes the major ideas and results of this thesis and discusses their impact and potential applications in the field of cell science. Furthermore, suggestions for possible future experiments based on the results of this thesis are made. Finally, in the supplementary **Chapter A**, additional information and detailed descriptions of the applied experimental methods as well as of the data analysis and modeling approaches are given.

CHAPTER 2

FUNDAMENTAL CONCEPTS

2.1. STRUCTURE AND MAJOR COMPONENTS OF LIVING CELLS AND TISSUES

The process of cell migration involves the coordinated interplay of a multitude of different components and pathways. The major players and concepts involved in this complex machinery will be introduced in this section.

2.1.1. THE CYTOSKELETON

The physical properties and mechanical functions of living cells are to large degree governed by the cytoskeleton. Although the term “skeleton” suggests a rigid and changeless structure, the cytoskeleton is in fact a highly dynamic network, that is built up and degraded continuously within the cell. Thereby, the cytoskeleton fulfills a great variety of functions. The major part of these functions can roughly be categorized into three general tasks: (i) spatial organization of cellular contents, (ii) rendering the cell sensible to external stimuli by connecting it physically as well as biochemically to its environment, and (iii) generating the mechanical forces that are necessary to establish, change, and maintain the shape of a cell as well as for the process of cell migration.[46] Structurally, the cytoskeleton is composed of three types of protein filaments, each of whom is assembled from different monomers.

MICROTUBULES

With a diameter of about 32 nm, microtubules are the thickest and stiffest among the filaments of the cytoskeleton. As illustrated in Figure 2.1, the actual filaments are composed of globular proteins called α- and and β-tubulin. During assembly, α/β-tubulin dimers polymerize in a head-to-tail fashion, forming linear protofilaments. Subsequently, 13 of these protofilaments associate laterally to form a hollow tube, the actual microtubule. Since the protofilaments associate in a slightly shifted manner, a helical structure exhibiting a lead of about 8 nm emerges. As a consequence of the parallel alignment of the tubulin dimers, microtubules are polar structures showing different growth and degradation rates at both ends of the filament.[47] The faster-growing end is called the plus end whereas the slower-growing end is referred to as the minus end. The filaments are mainly nucleated and organized by so-called microtubule-organizing centers (MTOCs) such as the basal bodies and the centrosomes.[48]

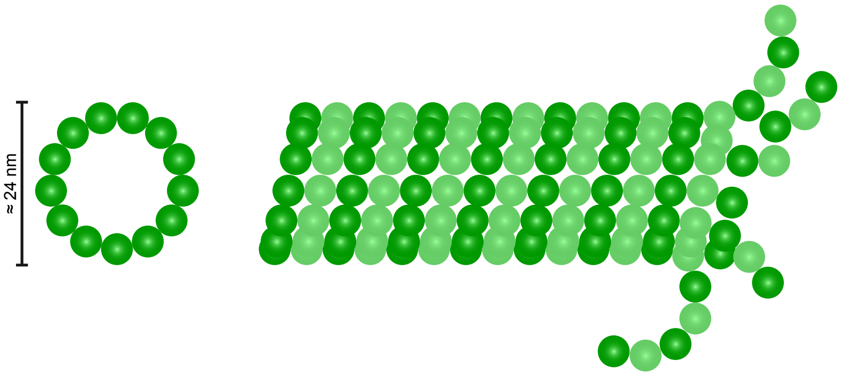

FIGURE 2.1.: Schematic illustration of the microtubule structure. Tubulin dimers assemble head-to-tail to form linear protofilaments. Subsequently, 13 of these protofilaments associate laterally to form the helical microtubule.

Microtubules are formed in all eukaryotic cells that are able to divide and in most differentiated cell types. As they build the mitotic spindle apparatus and provide the pathways for a large variety of different molecular motors, they play a key role in cell division as well as in intracellular transport. Also, the flagella and cilia used to propel eukaryotic cells contain bundles of microtubules.[49] Furthermore, microtubules are essential for the process of cell migration as they are directly involved in providing and maintaining cell polarization and orchestrate actin assembly.[50–52]

INTERMEDIATE FILAMENTS

As their name indicates, intermediate filaments have a diameter of about 10 nm which is in between that of the thicker microtubules and that of the thinner actin filaments. Intermediate filaments consist of elongated monomers which assemble to dimers in a coiled coil fashion, as illustrated in Figure 2.2. Two of such dimers then assemble in an antiparallel fashion to form staggered tetramers. These tetramers provide the building blocks of the elongated protofilaments, about eight of which pack together in a rope-like structure to form the actual intermediate filament.[53,54] In contrast to microtubules and actin filaments, intermediate filaments are non-polar, since the tetramers are assembled in an antiparallel fashion.

Due to their rope-like structure, intermediate filaments are rather robust and elastic and hence often are a key player in providing physical strength to cells and tissues. In doing so, intermediate filaments appear in various forms. While desmins stabilize the arrangement of

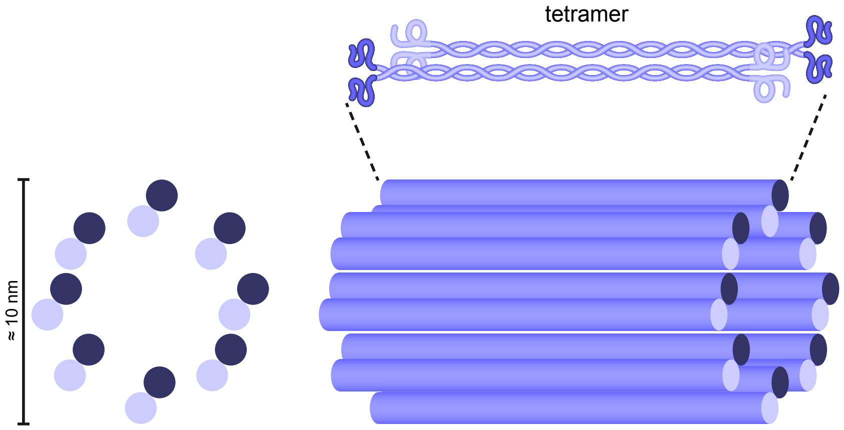

FIGURE 2.2.: Schematic illustration of the intermediate-filament structure. The elongated monomers assemble in a coiled coil fashion into polar dimers, which in turn assemble in an antiparallel fashion building non-polar tetramers. Around eight of these tetramers assemble in a rope-like structure, the actual intermediate filament.

muscle fibers, neurofilaments provide structural support for the axons of nerve cells. Another representative of intermediate filament building proteins are the nuclear lamins, which stabilize the cell nucleus and are involved in processes like mitosis and the positioning of nuclear pores.[53,54]

ACTIN FILAMENTS

With a diameter of about 8 nm, actin filaments are the thinnest among the filaments of the cytoskeleton. Similarly to microtubules, actin filaments are composed of globular proteins. As illustrated in Figure 2.3, these globular monomers, the so-called G-actins, assemble together to build the helical structure of the filament, the so-called F-actin. Since the G-actins are assembled in a head-to-tail fashion, actin filaments possess structural polarity, resulting in a slowly growing "pointed" (or (−)) end and a fast growing "barbed" (or (+)) end. Actin filaments are continually assembling and degrading in response to local intracellular signaling. If the growth at the barbed end is equaled by the degradation at the pointed end, the filament remains in a so-called steady treadmilling state. In this state, the overall length of the filament remains constant, but due to energetically favorable assembling and disassembling, force can be created. Although the individual actin filaments are much less rigid than microtubules actin filaments can build highly organized and stiff structures such as isotropic, bundled, or branched networks when tied together with crosslinking proteins.[46]

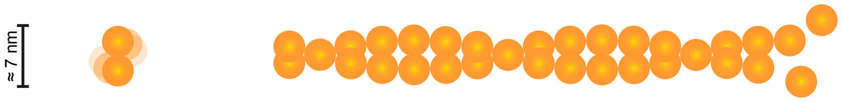

FIGURE 2.3.: Schematic illustration of the actin-filament structure. The actin filament is a polar, helical structure built by assembly of globular actin monomers.

Actin is one of the most abundant proteins in eukaryotes and is essentially found in all eukaryotic cells.[54] In form of the membrane attached actin cortex, it controls the shape of most eukaryotic cells lacking a cell wall. Furthermore, flexibility with regard to the structure of the crosslinked networks enables the actin cytoskeleton to support thin and needle-like protrusions like filopodia and nanotubes, as well as the broad flat lamellipodia at the leading edge of a migrating cell. Actin filaments are hence not only essential for processes like cell-substrate and cell-cell adhesion, but also play a key role in the process of cell migration. In this process, actin polymerization at the barbed end of the filaments generates the protrusive forces that push the membrane at the cell front.[55,56] Furthermore, in combination with actin-binding motor proteins, the myosins, actin filaments form the actomyosin machinery. This machinery provides the contractility of a cell and hence generates the forces that drag the cell body forward (see Section 2.2).[56]

2.1.2. THE EXTRACELLULAR MATRIX

Cells are highly sensitive objects, which dynamically adapt to and interact with their surrounding environment. In living tissue, this environment is not solely composed of other cells but consists to a large part of extracellular space. This space is to a great extent filled with a complex network of cell-secreted macromolecules, the so-called extracellular matrix (ECM). The ECM surrounds and supports cells in multiple ways, thereby often determining the physical properties of whole tissues. Variations in the concentration or orientation of the different molecular components of the ECM can change its physical characteristics drastically, resulting in a variety of different manifestations ranging from solid structures like bones or teeth to soft and transparent materials like the cornea.[53] In form of the basal lamina, the ECM also builds the substrate on which epithelial cells are sitting and migrating.

There are four major families of proteins which form the fibrous part of the ECM:

Collagens, the most abundant protein of the ECM, makes up to about 25 % of the mammal body mass, and is hence the most frequent protein in mammals.[53] Up to now, over 27 different types of collagen have been identified, of which the majority is of the fibrous form and fulfills functions like providing tensile strength, directing tissue development, and regulating cell adhesions.

Elastins, as the name indicates, are highly elastic proteins, which which provide many tissues with the ability to recoil after transient stretch. Elastin fibers are often found in tight association with collagens so that very flexible as well as stable matrices are formed.

Laminins are heterotrimeric proteins which play an important role in most tissues of living organisms. They are a major constituent of the basal lamina and directly involved in cell adhesion and migration.

Fibronectins are protein dimers found in all vertebrates. As they provide binding sites for different types of integrins, which are a transmembrane family of cell adhesion molecules (see Section 2.1.3), fibronectins, similar to collagens and laminins, are highly involved in cell-substrate adhesion and migration.[53,57,58]

Next to the fibrous proteins, the **proteoglycans** build another main class of macromolecules constituting the ECM. These molecules commonly consist of a core protein to which one or more long glycosaminoglycan chains are covalently attached. Proteoglycans are highly hydrophilic. High amounts of these molecules hence result in a hydrogel-like character of the ECM and therefore provide the corresponding tissues with resistance to compressive forces.[57]

2.1.3. THE PLASMA MEMBRANE

The plasma membrane is an integral component of living cells, separating the intracellular components from the extracellular environment. The membrane itself consists to a great part of phospholipids, which are characterized by a polar and hence hydrophilic head group, to which two hydrophobic fatty acid tails are attached. In aqueous environments, this amphiphilic character causes phospholipids to spontaneously assemble into lipid bilayers, which build the basis of the plasma membrane. As depicted in Figure 2.4, this structure enables proteins that also posses separated hydrophilic and hydrophobic regions to embed partly in or all through the membrane. If they are not connected to other intra- or extracellular components, these so-called integral or transmembrane proteins diffuse freely within the plane of the membrane. Furthermore, they are often specialized to fulfill specific tasks within the bilayer such as relaying signals or channeling molecules. Embedded with a great variety of such proteins, the plasma membrane hence becomes highly functional.

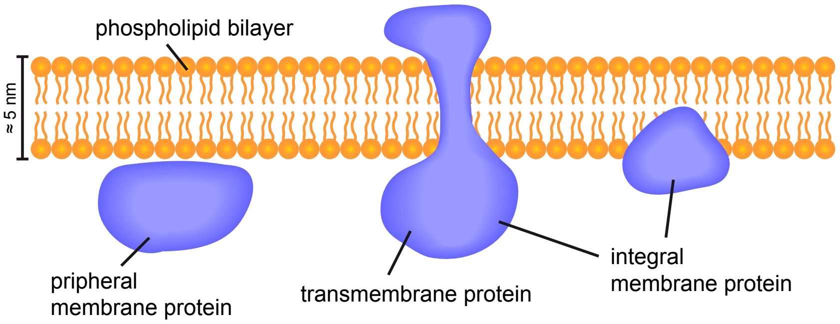

FIGURE 2.4.: Schematic illustration of the plasma membrane. Different types of membrane proteins are associated with the phospholipid bilayer.

From a mechanical point of view, the plasma membrane plays an important role in providing and maintaining the cell shape as well as in processes like cell-cell and cell-substrate adhesion and cell migration. Through different types of membrane proteins, the plasma membrane is able to anchor to the intracellular actin cortex as well as to extracellular components such as the membrane of other cells or the ECM.

One of the most important protein families in the context of cell-cell adhesion are the **cadherins**. These transmembrane adhesion proteins are able to link (directly or indirectly) to the cortical actin filaments as well as to other cadherins anchored in the membranes of neighboring cells. Once such a connection to another cell is established, the cadherin molecule, which originally was diffusing freely within the plasma membrane, becomes immobilized. Additionally, a rearrangement in the cytoskeleton is triggered by direct control of the activity of several actin regulators. This reorganization of the cortical actin filaments leads to an increase of the contact area between the cells and consequently to further cadherin connections, finally resulting in the formation of larger connecting complexes such as adherens junctions and desmosomes.[59]

A further family of transmembrane proteins, which is not only involved in cell-cell adhesion but is the principal receptor for binding the proteins of the ECM in the context of cell-substrate adhesion, are the **integrins**. Depending on the specific integrin type, the extracellular part of these proteins is able to bind to various ligands such as fibronectin, collagen, and laminin. As they are simultaneously attached to the intracellular actin cortex, integrins do not only work as linking proteins, but also transduce information from the ECM to the cell interior and back. Once an integrin molecule has bound to a ligand, a conformational change in the receptor can lead to further integrin assembling. This process can finally lead to the formation of so-called focal adhesions, which are large integrin clusters attaching the cell to the ECM.[56,58]

Since cadherin- and integrin-based cell junctions are mechanosensitve, both proteins are considered to be key players in the process of mechanotransduction, in which a cell converts external mechanical stimuli into cell-internal electrochemical activity (often represented by cytoskeletal activity).[60,61]

2.2. CELL MIGRATION

In the last section, the major players involved in the process of cell migration have been introduced. In this section, an outline on how these components work together to form the highly complex machinery propelling the cell will be given.

2.2.1. SINGLE-CELL MIGRATION

The initial step for the migration of a cell is its internal polarization. In this process, the cell builds up an intracellular signaling cascade that results in a symmetry break in the concentration and activity of cytoskeletal components and other related molecules, finally leading to the development of a leading and a tailing edge in the axis of motion.

During the process of polarization, the centrosome orients towards the leading edge, resulting in the formation of a polarized array of microtubules pointing towards the cell front. Since microtubules, as pathways for a large variety of different molecular motors, coordinate a great part of the intracellular molecule transport, the establishment of this array is thought to be an essential factor for the establishment and maintenance of cell polarity.[51,62] In addition, the dynamics of actin polymerization and depolymerization become highly anisotropic throughout the cell. While the tailing edge of the cell is characterized by increased actin depolymerization, actin is polymerized rapidly at the leading edge.

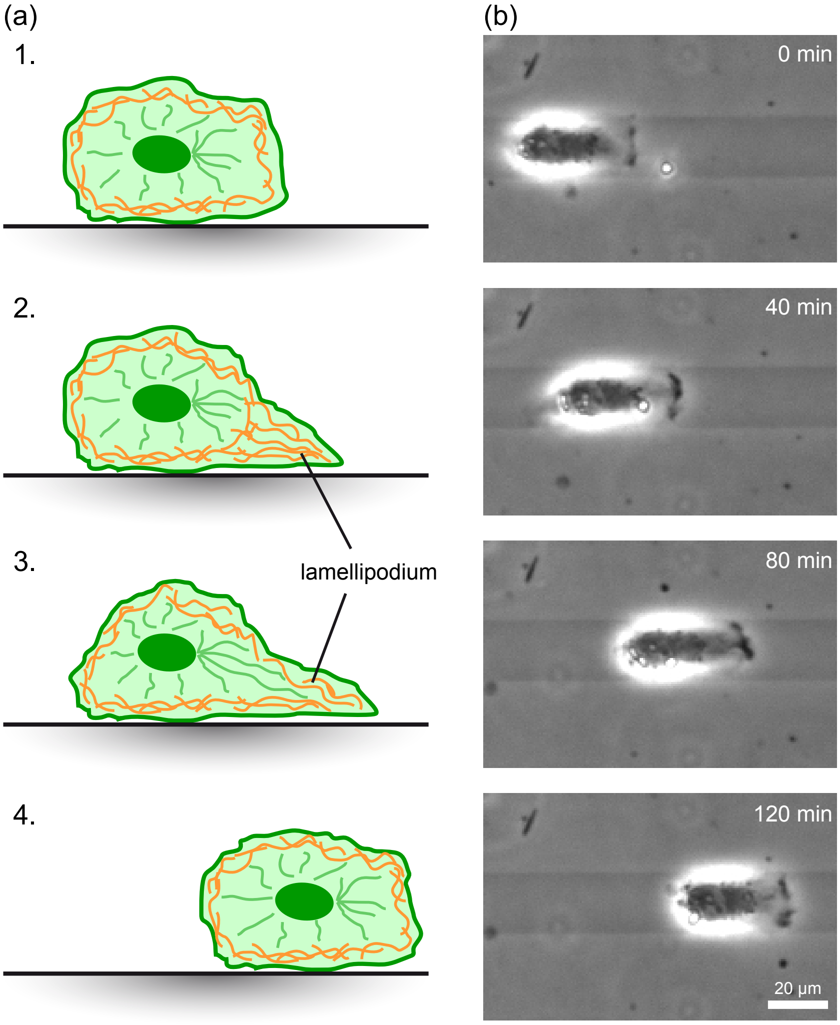

FIGURE 2.5.: The basic principle of cell migration. (a) Schematic, stepwise illustration of the migration process: 1. Cell before polarization and spreading. 2. Polarization and formation of a lamellipodium at the cell front. 3. Adhesion to the substrate at the cell front and depolymerization of actin at the rear. 4. Contraction and consequential displacement of the cell body. (b) Phase contrast images of a MDA-MB-436 cell migrating on a micropatterned stripe of 20 µm width.

As illustrated in Figure 2.5, the resulting process of locomotion can be explained with a stepwise model. In the first step, the asymmetry in the cytoskeletal activity, in particular the polymerization of actin at the cell front, leads to the generation of a protrusive force pushing the cell membrane at the leading edge. This results in the formation of protrusions such as lamellipodia and filopodia at the front edge of the cell. Once a lamellipodium is formed, integrins and other membrane-bound adhesion receptors link the actin cortex to the fibrous proteins of the underlying ECM, resulting in the formation of focal adhesions. Being attached to the substrate at the cell front, actomyosin-driven contraction of the cell in combination with depolymerization of actin at the tailing edge leads to detachment of substrate adhesions at the rear and finally to a displacement of the cell body.[53,56] It should be noted, however, that this stepwise model serves demonstrative purpose only. In Figure 2.5(b) microscopy images of a migrating MDA-MB-436 are shown. It becomes evident, that rather than one after another, the individual steps of migration are executed simultaneously and continuously as the cell moves along.

2.2.2. CELLULAR COLLECTIVITY

Many mammal cell types are not found as isolated cells within the organism but rather appear as part of larger cell assemblies or tissues. In various processes like morphogenesis[5–7], tissue repair[9,10], and cancer metastasis[12,63], the interconnected cells of such assemblies migrate coherently, showing spatially long-ranged correlations. This process is called collective cell migration.

To realize the long-ranged motion alignment involved in collective migration, in addition to the intracellular machinery of cell migration outlined in the last section, communication between the individual participating cells is required. Such intercellular signaling can be mechanical or chemical (or both) in nature. The mechanical part of the intercellular signaling is mostly transmitted via cadherin-based cell-cell junctions. Mechanically coupled by these junctions, a cell is able to adapt its motion to the pushing and pulling forces exerted by its neighbors. This mechanocoupling is known to be one of the key players driving collectivity in cell migration.[64–68] In addition to the direct mechanical coupling via cell-cell adhesions, intercellular forces can also be transmitted via deformations of the underlying substrate. In fact, substrate deformations have been found to be involved in mediating long-ranging mechanical coupling and hence in the coordination of collective cell migration.[19]

Intercellular chemical signals guiding collective migration can either be exchanged by soluble chemicals transmitted by the environmental solution or directly via junctions involved in cell-cell adhesions.[67,69,70] A well-known phenomenon emerging from the direct exchange of chemical signals is the process called “contact inhibition of locomotion” (CIL). Originally, CIL describes the observation that an individually migration cell halts its motion and/or changes migration direction after contact with another cell.[71,72] In recent years, however, it has not only been shown that collective migration and CIL can coexist[40], but it has been suggested that the very same signaling pathway involved in CIL also serves as a guiding mechanism driving the emergence of collective cell migration.[73]

By these means, cells are able to align their motion over distances exceeding several cell lengths.[18–20] The phenomena emerging from this collectivity are found to be rather complex and to depend on cell-type specific properties as well as on environmental conditions. A classical example for the heterogeneities possibly emerging in an initially homogeneous cell layer are the leader-follower dynamics resulting in “finger”-like outgrowth when monolayers of epithelial cells are presented to a free surface.[10,74] In the absence of free surface (or many cell rows behind), streaming patterns and vortices are typical migration patterns found in closed cell sheets.[39,75] Despite these highly dynamic features of cellular matter, it has been shown that an increase in cell density (or the maturation of cell-cell and cell-substrate junctions) can change the dynamics in a cell monolayer in a way similar to the amorphous solidification involved in glass transition.[20,76]

2.2.3. GUIDED CELL MIGRATION

The direction of the polarization and migration of a cell is not always of random orientation, but often results from asymmetries in the cell’s environment. In fact, depending on the cell type, migrating cells can be sensitive to a multitude of extracellular guidance cues. Such guidance cues can be represented by external electrical fields (electrotaxis, galvanotaxis)[77,78], gradients or asymmetries in the rigidity or structure of the underlying substrate (durotaxis, haptotaxis)[16,79], or by external forces (mechanotaxis)[80]. The most investigated guidance principle in cell migration, however, is chemotaxis. This process describes the emergence of directed motion in response to an external chemical stimulus. Prominent examples are the directed migration of endothelial cells in soluble gradients of vascular endothelial growth factor[81,82] or that of nerve growth cones in soluble gradients of neurotransmitters[83,84]. However, the chemical gradients inducing a directional bias in cell migration have not necessarily to be soluble. It has been shown that also gradients in the surface density of vascular endothelial growth factor or ECM proteins like collagen or fibronectin can induce chemotaxis.[85–88]

2.3. SURFACE FUNCTIONALIZATION IN CELL RESEARCH

Over the last decades, *in vitro* assays in the field of cell research have undergone considerable development. One aspect driving this development was the goal to mimic the highly complex environments that cells encounter *in vivo*. Another trigger was that a more complex microenvironment often allows to narrow down the specific question on cellular behavior and properties addressed by the experimental setup. The for this thesis most important experimental approaches addressing 2D cell migration are outlined in this section.

2.3.1. PROTEIN ADSORPTION

In order for a cell to migrate it needs to establish adhesions to the underlying substrate. *In vivo*, this substrate is often composed of the proteins of the ECM. As a consequence, most migrating cell types are specialized in migrating on ECM proteins. Hence, in order to provide conditions in favor of cell adhesion and migration, the glass or plastic surfaces used in cell experiments are often coated with ECM proteins like fibronectin, collagen, or laminin. This coating is mostly achieved via incubating the surface in a solution containing the desired protein. It has to be mentioned, however, that the conformation of proteins is likely to change when attaching to the substrate.[89–91] Such conformational changes possibly alter the accessible motives, like integrin binding sequences, of a protein and consequently may affect the adhesion behavior of cells on the corresponding protein layers.[92] For applications in which a more accurate control over the specific type of binding is essential, assays in which only specific binding motives are coated or the corresponding proteins are bound covalently with a defined orientation might therefore be more suitable.[93]

2.3.2. PATTERNING APPROACHES

Rather than tuning a surface globally for cell adhesion, so-called micropatterning techniques can be applied to achieve well-defined spatial arrangements of differently functionalized surface areas. Thereby, patterns composed of cell friendly areas and areas prohibiting cell adhesion can be created. Many of the common techniques in this field use a coating with ECM proteins for the adhesive parts of the surface, while cell repellence is often achieved via a coating with passivating polymers such as poly(ethylene-glycol) (PEG). The cushion-like arrangement of the PEG chains of such PEG layers thereby sterically hinders the adsorption of proteins and thus prevents cell adhesion.[94,95] The protocols for the formation of PEG layers are various. Due to its versatility and simple application, a common approach is the physisorption of block copolymers such as Pluronic or poly(l-lysine)-graft-poly(ethylene-glycol) (PLL-PEG) from solution. As depicted in Figure 2.6, these block copolymers consist of PEG chains which are linked to a poly(propylene-oxide) (PPO) (in the case of Pluronic) or poly(l-lysine) (PLL) (in the case of PLL-PEG) backbone. These polymers are available featuring different grafting ratios and chain lengths, which, depending on the used substrate, determines the quality of the resulting protein repellence of the corresponding monolayers.[94] For the applications, the main difference between both molecules is their affinity to different types of surfaces. While the non-polar PPO backbone of Pluronic binds via hydrophobic interaction to hydrophobic surfaces, the positively charged PLL backbone of the PLL-PEG molecule binds electrostatically to negatively charged surfaces.

Spatial control over the deposition of the adhesive and repulsive coating is achieved via a variety of different patterning protocols. Most patterning techniques used in cell sciences are based on one of the following three approaches:

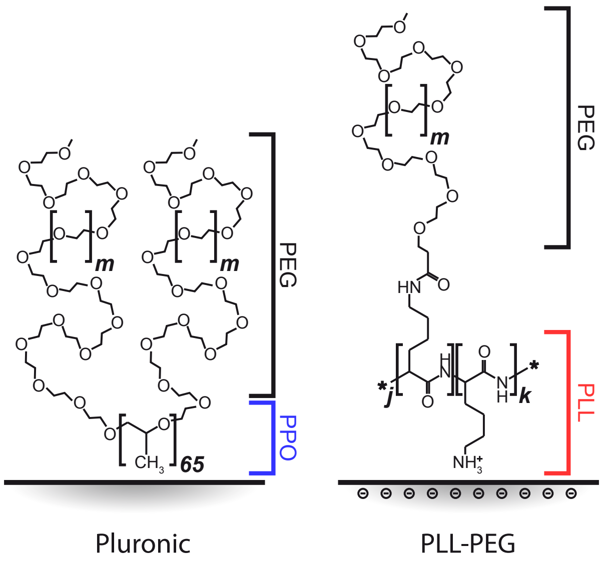

Figure 2.6.: Schematic illustration of the polymer architecture of Pluronic and PLL–PEG. (a) Pluronic consists of a 65-mer of PPO attached to two PEG chains. (b) PLL-PEG consists of a PLL chain of variable length to which PEG chains are linked. Dependent on the exact type, the number of lysine units per PEG chain is given by the grafting ratio. Both molecules are available featuring various PEG-chain lengths. Figure adapted with permission from Reference [96]. Copyrighted 2014 by WILEY-VCH Verlag GmbH & Co. KGaA, Weinheim.

In **soft lithography**, which is commonly used in form of microcontact printing (µCP), a polymeric stamp of the desired pattern is “inked” via incubation in a protein solution and afterwards brought into contact with a surface, thereby transferring the protein.[97–99] Subsequently, the remaining surface parts can be passivated using PEGylation. The main advantage of µCP is that it does not require advanced or expensive equipment and in most cases involves a relatively easy working procedure. On the downside, depending on the substrate and protein used, the transfer of the protein from the stamp to the surface can eventually be tricky to handle, resulting in no or only very inhomogeneous protein transfer.

Photolithography works via local alteration of the chemical properties of a surface or a precoated matrix (such as a PLL-PEG layer) by light-induced photocleavage. The actual pattern is generated using a laser writing device or illumination through a photomask.[100–103] Subsequently, adhesion proteins can be coated via adsorption from a protein solution. Since, in contrast to µCP, proteins are not transferred from a stamp but adhere from solution, photolithography-based protocols are able to produce very homogeneous patterns and can be extended to form gradients in the surface-bound protein density.[104] A drawback of approaches based on photolithography is, however, that in order to change substrate properties by illumination, they require either sophisticated photochemistry or high quality (deep UV permeable) photomasks or laser writing devices.

Finally, using **plasma induced patterning**, the surface is usually covered partially by a shadow mask or stamp of the desired pattern and subsequently exposed to plasma (e.g. oxygen), which changes the chemical properties of the exposed surface parts (e.g. by inclusion of ions).[105–110]

In some applications, proteins or passivation agents are subsequently attached to either the plasma-activated or the untreated parts of the surface. Plasma-based approaches hold the advantage that plasma activation is a robust and comparatively fast procedure that works on a multitude of different substrates. Furthermore, plasma activation can be exploited (i) directly to render an initially cell repellent surface accessible for cell adhesion[107,110], (ii) as a basis for the spatial control of adhesion or conformation of proteins or polymers[105,106], and (iii) to selectively remove parts of a protein or polymer layer[108,109]. Still, it has to be considered that the creation via a shadow mask or stamp makes certain pattern geometries (e.g. ring structures) not, or only very difficult, to accomplish.

Some of the patterning techniques used in cell sciences have been extended to enable the formation of patterns composed of more than two components (e.g. to incorporate different protein coatings). Mostly, such multi-component patterning is achieved by successively repeating the same patterning protocol several times, thereby preserving all previous patterning generations in each iteration of the protocol.[102,104,111–113] Although often providing the possibility to deposit more than three components, the proper positioning of a pattern generation with regard to previous ones is has shown to be difficult in iterative protocols.

2.3.3. CHEMOTAXIS ASSAYS

The process of chemotaxis describes the directed migration of a cell in response to a chemical stimulus (see Section 2.2.3). *In vitro* setups aiming to analyze this process are commonly realized by forming a soluble gradient of the desired chemical guidance cue using chemotaxis chambers. Although there are various different designs for chemotaxis chambers, in most cases, the means used to form the actual gradient is diffusion. In Figure 2.7, a simple design for a diffusion-based chemotaxis chamber, similar to the one used in this thesis, is shown. The chamber consists of two reservoirs which are interconnected by a comparatively narrow channel. If the solution within one the reservoirs exhibits a particle concentration of $c = c_0$ while no (or less) particles are present in the other reservoir, the resulting diffusion leads to the formation of a gradient in the interconnecting channel.

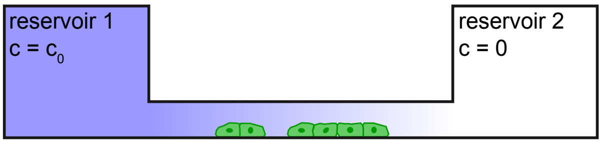

FIGURE 2.7.: Schematic drawing of a diffusion-based chemotaxis chamber. Different particle concentrations in the solutions in reservoirs 1 and 2 result in the formation of a gradient in the interconnecting channel. For chemotaxis experiments, the migration of cells within the channel is analyzed.

In order to understand the formation and shape of the gradients formed in such chambers, the basic principles of diffusion have to be understood.

PARTICLE DIFFUSION AND RESULTING GRADIENTS

Diffusion is the process of matter transport due to thermally driven random motion of particles. The net motion of particles follows the concentration gradient and hence points from regions of high particle concentrations towards regions of low particle concentrations.[114]

This process can be described mathematically by Fick's first law, which postulates that the diffusion flux, J, is proportional to the gradient in the concentration, c. Simplified to one dimension Fick's first law reads:

$$J = -D\frac{\partial c}{\partial x}. \tag{2.1}$$

The constant of proportionality, D, is called the diffusion coefficient. From Equation 2.1, the fundamental differential equation describing diffusion can be derived (see Reference [114] for detailed calculations):

$$\frac{\partial c}{\partial t} = D\frac{\partial^2 c}{\partial x^2}. \tag{2.2}$$

This partial differential equation, known as Fick's second law or diffusion equation, predicts the temporal concentration dynamics due to diffusion.

The particular solutions of Equation 2.2 depend on the specific initial and boundary conditions of the system. Chemotaxis chambers like the one shown in Figure 2.7 can approximately be described as a system possessing a large reservoir with a high particle concentration from which particles diffuse into a narrow channel. A particular solution for boundaries and initial conditions resembling such a setup will be presented in the following.

The reservoir is represented by a constant particle concentration, c_0, at the position $x = 0$ of the channel:

$$c(x = 0, t \geq 0) = c_0. \tag{2.3a}$$

Furthermore, no particles are present outside of the reservoir at the start of the experiment:

$$c(x > 0, t = 0) = 0. \tag{2.3b}$$

The solution satisfying Equation 2.2, as well as the conditions stated in Equations 2.3 can be written as:

$$c(x,t) = c_0\left[1 - \operatorname{erf}\left(\frac{x}{2\sqrt{Dt}}\right)\right] \tag{2.4}$$

(see Reference [114] for a detailed derivation). Here, erf is defined as the error function:

$$\operatorname{erf}(x) = \frac{2}{\sqrt{\pi}}\int_0^x e^{-z^2}\mathrm{d}z. \tag{2.5}$$

The slope of the corresponding concentration distributions can hence be written as:

$$\frac{\partial c}{\partial x} = \frac{c_0}{\sqrt{\pi D t}} \cdot e^{-\frac{x}{2\sqrt{Dt}}}. \tag{2.6}$$

Exemplary concentration distributions for different reservoir concentrations, c_0, and at different times after the start of diffusion are shown in Figure 2.8.

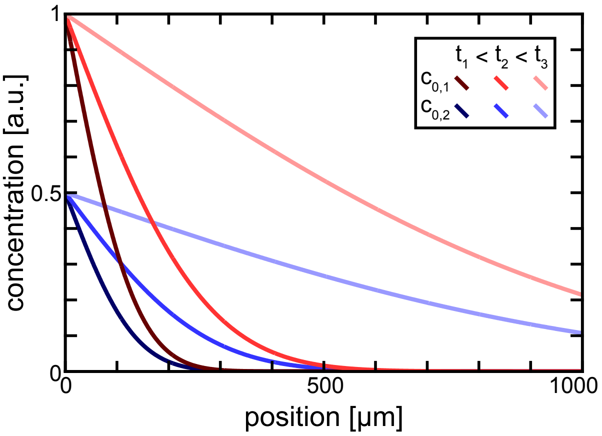

FIGURE 2.8.: Illustration of concentration distributions resulting from diffusion from a reservoir of constant concentration, c_0, at $x = 0$. The distributions are plotted according to Equation 2.4, which describes a solution of the one-dimensional diffusion equation. Curves are plotted for different reservoir concentrations of $c_{0,1} = 1$ and $c_{0,2} = 0.5$ and for different time points after start of the diffusion process ($t_1 = 5\,\text{min}$, $t_2 = 20\,\text{min}$ and $t_3 = 300\,\text{min}$). The diffusion coefficient is chosen as $D = 18\,\mu\text{m}^2/\text{s}$ (which should roughly correspond to the diffusion coefficient of fibrinogen molecules in aqueous solution[115]).

2.4. THEORETICAL DESCRIPTION OF CELL MIGRATION

In order to understand the underlying rules of cell behavior, theoretical descriptions and numerical models are inevitable. In the field of cell motility, such theoretical approaches serve, on the one hand, to mathematically characterize and quantify the migration patterns observed for different cell types in experiment on a phenomenological basis. On the other hand, they are essential to establish mathematical models aiming to understand and reproduce the concepts and mechanisms of cellular locomotion. The developments in both of these fields will be outlined in the following section.

2.4.1. MATHEMATICAL ASSESSMENT OF MIGRATION PATTERNS

In the absence of external guidance cues, a cell migrating on a 2D surface exhibits a migration pattern that is characterized by directional persistence on short timescales and erratic motion on long time scales. For decades, the persistent random walk in form of an Ornstein-Uhlenbeck process[116] hence served as the standard model to describe the resulting motion patterns.[117–119] In this process, the time evolution of a cell's velocity, $\vec{v}$, is described by the equation originally stated by Langevin[120] to describe the Brownian motion of a particle:

$$\frac{\mathrm{d}\vec{v}}{\mathrm{d}t} = -\frac{1}{\tau}\vec{v} + \frac{\sqrt{2D}}{\tau}\vec{\xi}(t). \tag{2.7}$$

Here, D denotes the diffusion coefficient, $\vec{\xi}(t)$ indicates a vector with white-noise components, and τ describes the persistence time of the process. In this model, the resulting mean squared displacement is given by the Fürth formula[121],

$$\mathrm{MSD}(t) = 2n_{\mathrm{dim}} D\tau \cdot (e^{-\frac{t}{\tau}} + \frac{t}{\tau} - 1), \tag{2.8}$$

where n_{dim} indicates the spatial dimension of the system. Figure 2.9 shows the MSD of the Ornstein-Uhlenbeck model for different persistence times, τ. It becomes evident that on short timescales the MSD shows a behavior of $\mathrm{MSD}(t) \propto t^2$, corresponding to directionally persistent motion. In contrast, on long timescales, $\mathrm{MSD}(t) \propto t$, corresponding to the diffusive motion of a Brownian particle, as derived by Einstein[122].

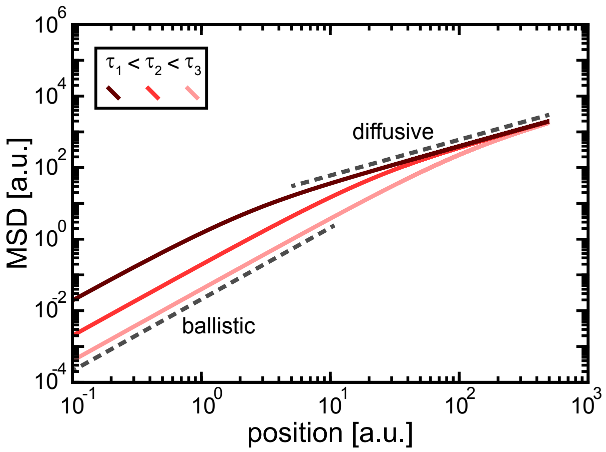

FIGURE 2.9.: Prediction for the MSD according to the Ornstein-Uhlenbeck process. The MSD of the Ornstein-Uhlenbeck process is plotted according to Equation 2.8 in log-log representation for three different persistence times, τ. Dashed black lines indicate fits corresponding to ballistic ($\mathrm{MSD}(t) \propto t^2$) and diffusive ($\mathrm{MSD}(t) \propto t$) motion.

The fit of the experimental data to Equation 2.8 often serves as the main argument why experimentally observed migration patterns are attributed to an underlying Ornstein-Uhlenbeck process. However, in more recent studies it has been shown that simply fitting the MSD is not sufficient to draw such conclusions.[123–126] Furthermore, several publications indicate that the paths described by individually migrating cells are not sufficiently represented by a single mode of migration but rather exhibit dynamic transitions between different modes of migration.[127–129]

2.4.2. MODELS FOR CELL MIGRATION

Over the last decades, a vast number of different models aiming to describe and understand the process of cell migration have been proposed. The different implementations of these models cover multiple levels of complexity. On the microscopic scale, several models have been implemented addressing the emergence of cellular locomotion from sub-cellular processes like intracellular reaction diffusion dynamics.[21–24] On the macroscopic scale, the dynamics of collective migration of large cell numbers is often captured by coarse grained models, in which individual cells are represented by interacting, self-propelled particles or simple geometrical objects[25–27].

Each of these approaches brings its individual benefits and drawbacks. While microscopic models potentially give insights into the dynamics of the intracellular migration machinery, they are usually too complex and computationally intensive to simulate larger cell assemblies and tissues. Furthermore, aiming to describe the locomotion of individual cells, these models often lack the aspect of intercellular signaling. Macroscopic models, in contrast, are designed to describe and understand large scale phenomena emerging from the interaction of vast numbers of individual cells. Hence, focusing on averaged emergent features, they lose explanatory and predictive power with regards to smaller systems and sub-cellular processes.

A modeling approach exhibiting an intermediate level of coarse graining is the so-called cellular Potts model (CPM). Originally implemented by James Glazier and François Graner[130,131] as an extension of the Potts model, aiming to describe cell sorting phenomena, the CPM has found widespread application in cell research.

The basic principle of the CPM as it is illustrated in Figure 2.10 can be outlined as follows: The system is described as a lattice with an index (spin), $\alpha(k)$, assigned to each grid site, $\vec{x}_k$. A cell is defined as a set of adjacent grid sites of the same index. The energy of the system is defined by a Hamiltonian, $\mathcal{H}$. Although different implementations of this Hamiltonian have been proposed, a classical definition is given by:

$$\begin{aligned}\mathcal{H} = \sum_{i,j\,neighbors} & J[\tau(\alpha(i)), \tau(\alpha(j))] \cdot [1 - \delta_{\alpha(i),\alpha(j)}] \\ & + m \sum_{\alpha} [A(\alpha) - A_{\text{target}}(\alpha)]^2 \\ & + a \sum_{\alpha} [P(\alpha) - P_{\text{target}}(\alpha)]^2 .\end{aligned} \tag{2.9}$$

Here, J is the boundary coefficient giving the interaction of adjacent grid sites, while τ indicates the cell type (if different cell types are implemented). Consequently, the first term accounts for the interaction energy of neighboring cells. $A(\alpha)$ and $P(\alpha)$ indicate the actual area and perimeter of the cell defined by the index α, while the constants A_{target} and P_{target} denote the corresponding target values of these quantities. The second and third term hence represent the energy contributions of the elastic properties of a cell. While deviations from the target values, A_{target} and P_{target}, are energetically penalized, the multipliers m and a weight the contribution of the individual terms.

The dynamics of the system are represented by "elementary events", $\mathcal{T}$, in form of copy processes implemented in a Monte Carlo procedure (Fig. 2.10). In each Monte Carlo step (MCS),

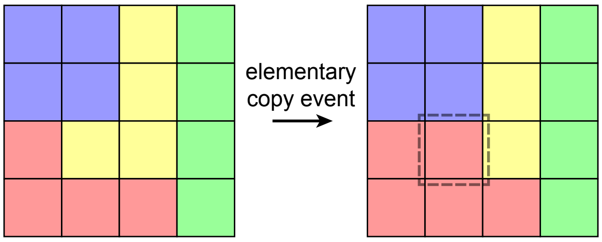

FIGURE 2.10.: Illustration of the cellular Potts model. Cells are represented as connected sets of pixels to which the same index (color) is attributed. The dynamics of the system are resembled by copy processes in form of protrusions and retraction events in which a cell takes over or loses a grid site.

a certain number of “source” grid sites, $\vec{x}_s$, is randomly chosen. For each of these sites, an elementary event, $\mathcal{T}$, is performed, in which the index assigned to $\vec{x}_s$ is copied to one of the neighboring “target” grid sites, $\vec{x}_t$. For each elementary event, the probability for the copy process to be successful is calculated as

$$p(\mathcal{T}) = \min\{1, e^{-\frac{\Delta\mathcal{H}}{\mathrm{k_b}T}}\}, \tag{2.10}$$

where $\Delta\mathcal{H}$ indicates the difference in energy for the successful elementary event. The constant term, $\mathrm{k_b}T > 0$, can be adjusted to regulate the activity of the system.

The original version of the CPM has been extended in various ways. Its applications in cell science range from the study of intracellular processes like internal polarization of individual cells[132] to large scale phenomena emerging from cell-cell interactions within large assemblies and tissues[133,134].

CHAPTER 3

MICROSCALE PLASMA-INDUCED PROTEIN PATTERNING*

Micropatterning has established as a tool to create highly specialized microenvironments addressing open question on cellular properties and functions in life sciences. The applications of micropatterning are various and range from protein expression assays[28] over research on cell polarization, division, and coupling[29–33] to motility studies on single-cell[13,34–37] as well as on collective[38–40] level. In order to enable a wide range of cell-science labs to benefit from the possibilities provided by micropatterning, versatile and yet easy-to-use patterning protocols are required. In this context, microscale plasma-induced protein patterning (μPIPP), a novel and easy-to-handle patterning method was developed in the course of this thesis. μPIPP is able to produce protein patterns on a variety of substrates and can be extended to create setups featuring gradients in protein density as well as patterns composed of multiple proteins.[135] In this chapter, the concept of μPIPP is introduced and the produced patterns and their implications for cell research are discussed.

3.1. CONCEPT AND FUNCTION

The basic concept of μPIPP (see Section A.1 for detailed working protocols) is a spatially controlled plasma treatment of the substrate in combination with a poly(ethylene-glycol) (PEG) coating and protein incubation. As depicted in Figure 3.1, the surface is first covered by a poly(dimethyl-siloxane) (PDMS) stamp of the desired pattern. Afterwards, the exposed surface parts are treated with O_2 plasma. The plasma removes organic residues from the surface, leads to oxidation, and introduces polar groups (such as carbonyl or carboxylic acid) which promote surface hydrophilicity. Furthermore, depending on the surface material, decomposition and abrasive removal of material leads to surface ablation and increased surface roughness (in the order of a few hundred nm).[136–138] In the next step, the plasma-exposed surface parts are incubated in a solution of the block copolymer PLL-PEG (see Section 2.3.2 for the detailed

---

*This chapter is to a large part based on the publication Segerer *et al.*[135].

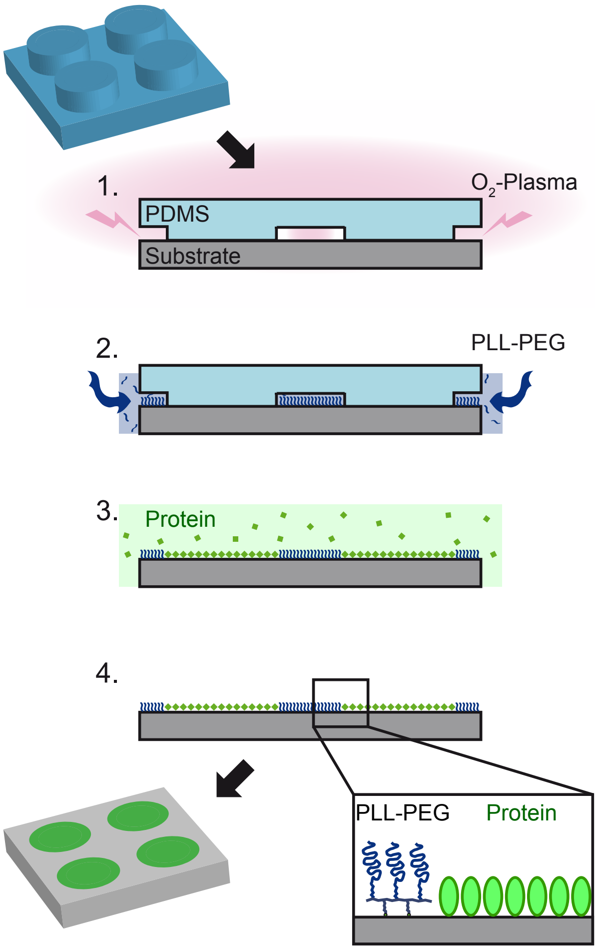

FIGURE 3.1.: Procedure of µPIPP. 1. The surface is partially covered by a PDMS stamp of the desired pattern and subsequently exposed to O_2 plasma 2. A PLL-PEG solution is applied to the margins of the stamp and is drawn between stamp and surface by capillary action 3. After removal of the stamp, the surface is incubated in a solution containing the desired protein. Figure adapted with permission from Reference [135]. Copyright 2016, American Vacuum Society.

polymer structure). Since the PLL groups of the molecule are positively charged, they serve as an electrostatic anchor, linking the polymer to the plasma-activated surface.[139] As described in Section 2.3.2, the PEG chains of the polymer work as a polymeric cushion, rendering the surface protein repellent by steric hindrance.[94,96] Finally, the PDMS stamp is removed and the surfaces is incubated with a protein solution, resulting in protein adhesion to the untreated (i.e. not PEGylated) surface parts.

3.2. PATTERNING DIFFERENT SUBSTRATE MATERIALS

To test whether the method is compatible with commonly used cell-culture substrates, µPIPP was applied to standard tc-PS, glass, cyclic olefin copolymer (COC), parylene C, and PDMS.

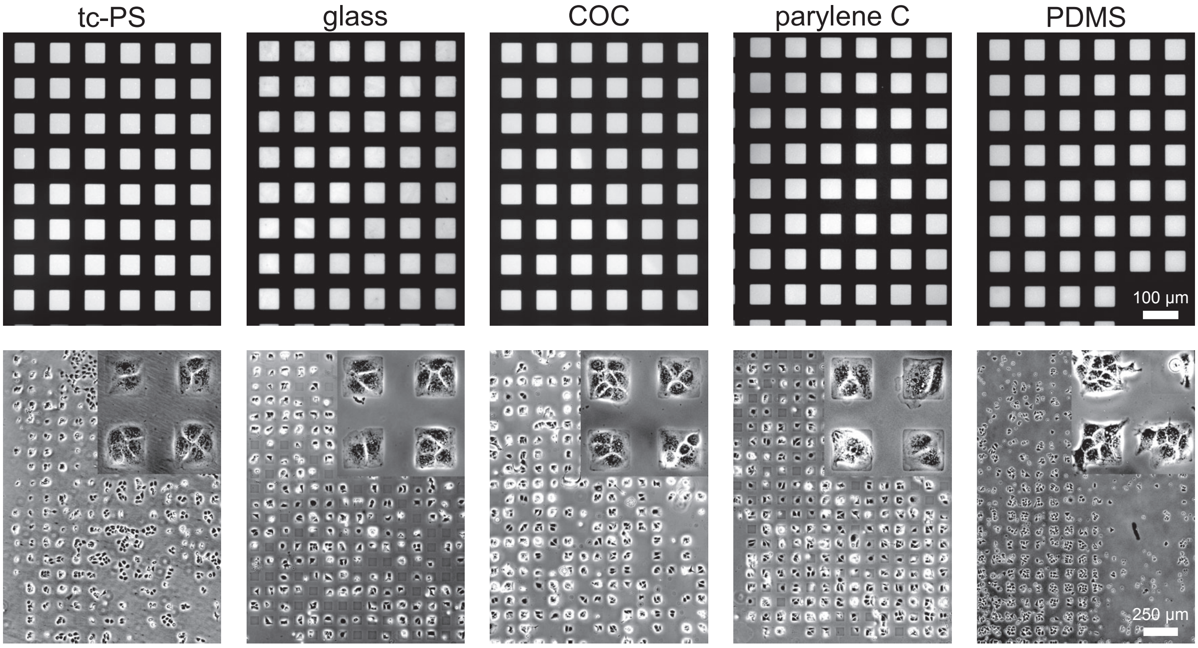

FIGURE 3.2.: µPIPP on different substrates: tc-PS, glass, COC, parylene C, and PDMS (Upper row) Fluorescence images of patterns composed of fibrinogen Alexa-488 (bright) and PLL-PEG (dark). (Lower row) MDCK cells on fibronectin patterns 24 h after cell seeding (insets 5x magnified). Figure adapted with permission from Reference [135]. Copyright 2016, American Vacuum Society.

On all of these materials, µPIPP produced homogeneous protein patterns as can be seen in Figure 3.2. Regarding the cell adhesion and confinement, differences in pattern quality were observed though. Good cell confinement was achieved on tc-PS, glass, COC, and parylene C.

To gain a more detailed insight into how accurately cells adapt to the geometry of the patterns, cells on square patterns were fixed and dehydrated according to Section A.2.2 and visualized using scanning electron microscopy. The resulting images, shown in Figure 3.3, illustrate that MDCK cells within the patterns mostly arrange their cytoskeleton such that the area provided by the the pattern is filled completely.

Despite the proper arrangement of protein on PDMS, the confinement of cells within the patterns on this substrate was not stable over time. After short times of confinement ($\sim$ few hours), cells leaving the protein-coated areas were observed on this material. This finding can possibly be attributed to the fact that O_2-plasma exposure induces the formation of silicon oxide groups (SiO_x) on PDMS[140,141], which might result in a different rigidity or roughness of the surface and hence affect cell adhesion behavior. In general, the increased hydrophilicity of plasma-treated PDMS results in enhanced cell adhesion as compared to untreated PDMS[107,110,142] (as was also found in previous studies). If a cell is able to “feel” the PDMS substrate underneath the PEG or protein layer, this effect might hence cancel out the repulsive/adhesive effect of the PEGylation/protein coating. Another possible explanation would be that no proper PEG layer is formed on PDMS in the first place and that the selec-

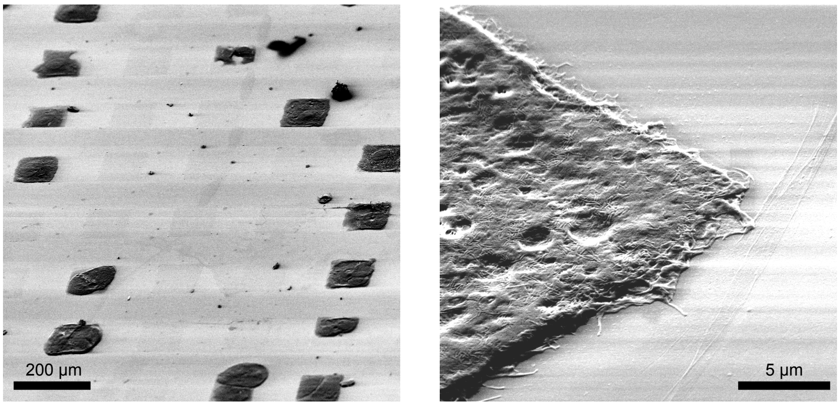

Figure 3.3.: Confinement of cells within micropatterns. Scanning electron microscopy images of MDCK cells confined to square-shaped micropatterns created via µPIPP on a glass substrate. (See Section A.2.2 for a detailed description of the pretreatment of cells and substrate.)

tive protein adsorption is solely due to the difference in hydrophilicity between untreated and plasma activated PDMS. Protein attachment studies to plasma patterned PDMS without the use of PEGylation might provide clarity in this point. As, in the course of this work, COC (in form of ibidi slides[143]) was the prevailing material for all cell experiments, the following procedures and results are focused on this substrate.

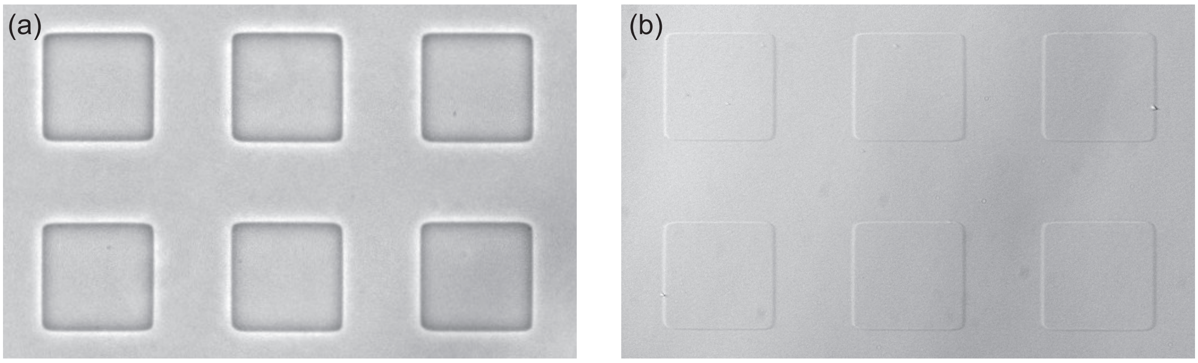

Figure 3.4.: Patterns produced via µPIPP are visible in contrast enhanced optical microscopy. Square patterns (width 60 µm) on COC imaged by (a) phase-contrast and (b) differential interference contrast microscopy. Figure adapted with permission from Reference [135]. Copyright 2016, American Vacuum Society.

Due to the plasma treatment, which alters the altitude as well as the roughness of the activated parts of the substrates[136,138], patterns produced by µPIPP are visible in contrast enhanced optical microscopy. Figure 3.4 shows patterns created by µPIPP in phase-contrast and differential interference contrast. Due to this feature, patterned regions within cell dishes and slides can be readily located and identified before cell seeding and without the need for fluorescently labeled pattern components. This does not only simplify the appropriate choice of image positions for time lapse measurements but also facilitates image processing. In this regard, the plasma approach hence provides a clear advantage over conventional µCP or photolithography based techniques for which this feature is not given.

The patterns produced by μPIPP are stable and capable to confine cells over time periods of up to several days as can be seen in Figure 3.5. As cell migration experiments usually extend over at least 24 h, such long term stability is essential for patterning techniques in cell research.

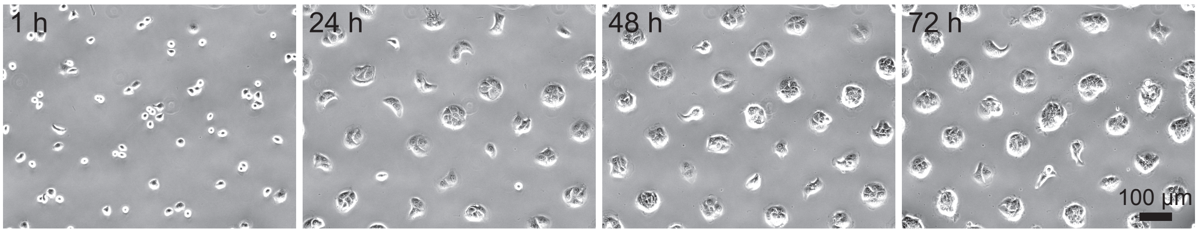

FIGURE 3.5.: Cells are confined to pattern elements for time periods of several days. MDCK cells confined in circle shaped micropatterns (radius 46 μm) at different time points after cell seeding. Figure adapted with permission from Reference [135]. Copyright 2016, American Vacuum Society.

3.3. PROTEIN SURFACE DENSITY AND GRADIENTS

The relative density of adhesion sites[17,144,145] as well as density gradients of surface-bound proteins[85,86,88,146] can influence and bias cell spreading and motion. To study these aspects of cellular behavior, experimental setups exhibiting variations in the surface-bound protein density are needed. Patterning techniques which provide control over protein density and enable the formation of protein gradients hence offer additional value for cell experiments.

In contrast to the stamping process of conventional μCP, the protein is adsorbed to the pattern sites from a protein solution in the process of μPIPP. This feature provides the possibility to adjust the amount of protein attached to the substrate. Such an adjustment can be achieved via varying either the concentration of protein in the incubation solution or the time for which the substrate is incubated. The corresponding effects on the surface concentration of protein can be seen in Figure 3.6(a). Here, for three different incubation times, $\tau = 5$, 15, 25 min, the concentration of Alexa-488 labeled fibronectin within the incubation solution was varied as $c_{\mathrm{sol}} = 7.5$, 15, 30, 75 μg/ml. For each combination of τ and c_{sol}, the fluorescence intensity within over 1500 pattern sites was measured in four independent experiments. The relatively small standard deviation between the experiments illustrates the reliability and reproducibility of the μPIPP protocol. The mean values show that an increase in τ or c_{sol} results in an increased fluorescence intensity and consequently in an increased concentration of protein attached to the surface.

The concentration of protein adsorbed to the surface, c_{surf}, as a function of c_{sol} is well fitted by the Langmuir adsorption isotherm[147]:

$$c_{\mathrm{surf}} = c_{\mathrm{sat}} \cdot \frac{\alpha c_{\mathrm{sol}}}{1 + \alpha c_{\mathrm{sol}}} \tag{3.1}$$

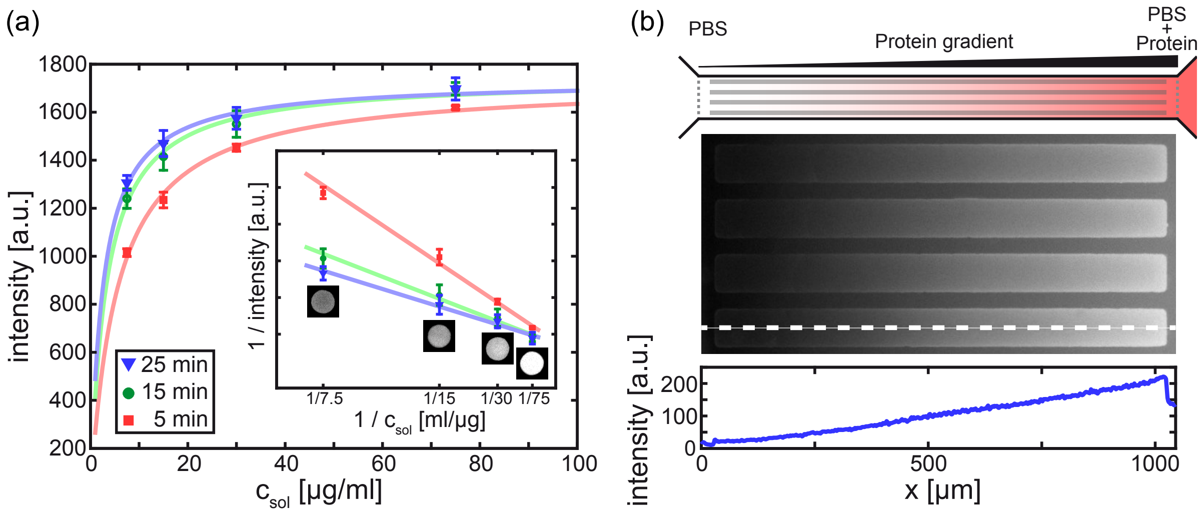

FIGURE 3.6.: Variation of protein surface concentration using μPIPP. (a) The protein surface density within patterns depends on both the protein concentration in the incubation solution, c_{sol}, and the incubation time, τ. The fluorescence intensity in micropatterns of Alexa-488-labeled fibrinogen for incubation times, $\tau = 5$, 15, 25 min, is plotted against the protein concentration in solution, $c_{\text{sol}} = 7.5$, 15, 30, and 75 μg/ml. The data is fitted by a Langmuir isotherm (Eq. 3.1) with equilibrium constants, α_τ, of $\alpha_5 = 0.18 \pm 0.06$, $\alpha_{15} = 0.31 \pm 0.16$, and $\alpha_{25} = 0.39 \pm 0.18$, for the different incubation times, τ, respectively (± errors indicate confidence bounds of 95 % within the fits). The inverse presentation in the inset illustrates the corresponding linear scaling. Error bars indicate the standard deviation among four individual experiments. (b) Via protein incubation in a chemotaxis chamber, a gradient in the surface-bound protein density was generated within the patterns. Top down: 1. Illustration of the protein gradient within the chemotaxis slide. 2. Fluorescence image of micropatterned stripes obtained by incubation in a gradient of fibrinogen Alexa-488. 3. Measured fluorescence intensity along the dashed line shown in the middle panel. Figure adapted with permission from Reference [135]. Copyright 2016, American Vacuum Society.

Here, c_{surf} denotes the protein concentration on the surface, c_{sat} the hypothetical saturated concentration of protein on the surface, and α the equilibrium constant in the case of Langmuir adsorption. It has to be considered, however, that at least for $\tau = 5$ min and $\tau = 15$ min, the protein surface concentration, c_{surf}, increases further for longer incubation times, τ. This indicates that adsorption and desorption of protein to and from the surface are not in equilibrium and hence the Langmuir assumptions resulting in Equation 3.1 are not met. Although the data suggests that for longer incubation times an equilibrium regime may be approached asymptotically, the Langmuir expression is provided here as an estimate for the scaling of c_{surf} with c_{sol} only, whereby the resulting values of α and c_{sat} should not be interpreted in the framework of the Langmuir adsorption model. In fact, it has been shown that also other effects than the initial assumptions in the derivation of Equation 3.1 can result in adsorption isotherms closely resembling the shape of the Langmiur isotherm.[148]

The fact that c_{surf} depends on c_{sol} can not only be exploited to adjust the protein surface density globally but can also be utilized to generate a spatial protein gradient within the micropatterns. For this purpose, a chemotaxis chamber was used to establish a gradient in the protein concentration of the incubation solution, c_{sol}. The chamber used was a “sticky-Slide Chemotaxis” (ibidi)[149,150], which enabled the creation of a pattern consisting of PEGylated and untreated surface parts on the substrate prior to attaching the actual chemotaxis chamber (see Section A.1 for detailed protocols). Afterwards, the upper part of the chamber was attached to the surface and a protein gradient in the incubation solution was formed.

The properties of the resulting gradient in the protein surface density, c_{surf}, depends on the time the surface is incubated as well as on the protein concentration, c_0, in the protein-filled reservoir of the chemotaxis chamber. The effects of both factors were studied within the framework of a bachelor thesis.[151] The results of experiments in which, for a fixed incubation time, the concentration c_0 was varied are shown in Figure 3.7(a). The graph indicates that an increase in c_0 potentially affects the global protein surface concentration (as becomes evident from a comparison of the curves for $c_0 = 50\,\mu\mathrm{g/ml}$ and $c_0 = 100\,\mu\mathrm{g/ml}$) as well as the average slope of the protein gradient (as becomes evident from a comparison of the curves for $c_0 = 10\,\mu\mathrm{g/ml}$ and $c_0 = 50\,\mu\mathrm{g/ml}$). Both of these facts can be explained when considering Equation 2.4 as an estimate of the time evolution of the solute protein gradient. In this framework, the local slope of the gradient (Eq. 2.6) as well as the local concentration of protein depend on c_0. As the surface protein concentration depends on the protein concentration in solution, such a dependence on c_0 is also predicted for the surface-bound protein gradient.

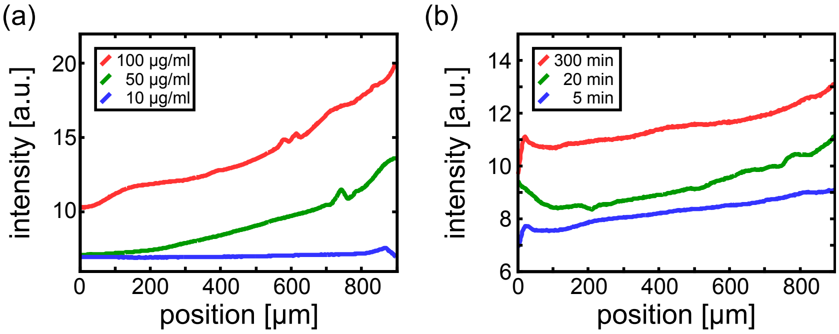

FIGURE 3.7.: Adjustment of the gradient in the surface density of proteins. Fluorescence intensity along a COC substrate incubated in a solute gradient of Alexa-488-labeled fibrinogen. The fluorescence intensity indicates the amount of protein adsorbed to the surface. (a) For a fixed incubation time of $\tau = 30\,\mathrm{min}$, the maximal protein concentration of the solute gradient was varied from $c_0 = 10\,\mu\mathrm{g/ml}$ to $c_0 = 50\,\mu\mathrm{g/ml}$ and $c_0 = 100\,\mu\mathrm{g/ml}$, respectively. (b) For a fixed maximal protein concentration of $c_0 = 50\,\mu\mathrm{g/ml}$, the incubation time was varied from $\tau = 5\,\mathrm{min}$ to $\tau = 20\,\mathrm{min}$ and $\tau = 300\,\mathrm{min}$, respectively.

The influence of the time for which the surface is exposed to the solute gradient was analyzed in a second set of experiments whose results are shown in Figure 3.7(b). The graph indicates that an extended incubation time, τ, leads to a global increase in the concentration of protein on the surface, while the average slope of the gradient remains approximately constant for the analyzed incubation times. This result cannot be directly explained by Equation 2.4 as the theory predicts a dependence of the slope of the solute gradient on the time over which the gradient is established (Eq. 2.6). It has to be considered, however, that the formation of the solute protein gradient is a dynamic process which goes on over the time of incubation. The assumption of a stable solute gradient directly resulting in the gradient in the protein surface density is hence oversimplified. Furthermore, the dynamics of protein adhesion have to be considered when comparing the protein gradient in the solution with the surface-bound protein gradient. An interplay of these features might also explain the comparatively linear shape of the surface-bound gradients when compared to the theoretical solute gradients depicted in Figure 2.8. Nonetheless, these experiments show that the properties of the gradient in the surface density of the applied protein can be tuned by adjusting the incubation time and the initial protein concentration within the reservoir.

Taken together, the results of this section illustrate that by adjusting the conditions of the protein incubation step, the protein concentration within micropatterns created via µPIPP can be tuned. This feature can not only be exploited to adjust the protein concentration globally but also to accomplish spatial gradients in the surface-bound protein density. A more detailed theoretical description of the combined effects of protein diffusion and surface adhesion might help to tune the shape of these gradients by adjusting the experimental conditions in future studies. Furthermore, after formation of the surface-bound protein gradient and cell seeding, the chemotaxis chamber used in the protocol provides the possibility to establish a second gradient of guidance cues in the solution surrounding the attached cells. This way, microenvironments can be created which combine guidance cues resulting from (i) a gradient in the surface-bound protein density, (ii) a soluble protein gradient, and (iii) the confinement of the micropattern. The implementation of such multi-cue environments provides the possibility to directly address and analyze cellular decision making and possible synergy or competition effects between cellular guidance cues.

3.4. PATTERNING MULTIPLE PROTEINS

The protein composition of the environment strongly effects a cell's attachment and migration behavior.[17,112,152,153] Experimental setups which combine different protein coatings are hence of high interest in cell research. This is due to the fact that such setups do not only allow to compare cell behavior on different protein types directly, but also enable to study cell behavior at the interface between different coatings.

In order to provide spatial control over the deposition of more than one protein (in addition to the PEGylation), the µPIPP protocol was combined with conventional µCP (see Section A.1.6 for detailed protocols). One way this was achieved was via applying both techniques simultaneously by using stamp geometries which exhibit enclosed cavities. The corresponding procedure is illustrated in Figure 3.8. Using this protocol, the embossed parts of the stamp which actually get into contact with the substrate are used for µCP of the first protein, while the enclosed cavities solely work as a shielding from plasma and PLL-PEG exposure. In the final protein incubation step, the second protein attaches to the surface parts at which no PEGylation or protein coating is already present. As depicted in Figure 3.9(a), complex patterns

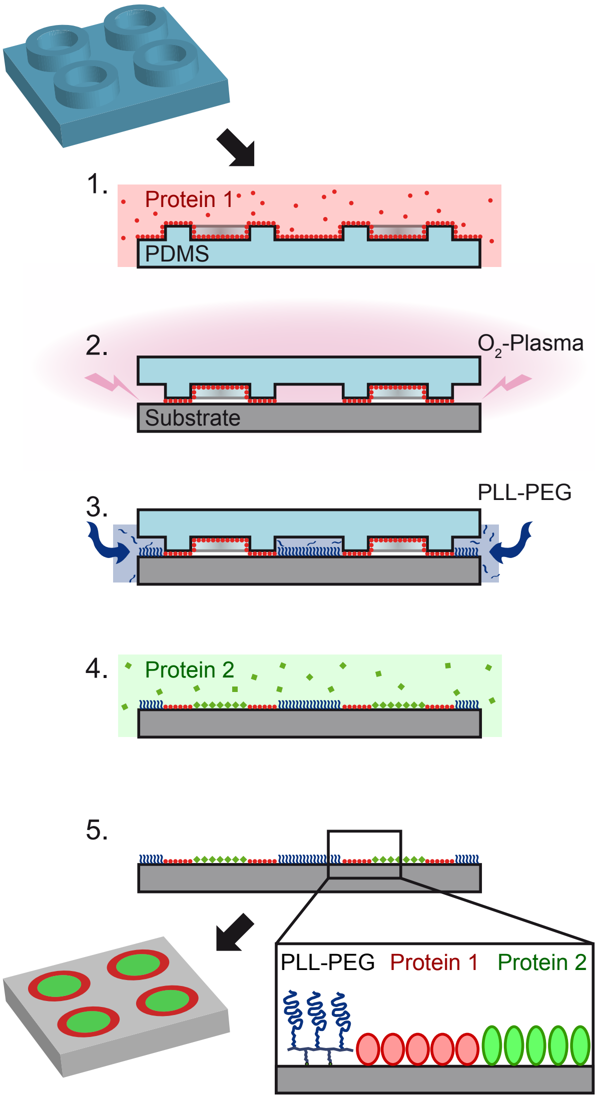

FIGURE 3.8.: Procedure of combining µPIPP with µCP. 1. Following a UV-ozone activation (see Section A.1.6), a PDMS stamp of the desired pattern is incubated in a solution containing protein 1. 2. The protein-coated stamp is inverted and protein 1 is printed on the surface, which is simultaneously exposed to O_2 plasma 3. PLL-PEG solution is applied to the margin of the stamp and drawn between stamp and surface by capillary action 4. After removal of the stamp, the surface is incubated in a solution containing protein 2. Figure adapted with permission from Reference [135]. Copyright 2016, American Vacuum Society.

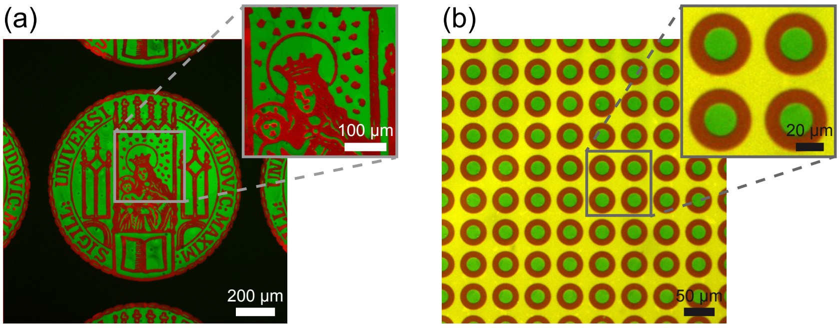

FIGURE 3.9.: Multi-component protein patterns created via combining the protocols of µPIPP and µCP. (a) Seal pattern composed of PLL-PEG (black) and fibrinogen labeled with Alexa-488 (green) and Alexa-647 (red), respectively. (b) Framed circle pattern composed of fibrinogen Alexa-647 (red) which was printed via µCP, fibrinogen Alexa-594 (yellow) which was drawn and adsorbed underneath the stamp by capillary action, and fibrinogen Alexa-488 (green) which was adsorbed to the remaining surface parts from the incubation solution. Figure adapted with permission from Reference [135]. Copyright 2016, American Vacuum Society.

composed of two proteins and a PEGylation can be created using this method. By applying a third kind of protein instead of PLL-PEG, also patterns consisting of three different proteins can be formed (Fig. 3.9(b)).

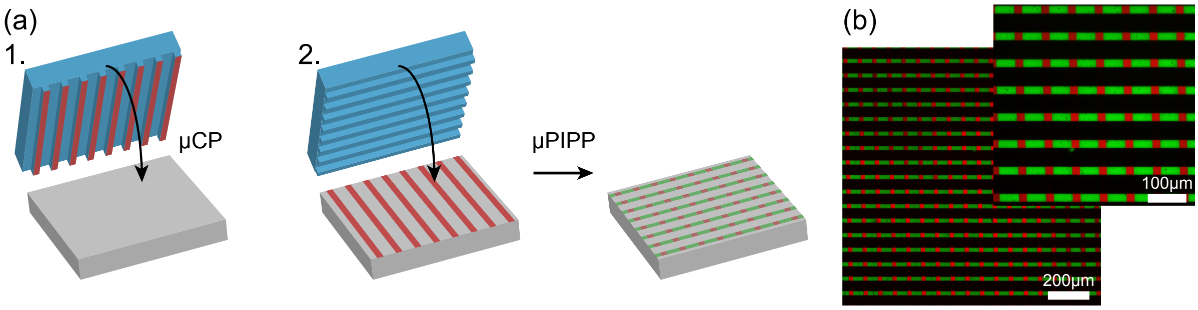

FIGURE 3.10.: Successive combination of µPIPP and µCP. (a) Patterning procedure: 1. Via µCP, a pattern consisting of the first protein and bare substrate is created. 2. µPIPP is applied such that the pattern created via µCP is partially removed by the plasma and replaced by areas coated with a second protein or PLL-PEG, respectively. (b) Dashed line pattern composed of fibrinogen Alexa-488 (green), fibrinogen Alexa-647 (red), and PLL-PEG (black), created via the successive combination of µPIPP and µCP. Figure adapted with permission from Reference [135]. Copyright 2016, American Vacuum Society.

It is worth pointing out that combining µPIPP and µCP in this way, the specific geometry of the stamp is used to produce a multi-component pattern within one iteration of the protocol. In contrast to multi-component patterning methods that work iteratively (see Section 2.3.2), this brings the advantage that the different components of the pattern are readily placed directly adjacent and in proper orientation to each other. Yet a drawback of this method is caused by the fact that only “framed” pattern designs in which one component (the one attached from solution in the last step) is completely surrounded by another one (the one printed via µCP) can be realized.

In order to overcome this limitation and extend the set of achievable geometries, an additional protocol, combining µPIPP and µCP in a successive manner was developed. As illustrated in Figure 3.10(a), this way of joining both techniques works via applying µPIPP to an already existing pattern created via µCP. In doing so, the pattern created via µCP is partially removed by the plasma used for µPIPP (see Section A.1 for detailed protocols).

Using this method, multi-component patterns such as the “dashed line patterns” shown in Figure 3.10(b) can be realized. Compared to the simultaneous combination of µPIPP and µCP, this successive combination approach is slightly more time-consuming and brings the challenge to correctly position one pattern to the other. Nonetheless, the approach extends the set of achievable pattern geometries with regards to multi-component designs not including framed structures.

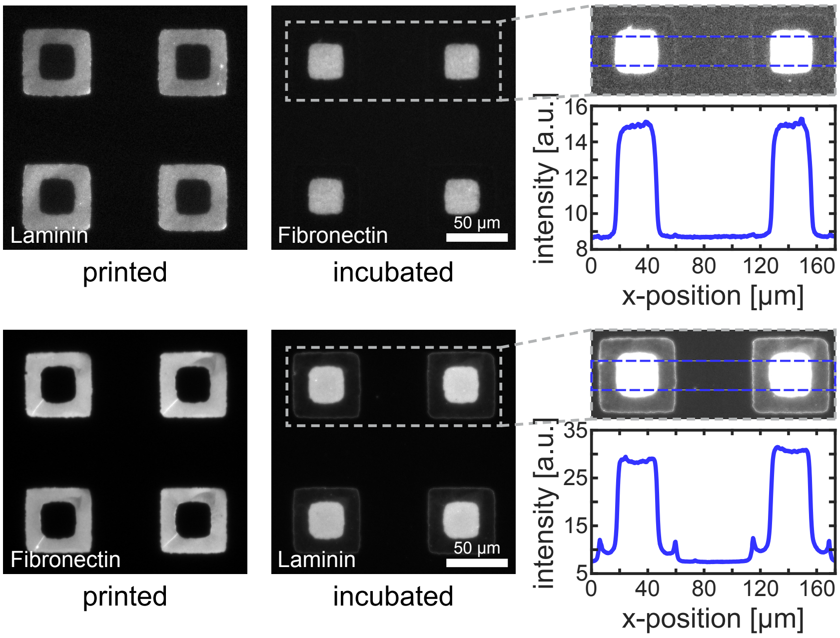

FIGURE 3.11.: Co-adhesion of proteins. Pictures of the individual fluorescence signals of a pattern composed of fluorescently labeled fibronectin and laminin-I (PLL-PEG is not labeled) created via the simultaneous combination of µPIPP and µCP. The upper row shows the result of an experiment in which laminin-I was placed via µCP and fibronectin was adhered from solution, while for the lower row the experiment was conducted vice versa. The pictures of the corresponding zoom-ins are overexposed to bring out weak intensity signals. In the graphs, the intensity along the x-position of the blue dashed rectangles, vertically averaged along the rectangle height, are plotted (for the not-overexposed images). The small intensity peaks at the outer edge of the patterns are most likely the result of protein accumulation at the increased surface of the sill, stemming from the plasma treatment. Note that due to different numbers of fluorescent dyes per protein and different illumination conditions, direct comparison of intensities among the individual images yields no information on relative protein density here.

It is important to mention that both multi-component patterning approaches introduced here (as almost all iterative multi-protein micropatterning approaches) include a final step in which the second protein is incubated to an already existing pattern composed of free surface and areas coated with PEG or the first applied protein type, respectively. Proper spatial separation of both protein coatings can hence only be achieved if the second applied protein does not adhere to the surface areas at which a layer of the first applied protein is already present. If and to what extend an accumulation or exchange of both proteins occurs depends strongly on the combination of protein types used. Whether or not the second protein attaches to the areas where the first protein is coated can even depend on the order in which the proteins are applied. Figure 3.11 shows patterns composed of fibronectin and laminin-I created via the simultaneous combination of μPIPP and μCP. For one of the shown patterns, laminin-I is printed and fibronectin is adhered from solution, while for the other one the experiment was conducted vice versa. The transfer of protein from the stamp to the surface worked well in both cases. In the fluorescence signal, no adhesion of fibronectin on the laminin-I coated surface is visible (at least no adhesion exceeding that of fibronectin on the PEGylated areas). In contrast, adhesion of laminin-I to fibronectin coated areas can be distinguished. This seemingly symmetry break in protein-protein interaction can possibly be explained by the fact that surface adsorption of proteins often leads to conformational changes in the protein structure[89–91]. Such conformational changes could result in an increased or decreased affinity of the printed protein to the protein in solution and hence favor or inhibit co-adhesion of proteins. Another possible explanation would be provided by the Vromann effect, which describes the replacement of surface-attached proteins by other proteins having a higher affinity for the particular surface.[154] Since higher surface affinity often goes along with a higher molecular weight (MW) of the corresponding protein, this effect is not unlikely to explain the asymmetric exchange in the case of fibronectin (MW $\approx$ 220 kDa) and laminin-I (MW $\approx$ 400 kDa).

In the course of this work, strong co-adhesion was observed only for the protein combination fibronectin/collagen-I, for which interaction in form of binding is known[155,156]. Only weak or no co-adhesion (comparable to the cases shown in Figure 3.11) was observed for the combinations fibronectin/laminin, fibronectin/e-cadherin, fibronectin/mucin, fibronectin/fibrinogen, and fibrinogen/fibrinogen. Nonetheless, protein accumulation or exchange have to be considered when intending to create multi-component patterns using other protein combinations in future experiments.

The multi-component patterns created by the methods described above can be used to test and compare cell responses to different surface coatings. As a proof of principle, adhesion of human umbilical vein endothelial cells (HUVECs) on framed square patterns consisting of the two extracellular matrix proteins fibronectin and laminin-I was studied. Both proteins are usually found in the ECM and are known to play a role in cell adhesion via binding to integrin receptors and other membrane molecules.[157,158] Cell adhesion within the patterns was found to be strongly affected by the respective protein coating. As depicted in Figure 3.12, HUVECs adhered well on surface parts coated with fibronectin, whereas they avoided laminin coated areas. This behavior was not influenced by the way the proteins were deposited, as HUVECs avoided laminin coated areas and attached to fibronectin coated surface regardless of whether the respective protein was placed via printing or adhered from solution. This indicates that also the effect of the already discussed accumulation of laminin on areas printed with fibronectin was small in this regard. In general, laminin is known to promote or weaken cell adhesion,

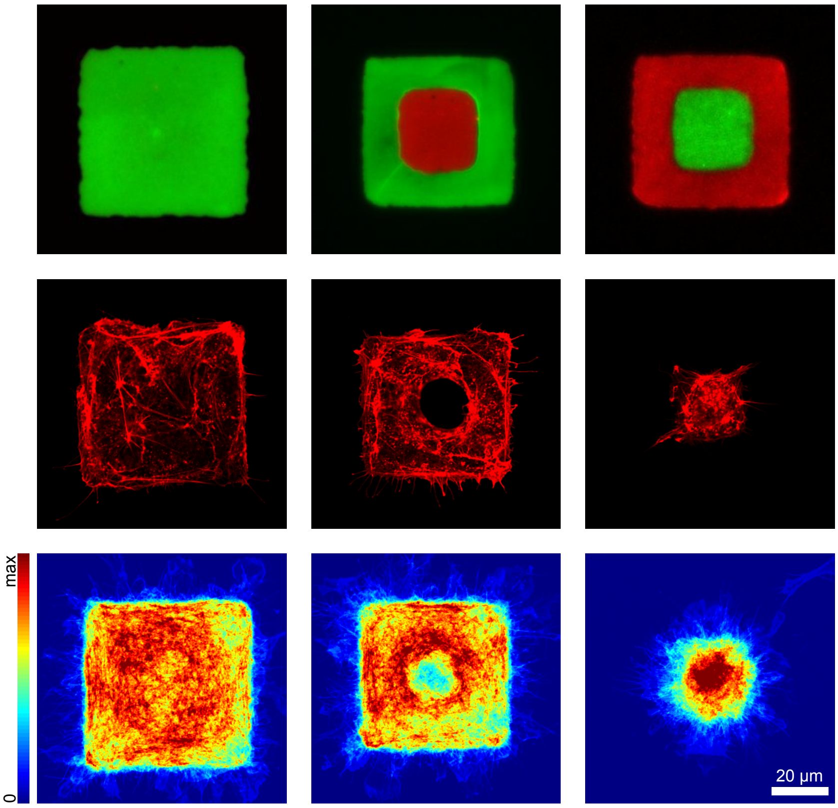

FIGURE 3.12.: Cells on multi-component patterns. (top row) Fluorescence image of square and framed square patterns composed of fluorescently labeled fibronectin (green) and laminin (red). (middle row) Representative confocal fluorescence image of the actin cytoskeleton of HUVECs arranged on the pattern. (bottom row) Heat map of the actin cytoskeleton distribution of HUVECs on over 20 evaluated patterns. All three patterns were created via simultaneously applying µPIPP and µCP. Figure adapted with permission from Reference [135]. Copyright 2016, American Vacuum Society.

depending on the cell type.[112,157] However, there are several reports on wild type HUVECs attaching to laminin.[159,160] The found strong inhibition of cell adhesion induced by laminin is therefore surprising. A possible explanation might be an eventual increased or decreased denaturation of laminin on the COC surface compared to its denaturation on the cell culture dishes (presumably PS) used in references [159, 160]. Also, the specific type or origin of the protein or the HUVECs could have influenced the result. In the course of this thesis, however, this experiment solely serves to test and illustrate the application of the developed patterning protocol with regards to cell behavior on multi-component patterns. Hence, the specific interactions of individual proteins with different cell types are not going to be discussed in more detail here.

Still, the example shows that multi-component patterning on the basis of µPIPP is a suitable framework to study and compare cellular interactions with distinct surface coatings and well defined interfaces. As the patterning approach is relatively easy to implement but nonetheless allows for the formation of complex arrangements of proteins with accurate relative positioning, it is a powerful tool and might proof useful in future cell studies.

3.5. ANALYSIS AND QUANTIFICATION OF THE PEG PASSIVATION*

The PEGylated surface areas created via µPIPP do, depending on the cell type, not always provide complete inhibition of cell attachment. In fact, HuH7, A549, and MDA-MB-436 cells were found to partially migrate on PEG coated surface parts created by µPIPP. Since these cells, nonetheless, preferentially adhere to fibronectin-coated adhesion sites, this property can lead to self organization-like phenomena.[161] In such processes, cells which are initially seeded randomly over the whole area of a micropatterned surface migrate erratically over PEGylated surface parts until they find and permanently attach to fibronectin-coated adhesion sites. Since this behavior seems to be in contrast to completely cell-repelling, covalently bound PEG layers[162], cell adhesion and migration on different types of PEG coating was systematically studied and compared to the behavior on fibronectin-coated surfaces.

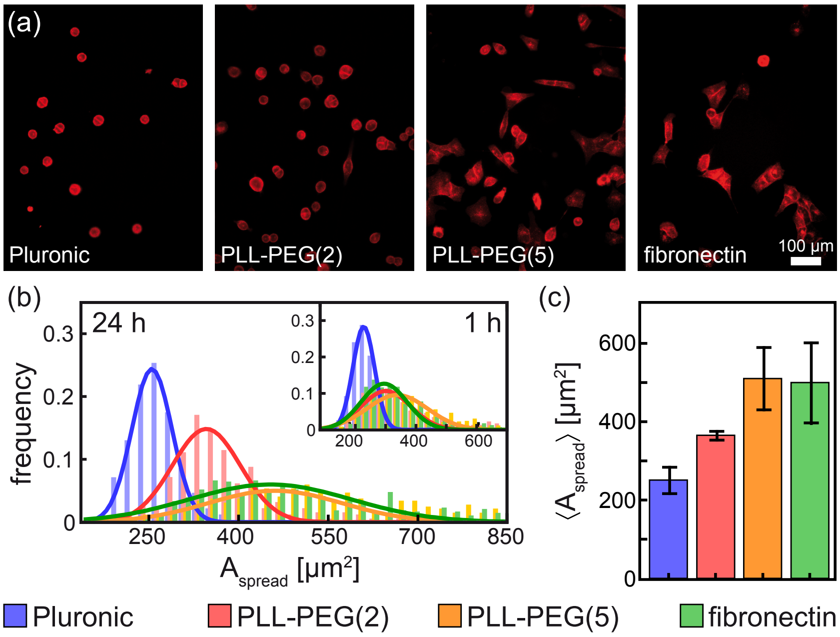

FIGURE 3.13.: Cell adhesion on PEGylated substrates and fibronectin. (a) False-color fluorescence images of plasma membrane labeled A549 cells 24 h after cell seeding on Pluronic coated, PLL-PEG(2) coated, PLL-PEG(5) coated, and uncoated COC substrates, all incubated with fibronectin. (b) Distribution of the cell spreading area, A_{spread}, on the different substrates 1 h (inset) and 24 h after cell seeding. (c) Mean spreading area per cell 24 h after cell seeding. Error bars indicate the standard deviation between the three conducted experiments. Figure adapted with permission from Reference [96]. Copyrighted 2014 by WILEY-VCH Verlag GmbH & Co. KGaA, Weinheim.

---

*This section is to a large part based on the publication by Röttgermann *et al.*[96].

The PEGylated substrates were fabricated using the two block-copolymers Pluronic and PLL-PEG, which both feature PEG chains (see Section 2.3 for detailed structure). Since PLL possesses a positively charged NH_3^+ group, it readily adsorbs to negatively charged surfaces via electrostatic interaction. In contrast, the hydrophobic PPO chain of Pluronic adsorbs to hydrophobic surfaces. Consequently, for the cell experiments described in this section, Pluronic was adsorbed from solution to an untreated and hence hydrophobic COC surface whereas for the adsorption of PLL-PEG, the COC substrate was activated via O_2-plasma exposure (analogously to the µPIPP protocol). In order to test the influence of PEG chain length on cell adhesion and migration, PLL-PEG polymers featuring PEG chains of 2 kDa (PLL-PEG(2)) and 5 kDa (PLL-PEG(5)) mass were used (PLL(20 kDa)-g[3.5]-PEG(2 kDa) and PLL(20 kDa)-g[3.5]-PEG(5 kDa)).

In a first set of experiments, the cell spreading area on the different substrates was analyzed. A large spreading area usually corresponds to flat-shaped cells and hence indicates strong adhesion to the substrate. In contrast, the small spreading area of roundish cells is a indicator for no or only weak cell-substrate adhesion. To estimate the spreading area, the plasma membrane was stained to highlight the cell shape and the area within the cell contour was evaluated.[1] Figure 3.13(a) shows the fluorescence image of stained adeno carcinoma cells (A549) 24 h after cell seeding on COC substrates coated with Pluronic, PLL-PEG(2), PLL-PEG(5), and fibronectin, respectively. On Pluronic and PLL-PEG(2), cells exhibited a roundish morphology, while on PLL-PEG(5) and fibronectin, cells generally showed a more flat and spread-out shape. For all tested coatings, the distributions of the spreading areas, A_{spread}, 1 h and 24 h after cell seeding are plotted in Figure 3.13(b). Already 1 h after cell seeding, the sharply peaked distribution for cells on Pluronic indicates the small spreading area of cells on this substrate. 24 h after cell seeding, the graph indicates slightly adherent cells on PLL-PEG(2) and well adherent cells on PLL-PEG(5) and fibronectin. This trend becomes also evident in the mean spreading area per cell on the different substrates (Fig. 3.13(c)).

In order to analyze the effect of the different coatings on cell motility, cell trajectories were extracted from time-lapse microscopy experiments (see Section A.4.1 for details). A set of typical cell trajectories for the different substrates is shown in Figure 3.14(a). The generally wider distance covered in the tracks on fibronectin and PLL-PEG(5) compared to PLL-PEG(2) indicates an increased motility on theses coatings. On Pluronic, cells showed no or only very weak cell-substrate adhesion and locomotion. In order to quantify this trend, the mean cell velocity was calculated as $v_{\mathrm{mean}} = \langle\langle|v_{\mathrm{i}}|\rangle_{\mathrm{track}}\rangle_{\mathrm{cells}}$, where v_{i} indicates the instantaneous cell velocity from one time-lapse image to the next, $\langle\ldots\rangle_{\mathrm{track}}$ is defined as the mean over the whole track of the corresponding cell, and $\langle\ldots\rangle_{\mathrm{cells}}$ indicates the mean over all cells evaluated on the corresponding substrate (Fig. 3.14(b)). As cells did almost not adhere to Pluronic, no proper migration analysis was possible on this substrate and the corresponding value of v_{mean}

---

[1] Note that a wide-field microscope was used and hence this measure evaluates the projection of the cell on the surface, which might slightly overestimate the actual cell-substrate contact area especially in the case of roundish, weakly adherent cells.

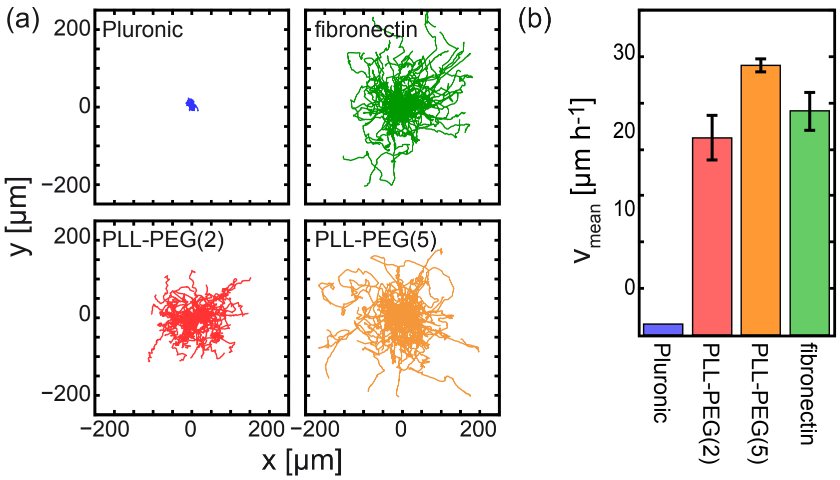

Figure 3.14.: Cell motility on PEGylated substrates and fibronectin. (a) Set of representative cell tracks of cells migrating for 24 h on substrates coated with Pluronic, PLL-PEG(2), PLL-PEG(5), and uncoated COC substrates, all incubated with fibronectin. (b) Mean cell velocity, v_{mean}, for cells migrating on the different coatings. Error bars indicate the standard deviation of the three conducted experiments. Figure adapted with permission from Reference [96]. Copyrighted 2014 by WILEY-VCH Verlag GmbH & Co. KGaA, Weinheim.

is close to zero. Interestingly, the highest value of v_{mean} was measured for cells migrating on PLL-PEG(5), whereas cells migrated slightly slower on PLL-PEG(2) as well as on fibronectin.

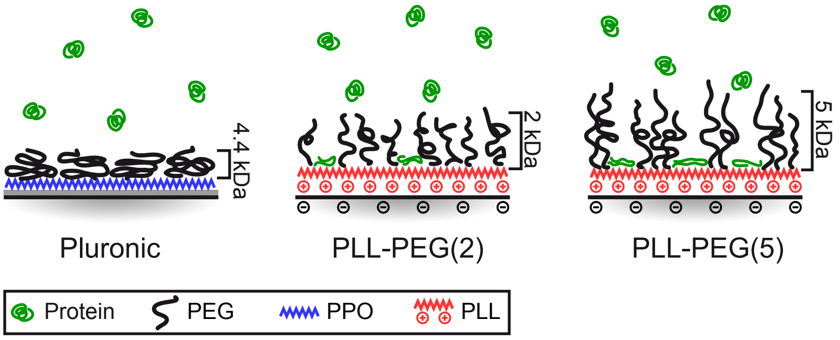

Figure 3.15.: Illustration of the protein adsorption to different types of PEG coating. For Pluronic coated substrates, the thin but dense PEG structure prevents protein adsorption almost entirely. The more elongated structure of the PEG chains of PLL-PEG polymers allows protein adsorption to the underlying PLL backbone or the substrate. The longer chains of PLL-PEG(5) might lead to a more disordered chain arrangement and hence increased protein adsorption compared to PLL-PEG(2). Figure adapted with permission from Reference [96]. Copyrighted 2014 by WILEY-VCH Verlag GmbH & Co. KGaA, Weinheim.

These findings show that PEG coatings based on PLL-PEG polymers are less cell-repellent than coatings based on Pluronic. In order to reveal eventual structural differences in the PEG layer causing this difference in affinity, neutron reflectivity measurements on PEG-coated silicon oxide blocks were conducted in the group of Bert Nickel (see Reference [96] for details). Indeed, a decreased PEG layer thickness ($< 28 \pm 1$ Å) and higher PEG density ($\sim 45\,\%$ water) for the 4.4 kDa PEG chains of Pluronic compared to the PEG layer thickness (68 ± 3 Å for

PLL-PEG(5) and 51 ± 1 Å for PLL-PEG(2)) and PEG density ($>$ 80 % water) of both PLL-PEG based coatings was measured. Furthermore, as illustrated in Figure 3.15, measurements before and after incubation with fibronectin indicated an adhesion of the protein to the PLL layer for PLL-PEG(2) ($\sim$ 72 fmol/cm^2) and PLL-PEG(5) ($\sim$ 127 fmol/cm^2) coated surfaces, while for Pluronic, no adhesion of fibronectin was detected. The low amount of fibronectin adhering to PLL-PEG(2) compared to PLL-PEG(5) is not entirely in accordance to literature, since in general, a higher PEG chain length is found to result in decreased protein adsorption.[95,163] However, depending on substrate, PEG chain length, and PLL-PEG grafting ratio, exceptions to the rule have been found before and were attributed to differences in the PEG chain conformation.[163] The increased protein adsorption to PLL-PEG(5) compared to PLL-PEG(2) may hence be the result of a more inhomogeneous arrangement of the PEG brushes for PLL-PEG(5) layers.

Taken together, the results of the neutron reflectivity measurements are in good agreement with the findings for cell adhesion and motility on the different coatings. The increased adhesion of fibronectin to PLL-PEG(5) and PLL-PEG(2) compared to Pluronic provides more accessible binding sites and hence enhanced cell spreading and motility. The observation of the highest migration speed on PLL-PEG(5) among all coatings is in accordance to literature, as peaked distributions of the cell velocity around an intermediate value for the fibronectin surface concentration have been reported already for fibroblasts and multi-potent stromal cells.[144,145,164] It is assumed that this effect derives from the fact that for a very low density of adhesion sites, the consequently weakly attached cells are not able to generate sufficient traction for effective locomotion, while for high adhesion site densities, the consequently strongly adherent cells are slowed down by breaking the comparatively large number of cell-substrate bonds.

The results of this section hence illuminate the effects of the PLL-PEG(2) coating used for µPIPP on protein adhesion and cellular behavior. While protein adhesion into the PLL-PEG(2) coating might provide sufficiently enough adhesion sites for cell attachment and migration, the coating is still clearly more cell-repellent than a fibronectin layer. In order to tune cell adhesiveness and/or achieve a cell repellence similar to the one observed for Pluronic coated substrates, PLL-PEG molecules of different grafting ratios and PEG chain lengths could be employed in future experiments.

CHAPTER 4

GUIDING MICROLANES TO STUDY AND CHARACTERIZE SINGLE-CELL MIGRATION*

Eukaryotic cell migration is a complex biomechanical process. The intricate interplay of processes like cellular polarization, actomyosin contractility, and the formation of focal adhesions results in migration patterns which depend on the cell type as well as on a cell's surrounding environment.[13–17] Deviations from typical migration patterns often indicate pathological conditions or pharmaceutical influences.

Hence, in order to characterize different cell types and detect anomalies in migration behavior, suitable metrics have to be found which characterize cell motility and its relation to environmental conditions. In addition, such metrics allow to parameterize and test theoretical models on a phenomenological basis. However, extracting characteristic and meaningful measures from individual cell tracks is a challenging task.

In this chapter, arrays of straight and ring-shaped microlanes are used as a platform to restrict single-cell migration to quasi-1D motion, thereby simplifying the assessment of characteristic phenomenological measures. Moreover, by introducing a PEGylated barrier into the track, the interaction of cells with chemical interfaces is analyzed.

4.1. MIGRATIONAL BEHAVIOR IN QUASI-1D ENVIRONMENTS

In order to probe and characterize cell migration in a standardized environment, arrays of ring-shaped lanes were created via µCP according to Section A.1.3[1] (Fig. 4.1(a)). The ring geometry was chosen for two reasons. Firstly, as can be seen in Figures 4.1(b) and 4.2, it

---

[*] This chapter is to a large part based on the publication by Schreiber and Segerer *et al.*[36].

[1] The enclosed form of the ring geometry does not permit a realization via µPIPP.

virtually reduces the degrees of freedom of a cell to one dimension (see movie c4_ring[165]). Secondly, in contrast to straight lanes, once isolated in a pattern, cells can migrate over large distances without leaving the field of view or colliding with other cells. This feature also prevents from getting a bias for the measured cell velocities due to the fact that faster cells leave the field of view more quickly.

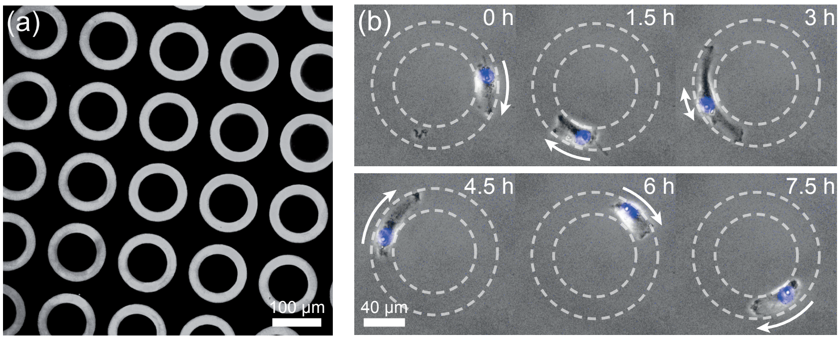

FIGURE 4.1.: Single-cell migration in ring-shaped micropatterns. (a) Fluorescence image of ring patterns composed of labeled fibronectin (bright) and a PEG coating (dark). (b) Phase-contrast time-lapse series of an MDA-MB-436 cell confined to a ring-shaped lane. The fluorescently labeled nucleus is shown in blue. The observed cell shapes can mainly be described by two prevailing morphologies: an asymmetric, polarized cell shape exhibiting a single lamellipodium at the cell front and the nucleus located at the rear, and an symmetric, elongated shape displaying two lamellipodia. Figure adapted with permission from Reference [36].

The width of the lane was chosen to be 20 µm, in which case cells exhibited a morphology closely resembling that of cells migrating on open 2D surfaces, but still were sufficiently guided such that the resulting tracks could be analyzed as a one-dimensional random walk along the lane.

By analyzing the morphology of MDA-MB 436 cells migrating within the patterns, two characteristic cell shapes were found to predominate. An asymmetric, polarized morphology exhibiting a single lamellipodium at the cell front and the nucleus located at the rear, and a more symmetric, elongated morphology displaying lamellipodia in both directions along the lane (Fig. 4.1(b)). In very rare cases, a third characteristic shape in form of a roundish morphology lacking lamellipodia was observed.

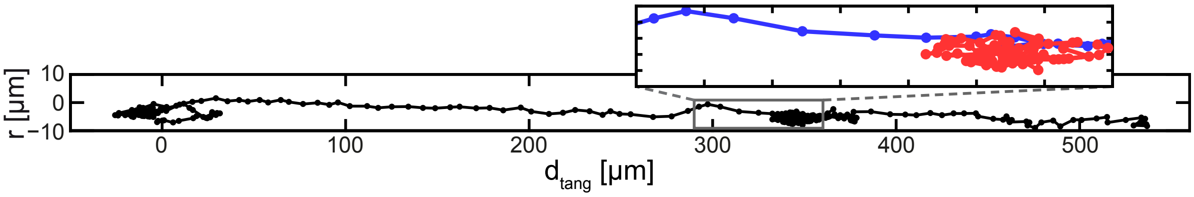

FIGURE 4.2.: Typical trajectory of an MDA-MB-436 cell confined within a ring-shaped micropattern. The radial cell position, r, of the nucleus is plotted against the tangential position, $d_{\text{tang}} = R \cdot \varphi$, where $R = 50$ µm denotes the mean radius of the ring lane and φ indicates the angular position of the nucleus. The zoom-in highlights periods of directionally persistent migration (blue) and periods of localized, erratic motion (red). Figure adapted with permission from Reference [36].

In the next step, the migration patterns of the cells within the lanes were analyzed. To this end, the cell nuclei were fluorescently stained, thereby enabling an automated tracking of the cell positions over time (see Section A.4.1 for details). In a typical cell track as the one shown in Figure 4.2, distinct phases of directional migration and localized random motions are discernible. As pointed out in Section 2.4.1, such multi-modality in cellular migration has been reported before.[127–129,166]

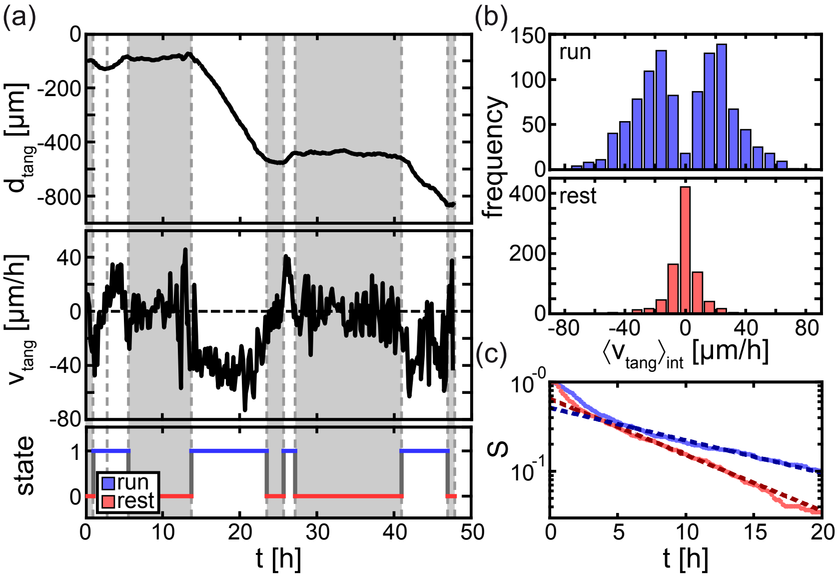

FIGURE 4.3.: Analysis of cell tracks and bimodal classification scheme. (a) For the cell track shown in Figure 4.2 are displayed: (top) The covered distance, d_{tang}, along the tangential direction of the ring-shaped lane, (middle) the tangential component of cell velocity, v_{tang}, and (bottom) the classification into run and rest states according to the algorithm described in Section A.4.2. (b) Distribution of the velocity in the tangential direction averaged over the individual run and rest intervals of more than 200 MDA-MB-436 cells. (c) Log-lin plot of the survival function, $S(t) = P(T > t)$, of the persistence times of the run (blue) and rest (red) states. Dashed lines indicate exponential fits. Figure adapted with permission from Reference [36].

In order to quantify the bimodality in the cellular motion observed within the tracks, a classification scheme that discriminates directional persistent run states from non-persistent rest states was implemented. The algorithm is based on cumulative sum (CUSUM) statistics and reveals and locates time points at which the fundamental trend of the cell velocity in the tangential direction along the ring track, v_{tang}, changes. Very similar approaches have been applied to identify trends in the fields of climate research or healthcare.[167–169] Once these change points in $v_{\mathrm{tang}}(t)$ are found, the mean squared displacement (MSD) of the cell motion within the interval between each set of adjacent change points is calculated. The scaling of the MSD with time is then used to classify the cell motion within the corresponding interval either as erratic (diffusive) motion or as directionally persistent (ballistic) migration (see Section A.4.2 for details on the classification scheme). The result of applying this classification scheme on the cell track depicted in Figure 4.2 is shown in Figure 4.3(a). Plotting the covered distance in tangential direction along the ring, d_{tang}, periods in which the cell migrates in a directionally persistent manner (run states) are represented by a continuous slope of $d_{\text{tang}}(t)$, while during periods in which cell motion is erratic (rest states), $d_{\text{tang}}(t)$ exhibits no, or at least no sustained, slope. By comparing the different regimes in the graph with the classification into run and rest states, it becomes evident that the two motion patterns are well dissected by the algorithm.

As a result of the bimodal analysis, the velocity of a cell can be analyzed separately for both migration modes. The distributions of the mean velocity, $\langle v_{\text{tang}} \rangle_{\text{int}}$, within the run and the rest states of over 200 analyzed MDA-MB-436 cells are shown in Figure 4.3(b). Here, v_{tang} denotes the instantaneous velocity (cell displacement from one frame to the next) in tangential direction along the ring track, while $\langle \ldots \rangle_{\text{int}}$ indicates the mean over all instantaneous velocities within a specific interval of the corresponding state. For the run states, the distribution of $\langle v_{\text{tang}} \rangle_{\text{int}}$ exhibits two peaks, corresponding to clockwise (cw) and counterclockwise (ccw) migration along the ring. As expected, the average velocity of the rest states is peaked at $\langle v_{\text{tang}} \rangle_{\text{int}} = 0$. The average absolute run velocity over all cells was evaluated as $v_{\text{run}} = \langle | \langle v_{\text{tang}} \rangle_{\text{int}} | \rangle_{\text{run}}$, where $\langle \ldots \rangle_{\text{run}}$ indicates the mean over all intervals classified as run state. For MDA-MB-436 cells, a run velocity of $v_{\text{run}} = 30.2 \pm 0.8$ µm/h was calculated. This value is considerably larger than the mean velocity, $v_{\text{mean}} = \langle \langle | v_{\text{tang}} | \rangle_{\text{track}} \rangle_{\text{cells}} = 25.2 \pm 0.8$ µm/h, where $\langle \ldots \rangle_{\text{track}}$ indicates the mean over the whole track of a cell and $\langle \ldots \rangle_{\text{cells}}$ denotes the mean over all tracked cells. This discrepancy between both measures is due to the fact that periods in which the cells are not moving or change direction very frequently do not contribute to v_{run}, but do contribute to v_{mean}. Hence v_{mean}, which is usually evaluated as a measure for the migration velocity in cell science, is biased by the directional persistence and consequently does not reflect the actual motion speed resulting from the running migration machinery.

To analyze the lifetime distribution of both states, and hence the persistence in cell motion, the survival function, $S(t) = P(T > t)$, was evaluated. Calculated as the fraction of run or rest states exceeding a time, t, this function gives an estimate on the probability, P, that the duration, T, of an arbitrary run or rest interval exceeds t. As shown in Figure 4.3(c), the survival function, $S(t)$, of both states is well fitted by an exponential function, $S(t) \propto e^{-t/\tau}$, at timescales exceeding 5 h. This exponential behavior of $S(t)$ suggests that the stochastic process underlying the emergence and collapse of both states is Poissonian. The deviation from this trend on shorter timescales might be due to other underlying biological processes like spatial fluctuations in the position of the nucleus with respect to the cell position or a decreased persistence of not yet fully polarized cells. Still, artifacts of the state classification algorithm cannot entirely be excluded. From the exponential fits on $S(t) : t > 5\,\text{h}$ for the run state and $S(t) : t > 2.5\,\text{h}$ for the rest state, the mean persistence times of both states were evaluated as $\tau_{\text{run}} = 13.6 \pm 0.5\,\text{h}$ and $\tau_{\text{rest}} = 6.5 \pm 0.2\,\text{h}$ (see Section A.4.3 for detailed calculations). Taken together, the migration behavior of a cell within the ring-shaped lanes is hence characterized by the three parameters, τ_{run}, τ_{rest}, and v_{run}.

4.2. MIGRATIONAL BEHAVIOR AT BARRIER ENCOUNTER

In order to gain a more detailed understanding on how a complex machinery like the cellular propelling system works, it is often useful to analyze its response to external disturbances. The eventual resulting adaption, break down, or re-initiation processes can yield additional measurable quantities and reveal more insights into the intrinsic working mechanisms than the sole observation of the smoothly running process. To apply such a disturbance to cellular migration, PEGylated barriers of different widths were introduced into the ring setup described in the last section (Fig. 4.4(a)). In doing so, we systematically analyzed and quantified the cell behavior at the encounter with a chemical barrier.

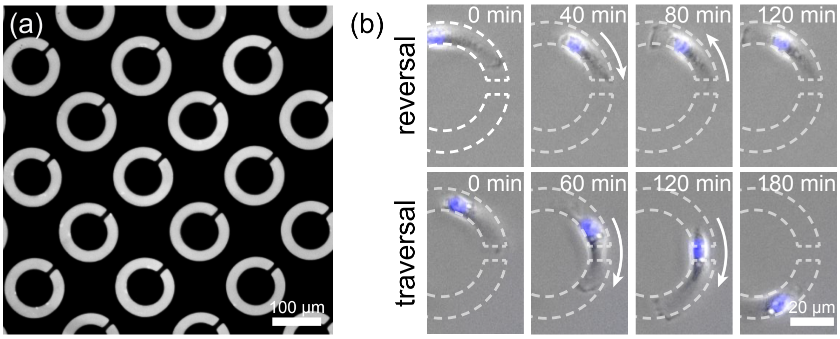

FIGURE 4.4.: Single-cell encounters with chemical barriers. (a) Fluorescence image of ring patterns composed of labeled fibronectin (bright) and a PEG coating (dark) featuring PEGylated barriers. (b) Phase-contrast time-lapse series of an MDA-MB-436 cell confined to the setup. The fluorescently labeled nucleus is shown in blue. When encountering the barrier, two different scenarios were observed. Either cell migration is stopped at the chemical interface and the cell starts to migrate in the opposite direction (reversal), or the cell is able to overcome the barrier (traversal). Figure adapted with permission from Reference [36].

For a cell encountering the chemical barrier, two possible outcomes were observed: either cell migration ceased at the interface before the cell started to migrate back in the opposite direction, or the cell was able to overcome the barrier and continued migrating (see movies c4_gap and c4_gap_2[165]). Typical examples for both scenarios are depicted in Figure 4.4(b). The chance of a resulting reversal at a barrier encounter led to an increased probability of finding a cell in the rest state close to the barrier. In contrast, the probability to find a cell in the run state decreased in the vicinity of the barrier. Both observations become evident in the graph shown in Figure 4.5. As depicted in Figure 4.6(a), the analysis of several hundred cell-barrier encounters revealed that the probability for a cell to traverse the barrier, P_{trans} (see Section A.4.3 for the detailed calculation), decreased with increasing width of the the barrier, d_{gap}. $P_{\mathrm{trans}}(d_{\mathrm{gap}})$ is well fitted by an exponential distribution:

$$P_{\mathrm{trans}}(d_{\mathrm{gap}}) = 1 - P_{\mathrm{turn}}(d_{\mathrm{gap}}) = [1 - P_{\mathrm{turn}}(0)] \cdot \exp\left(\frac{-d_{\mathrm{gap}}}{\mu_{\mathrm{trans}}}\right). \tag{4.1}$$

Here, $P_{\mathrm{turn}}(d_{\mathrm{gap}})$ indicates the probability for a cell to turn around encountering a barrier of width d_{gap} (see Section A.4.3 for detailed calculation). Since also spontaneous reversals of migration direction in the absence of a barrier were observed, $P_{\text{turn}}(0) > 0$ is valid. Hence, $P_{\text{trans}}(d_{\text{gap}})$ is smaller than unity also for $d_{\text{gap}} = 0$. The decay length of the exponential fit was found to be $\mu_{\text{trans}} = 8.3 \pm 2.3\ \mu\text{m}$, where the error denotes the 95 % confidence interval of the fit.

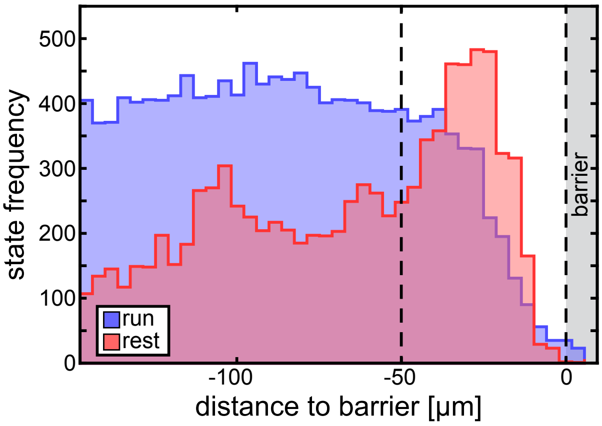

FIGURE 4.5.: The presence of a barrier affects the representation of run and rest states in cell motion. Frequency of cells found in the run or rest state as a function of the distance (along the ring pattern) between the cell and a barrier of 19 µm width. While in general, cells are found more frequently in the run state, in the interval from around 50 µm distance to the barrier interface, the probability to find a cell in the rest state increases considerably. Figure adapted with permission from Reference [36].

The exponential scaling of $P_{\text{trans}}(d_{\text{gap}})$ might directly emerge from the typical invasion depths of the lamellipodium of a cell into a PEGylated surface area. In order to test this hypothesis, the invasion of the cell into PEGylated areas was studied in a blind-alley pattern geometry as depicted in Figure 4.6(b). To capture the relatively fast dynamics of the lamellipodium, a higher temporal resolution (time between images $\Delta t = 5\,\text{sec}$) than for the other migration experiments described in this thesis ($\Delta t = 10\,\text{min}$) was used in these studies. Using this setup, the maximal invasion depths, d_{inv}, of 32 encounters of MDA-MB-436 cells with fibronectin/PEG interfaces were measured. The survival function, $S_{\text{inv}}(d) = P(d_{\text{inv}} > d)$, indicating the fraction of invasion depths, d_{inv}, exceeding a given distance, d, is shown in Figure 4.6(c). Similar to P_{trans} (Eq. 4.1), the survival function was well fitted by an exponential:

$$S_{\text{inv}}(d) = S_0 \cdot \exp\left(\frac{-d}{\mu_{\text{inv}}}\right). \tag{4.2}$$

The resulting typical invasion depth of $\mu_{\text{inv}} = 11.8 \pm 1.0\ \mu\text{m}$ is of similar to the exponential decay length of the survival function for the barrier traversals, $\mu_{\text{inv}} = 8.3 \pm 2.3\ \mu\text{m}$. It hence seems reasonable to argue that the invasion depth of the lamellipodium determines the capability of a cell to overcome a PEGylated barrier. All cells analyzed in this set of experiments penetrated at least two µm into the PEG coated area. This length is of similar magnitude as the typical distance from the tip of the lamellipodium to the region at which the first focal adhesions are formed in the process of cell migration.[170,171] The inability to form new focal adhesions on the PEG layer might therefore trigger the cease in the locomotion of a cell approaching the interface.

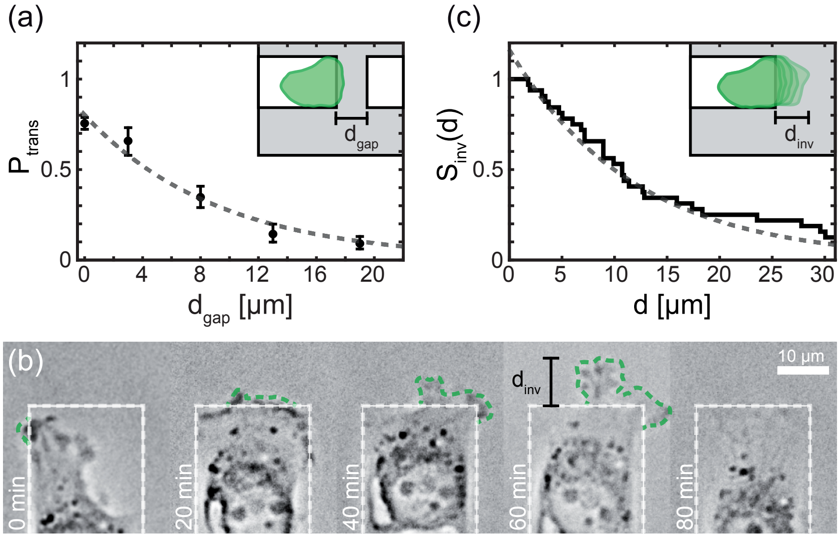

FIGURE 4.6.: Analysis of barrier-traversal probabilities and invasion into PEGylated areas. (a) Fraction, P_{trans}, of cell-barrier encounters resulting in barrier traversals as a function of the barrier width, d_{gap}. The dashed line indicates an exponential fit according to Equation 4.1. (b) Time-lapse images of a cell turning around at the chemical interface between fibronectin and PEG coated surface parts in a blind-alley lane pattern. The contour of the part of the lamellipodium invading the PEGylated area is highlighted by the green dashed line. The maximal invasion depth, d_{inv}, of this encounter is indicated. (c) Survival function, $S_{\text{inv}}(d) = P(d_{\text{inv}} > d)$, for the fraction of barrier encounters that resulted in a maximal invasion depth, d_{inv}, greater than a given distance, d. The dashed line indicates an exponential fit according to Equation 4.2. Figure adapted with permission from Reference [36].

The exponential distribution of $P_{\text{trans}}(d_{\text{gap}})$ as well as of $S_{\text{inv}}(d)$ indicates that the process underlying the invasion of a cell into a PEGylated surface part might be Poissonian in nature. This suggests that, analogously to the run and rest states observed for cell migration in the absence of a barrier, within each segment of migrated distance (or time interval) into the PEGylated region, the probability for the lamellipodium (or cell) to cease protruding is the same (for segments of the same length). Hence, the persistence of lamellipodium protrusion, and consequently cell motion, seems decreased on PEG surfaces compared to fibronectin coated surfaces.

4.3. MOTION ASSESSMENT AND THE MIGRATIONAL FINGERPRINT

The analysis of cell migration in closed ring-shaped micropatterns yielded three parameters describing cell motion: the migration velocity, v_{run}, quantifying the speed of a migrating cell in the run state, as well as τ_{run} and τ_{rest}, describing the characteristic lifetimes of the run and rest states, respectively. The extension of the setup by integrating a PEGylated barrier can be used to extend this set of parameters by P_{trans} (or P_{turn}), quantifying a cell's ability to invade a cell-repellent area. To this end, the fraction of cell encounters with barriers of 8 µm width resulting in reversals of migration direction, $P^{8}_{\mathrm{turn}} = P_{\mathrm{turn}}(d_{\mathrm{gap}} = 8\,\mu\mathrm{m})$, is used in this work. The choice of $d_{\mathrm{gap}} = 8\,\mu\mathrm{m}$ is due to the fact that at this barrier width the barrier is sufficiently wide to induce a clear increase in P_{turn} as compared to no barrier present, while it is still sufficiently narrow such that barrier traversals are observed frequently. In order to give information on the impact of the barrier on the reversal probability, P^{8}_{turn} has to be compared to the reversal probability in the absence of a barrier, $P^{0}_{\mathrm{turn}} = P_{\mathrm{turn}}(d_{\mathrm{gap}} = 0\,\mu\mathrm{m})$. Furthermore, P^{0}_{turn}, provides additional insights into cell behavior as it gives information on the tendency of a cell to change its direction of motion (this information is not included in τ_{run}, since the migration direction does not necessarily change when two run states are interrupted by a rest state).

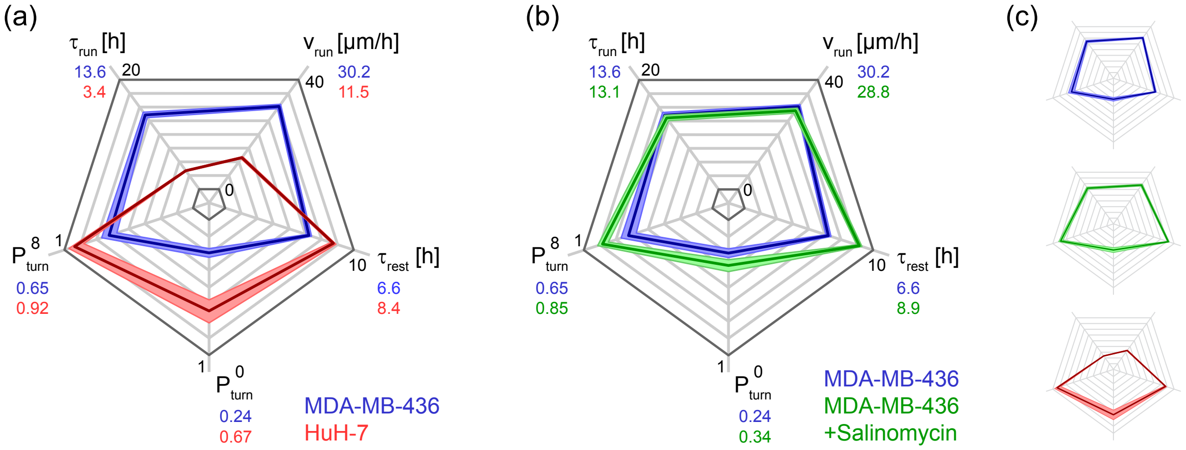

Figure 4.7.: Fingerprint-like characterization of cell migration. Using a radar chart, we compare: the run velocity, v_{run}, the typical duration of the rest state, τ_{rest}, the probability for a cell to turn around in the absence of a barrier, P^{0}_{turn}, the probability for a cell to turn around at a barrier of 8 µm width, P^{8}_{turn}, and the typical duration of the run state, τ_{rest}. The axes are arranged such that an overall downward shift of the polygon corresponds to decreased motility. (a) Comparison of MDA-MB-436 and HuH7 cells. (b) Comparison of MDA-MB-436 cells treated and untreated with 50 nM salinomycin. (c) Characteristic polygons shapes in the radar plot for of MDA-MB-436 cells (blue), MDA-MB-436 cells treated with salinomycin (green), and HuH7 cells (red). Figure adapted with permission from Reference [36].

Together, these five parameters build a characteristic signature of the migratory behavior of a cell type. This fingerprint-like characterization can be illustrated using radar charts similar to the ones used to visualize morphological and structural cellular properties[172]. To compare the migratory behavior of mesenchymal MDA-MB-436 cells to that of HuH7 cells, which are more epithelial in character, the corresponding plots are shown in Figure 4.7(a). The longer run persistence, the lower rest persistence, and the considerably higher run velocity of the MDA-MB-436 cells indicates the overall higher motility of this cell line. Additionally, the

MDA-MB-436 cell line exhibits a substantially lower probability for spontaneous direction reversals as well as for direction reversals induced by a barrier. MDA-MB-436 cells are hence more likely to overcome a cell-repellent barrier than HuH7 cells. This finding is in agreement with the invasive character of MDA-MB-436 cells compared to the low invasiveness of HUH7 cells.[173–175]

In addition to comparing different cell types, the multi-parameter assessment provided by the setup can also be used to characterize and quantify the effect of drugs on the migratory behavior of a cell. As an example, the effect of the anti-cancer drug candidate salinomycin was tested in the course of this thesis. From literature, salinomycin is known to reduce the overall velocity as well as the directionality of cell migration on 2D surfaces.[176] The results of experiments using salinomycin treated MDA-MB-436 cells in our setup are shown in Figure 4.7(b). It becomes evident that salinomycin has almost no effect on the run velocity as well as on the run persistence. However, the reversal probability in the absence as well as in the presence of a barrier are both increased by the drug. Moreover, the typical duration of a rest state is increased for salinomycin treated cells. These findings indicate that salinomycin does not affect the actual machinery propelling the cell but hampers the transition from the unpolarized (rest) state into the polarized (run) state. Since salinomycin is known to increase the global calcium concentration within a cell[177,178], which in turn affects the establishment of cell polarity[179–181], this effect seems reasonable. The multiparameter analysis used here hence yields a more detailed and comprehensive description of the effects of salinomycin on cell migration than a simple assessment of the mean cell velocity.

In the radar plot representation used here, changes in the overall motility of a cell are indicated by a shift of the corresponding polygon. The axis are chosen such that an increase in motility is indicated by an upward shift of the polygon. To highlight the emerging characteristic “fingerprint” for different cell types and the slight changes induced by salinomycin, the polygon shapes are compared in Figure 4.7(c). This type of visualization hence yields the advantage that the migrational “character” of a cell type can readily be grasped by the shape and position of the corresponding polygon.

Taken together, the results of this chapter so far show that arrays of ring-shaped micropatterns are a suitable platform to study cell motility. The bimodality found in the migration patterns of the observed cell lines is well captured and quantified by the implemented analysis. Furthermore, the inclusion of a PEGylated barrier into the setup extends the set of parameters by an additional quantity measuring the liability of the migrating cell to an external obstacle. Hence, the detailed characterization of the migration assay in combination with high-throughput time-lapse acquisition and automated cell tracking provides a step towards a standardized platform for the assessment of single-cell migration and the development of phenotypic descriptors.

4.4. ENDOTHELIAL CELL MIGRATION IN STRAIGHT LINES*.

The bimodal classification scheme introduced in the last sections can be used for the detailed assessment and quantification of effects induced by environmental conditions and migration-related pharmaceutics. For this purpose, the analysis scheme was applied to migration experiments conducted at the LMU department of pharmacy in the group of Stefan Zahler[37]. In these experiments, the migration of HUVECs on micropatterns consisting of straight, fibronectin coated lanes of different widths in a PEGylated surrounding was analyzed.

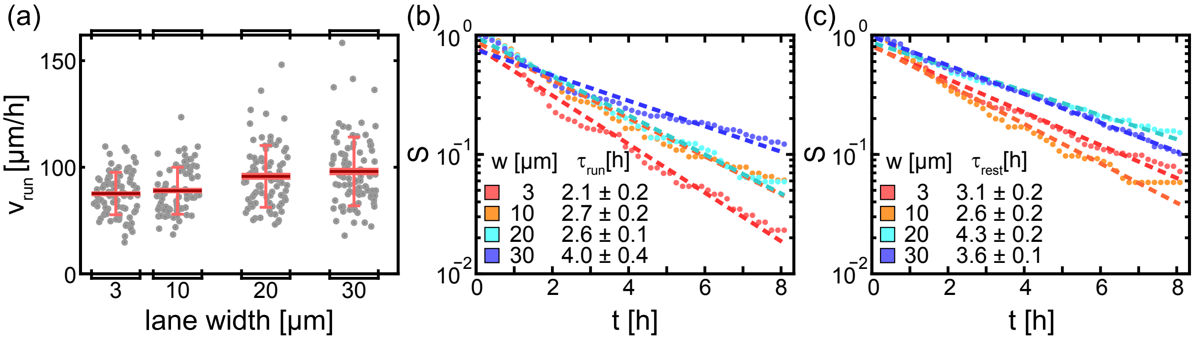

FIGURE 4.8.: HUVEC migration on lanes of different widths. (a) Boxplot of the run velocity of HUVECs on lanes of 3 µm, 10 µm, 20 µm, and 30 µm width, respectively. Grey dots indicate the average run velocity of individual cells, dark red lines indicate the mean run velocity, light red boxes indicate the standard error of the mean, and whiskers indicate the standard deviation. (b) Log-lin plot of the survival function, $S(t) = P(T > t)$, of the persistence times of the run states for different lane widths. Dashed lines indicate exponential fits. (c) Log-lin plot of the survival function of the persistence times of the rest states for different lane widths. Dashed lines indicate exponential fits. The errors for the corresponding mean persistence times,τ_{rest} and τ_{rest}, are evaluated as the 95 % confidence interval of the fit.

In a first set of experiments, cell migration was analyzed on lane patterns of different widths. Figure 4.8(a) shows the run velocity, v_{run}, for HUVECs migration on stripes of 3 µm, 10 µm, 20 µm, and 30 µm width. As can be seen, the migration speed increases with increasing width of the lane. This result is in contrast to the migration behavior of fibroblasts, for which a decrease in the (mean) migration velocity with increasing lane width was reported[41], but in accordance to other studies on HUVECs[182]. As shown in Figure 4.8(b), also the migration persistence of HUVECs was found to increase with increasing lane width. For the typical duration of the rest state no clear trend with the width of the lane was observed (Fig. 4.8(b)). Taken together, these results indicate, nonetheless, that the decreased adhesion area provided by narrower micropatterns reduces the mobility of HUVECs.

In a next set of experiments, the effects of different pharmaceutics affecting myosin and actin activity on HUVEC migration were tested. The corresponding results for blebbistatin, calycolin-A, and Y-27632 are shown in Figure 4.9. While all three drugs induced a slight increase in the typical duration of the rest state, they had different effects on run velocity as well

---

*This section is to a large part based on the publication Schuster *et al.*[37]

(a) blebbistatin:

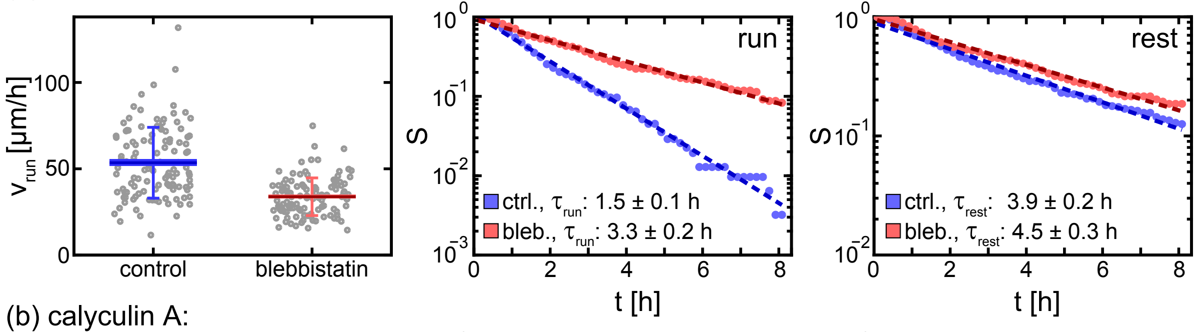

(b) calyculin A:

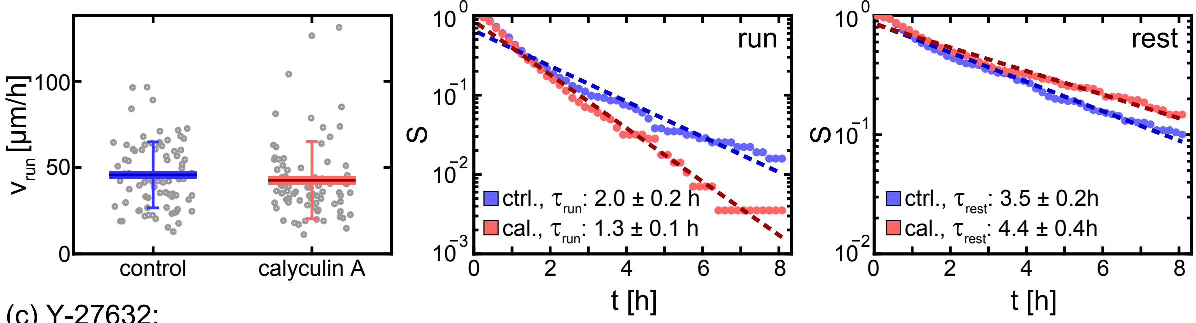

(c) Y-27632:

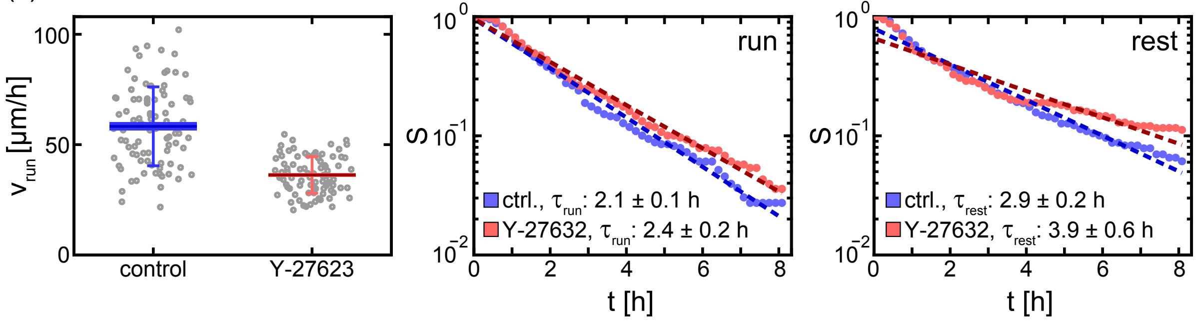

FIGURE 4.9.: Effect of blebbistatin (bleb.), calyculin A (cal.), and Y-27623 on HUVEC migration in lanes of 3 µm width. (left column) Boxplot of the run velocity for the corresponding controls (blue) and drug-treated cells (red). Grey dots indicate the average run velocity of individual cells, dark lines indicate the mean run velocity, light boxes indicate the standard error of the mean, and whiskers indicate the standard deviation. (middle column) Log-lin plot of the survival function, $S(t) = P(T > t)$, of the persistence times of the run states for the controls (blue) and drug-treated cells (red). Dashed lines indicate corresponding exponential fits. (right column) Log-lin plot of the survival function of the persistence times of the rest states for the controls (blue) and drug-treated cells (red). Dashed lines indicate corresponding exponential fits. The errors for the corresponding mean persistence times,τ_{rest} and τ_{rest}, are evaluated as the 95 % confidence interval of the fit.

as on the run persistence. Blebbistatin, which is known to inhibit myosin[183,184], was found to decrease run velocity while simultaneously increasing the directional persistence of migration (Fig. 4.9(a)). In contrast, calycolin-A treatment, which has been reported to promote myosin activity and contractility[185,186], decreased directional persistence while having almost no effect on the run velocity (Fig. 4.9(b)). Treatment with Y-27632, which inhibits Rho-associated protein kinase (ROCK), a key regulator of actin organization[187], had only small effect on the run persistence but decreased the run velocity considerably (Fig. 4.9(c)).

Taken together, these findings suggest that myosin-induced cell contractility is a regulator of velocity and directional persistence in cell migration, while inhibition of actin assembly mainly effects migration speed. In fact, the decreased persistence induced by increased contractility was suggested to be the consequence of a stronger representation of cell morphologies characterized by increased cell blebbing.[37] Furthermore, the results show that migration speed and migration persistence are affected contrarily by pharmaceutics like blebbistatin and hence contradict studies which postulate a universal coupling between both quantities[13,42]. The suggestion of such universal coupling was based on experiments in which the (instantaneous) mean velocity, v_{mean}, of the cell tracks was used to measure the migration speed. As discussed in Section 4.1, the value of v_{mean} is influenced by the number of changes in direction (and resting periods) within the observed track, and consequentially can not be considered independent of the directional persistence. The bimodal analysis introduced in this chapter does not suffer from this drawback and hence gives a more detailed picture of the migration process.

CHAPTER 5

COLLECTIVE CELL MIGRATION IN CIRCULAR MICROPATTERNS*

In the previous chapter, micropattern arrays used as a platform to study and quantify single-cell migration were presented and discussed. Although such a setup gives a good impression on the basic properties of cellular motion and is well-suited to characterize and dissect different cell types and pharmaceutical or pathological effects, it omits an important aspect of cell motion: What happens if one cell encounters another? What are the basic rules of cell-cell interaction? How does collective behavior in cell migration emerge from the properties of an individual cell?

Addressing these questions, one of the objectives of this thesis was to systematically study the transition from the erratic motion of a single cell to the coordinated migration of multicellular assemblies. In order to accomplish this task, a setup was needed in which collective cell migration could be observed for assemblies of small, controllable numbers of cells. Furthermore, to quantify collectivity in the system, the setup had to be suitable to narrow down the rich phenomena in which collective cell migration can manifest to motion patterns providing clear measurable quantities.

One rather generic pattern often emerging from the collective motion of self-propelled objects is a coherent angular motion (CAMo) resulting in the formation of so-called swirls or vortices. Such rotational states have been observed in the migration of eukaryotic cells[39,188,189] and bacterial colonies[190–192] as well as in the motion of driven filaments[193,194] and granular materials[195,196]. Huang *et al.*[43] showed that for two adherent, migrating cells the environment of a circular-shaped micropattern induces persistent rotational motion. In a variation of this setup, Doxzen *et al.*[44] as well as Deforet *et al.*[45] used larger circular patterns to study the emergence of collective rotation and its dependence on cell density for assemblies composed of up to several hundred cells. In the course of this thesis, circular patterns of intermediate size between these setups were used to systematically study the emergence and persistence of the collective rotational motion of small cell assemblies in dependence on the number of

---

*This chapter is to a large part based on the publication Segerer and Thüroff *et al.*[38].

participating cells. As layer-forming and collectively migrating epithelial cells, Madin-Darby canine kidney (MDCK) cells are the classic cell line used in studies on collective cell migration.[10,18,20,27,39,44,45,76] In order to provide comparability to these studies, MDCK cells were used for the experiments described in this chapter.

5.1. Spontaneous Onset of Collective Rotation

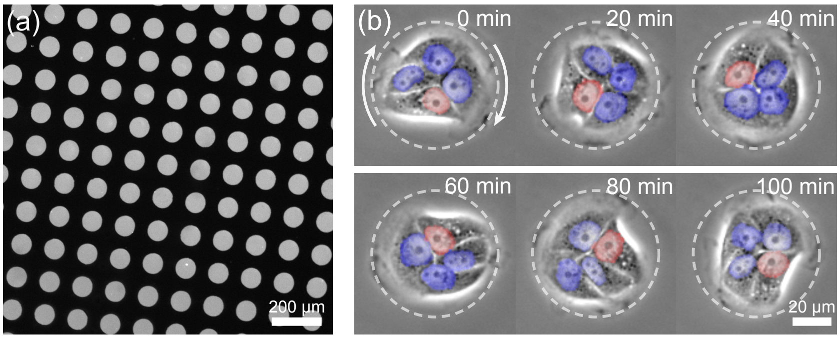

Figure 5.1.: Collective cell migration in circular-shaped micropatterns. (a) Fluorescence image of circle patterns composed of labeled fibronectin (bright) and a PEG coating (dark). (b) Phase-contrast time-lapse series of four MDCK cells confined to a circle-shaped pattern. The false color of one of the fluorescently labeled nuclei is changed to red instead of blue in order to highlight the collective rotational motion.

As depicted in Figure 5.1(a), the experimental setup used here consisted of arrays of circular micropatterns composed of fibronectin and PLL-PEG created via µPIPP according to Section A.1.4. Figure 5.1(b) illustrates the emergent CAMo for a group of four cells confined in such a pattern. In order to study the properties of this CAMo as a function of the cell number, circular fields of different diameters were designed to accommodate two to eight cells at a constant cell density of approximately 830 $\mu\text{m}^2/\text{cell}$ (Fig. 5.2). Consequently, for each pattern size, only fields containing the appropriate number of cells were selected for further analysis. We observed CAMo for all analyzed cell numbers (see movies concerning the experimental part of this chapter[165]). The cell nuclei were stained and time-lapse movies were recorded with a temporal resolution of 6 frames/h. Afterwards, the individual nuclei were tracked using the algorithm described in Section A.5.1.

For each cell, c_i, where $i \in \{1, \dots, N\}$ for a circular field containing N cells, the individual angular position, $\varphi_i(t)$, of the geometric center of mass of the nucleus with respect to its initial position, $\varphi_i(0) = 0$, was evaluated as illustrated in Figure 5.3 (see Section A.5.2 for detailed calculations). As depicted in Figure 5.3(b), periods of distinct motion patterns are discernible in the time courses of $\varphi_i(t)$. Periods where all $\varphi_i(t)$ exhibit a similar slope correspond to a common angular velocity of all cells within the system and hence resemble periods of CAMo. Eventually, such rotational states are interrupted by periods in which the time evolutions of $\varphi_i(t)$ show no common trend or exhibit almost no slope at all. In such periods of disordered

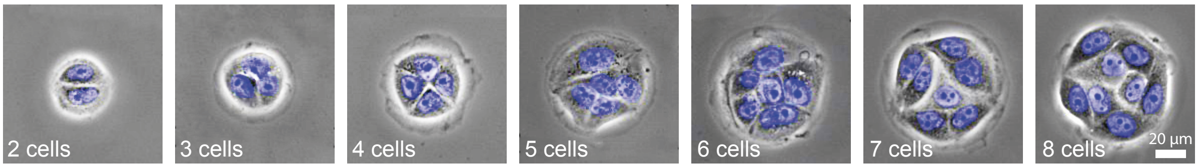

FIGURE 5.2.: Circular micropatterns occupied by two to eight cells. The size of the evaluated patterns was increases in line with cell number such that the average area provided for each cell remained constant at approximately 830 µm^2. The fluorescently labeled nuclei are shown in blue. Figure adapted with permission from Reference [38]. Copyrighted by the American Physical Society.

motion (DisMo) the confined cells do not migrate collectively in azimuthal direction. The uncoordinated cell movements within periods of DisMo can in turn spontaneously align, resulting in an anew period of CAMo in arbitrary direction.

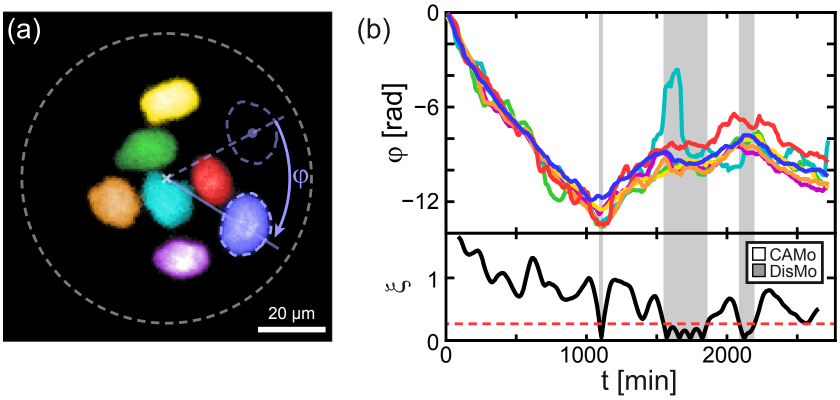

FIGURE 5.3.: Cell tracking and classification of motion states. (a) False-color fluorescence image of the nuclei of seven cells within a circular micropattern. For each cell, c_i, the angular position, $\varphi_i(t)$, was evaluated with respect the cell's initial angular position, $\varphi_i(0) = 0$ (see Section A.5.2 for detailed calculations). (b) Angular positions, $\varphi_i(t)$, of each cell (in colors corresponding to the colors of the nuclei in (a)) and normalized total angular velocity, $\xi(t)$, according to Equation 5.2. The classification threshold of $\xi_c = 1/4$ is indicated by the red dashed line. Periods classified as DisMo are highlighted in gray. Note that the pronounced peak of the cyan-colored curve at around 1600 min results from the fact that the corresponding cell migrates in close vicinity of the common rotation axis (see Section A.5.2 for details). Figure adapted with permission from Reference [38]. Copyrighted by the American Physical Society.

5.2. CLASSIFICATION OF MOTION PATTERNS

In order to study and quantify the overall rotational motion in the system, the system angular velocity, $\Omega_N(t)$, was calculated by taking the mean over the individual angular velocities of all cells within the system smoothed over a number of frames, n_f:

$$\Omega_N(t) = \frac{1}{N \cdot n_f^2 \cdot \Delta t} \sum_{i=1}^{N} \sum_{\tau=t}^{t+n_f} [\varphi_i(\tau) - \varphi_i(\tau - n_f)]. \tag{5.1}$$

Here, $\Delta t = 10\,\text{min}$ indicates the time interval between two successive frames of the time-lapse measurements. The smoothing over n_f successive frames was performed to filter out small fluctuations which result, for example, from displacements of the nucleus with respect to the geometric center of a cell. As a trade-off between smoothing of fluctuations and temporal resolution, the length of the smoothing interval was chosen to be $n_f = 9$.[1]

TABLE 5.1.: Number of analyzed systems for different cell numbers.

Cells per system	2 cells	3 cells	4 cells	5 cells	6 cells	7 cells	8 cells
Number of analyzed systems	124	115	95	89	64	63	56

In order to distinguish periods of CAMo from periods of DisMo, the probability distribution, $P(|\Omega_N|)$, was calculated and analyzed from the evaluation of sample sizes according to Table 5.1 for each cell number. As depicted in Figure 5.4(a), $P(|\Omega_N|)$ is approximately Gaussian for all cell numbers. With increasing cell number, the maximum of the fitted Gaussian distribution, $\overline{\Omega}_N$, is shifted towards slower rotation speeds. This slower rotation speed of larger cell assemblies can be explained by geometry-based reasoning. As can be seen in Figure 5.4(b), the distribution of the average velocity, v_{CAMo}, of the fastest cell during a period of CAMo shows no clear trend with the number of cells in the system. This indicates, that during CAMo the outermost cells in average migrate with a similar velocity for all cell numbers, N. Since the outermost cells of larger assemblies (systems) are further away from the common rotation axis (system center), this results in slower rotation speeds for higher cell numbers. Also, the standard deviation, σ_N, of $P(|\Omega_N|)$ decreases with increasing number of cells in the system. This feature might partly be due to the fact that cells adjust their velocity to one another, canceling out outliers in migration speed. In addition, this trend is certainly due to the fact that Ω_N is calculated as an average over the number of cells in the system, whereby individual faster or slower migrating cells do contribute more for lower cell numbers. Together, the decrease of $\overline{\Omega}_N$ and σ_N with increasing number of cells in the system results in a similar coefficient of variation $\sigma_N/\overline{\Omega}_N = 0.74 \pm 0.13$ for all cell numbers.

On closer examination, it becomes clear, however, that $P(|\Omega_N|)$ is not entirely described by a single Gaussian function but exhibits a weak second maximum around $\Omega_N = 0$. This second maximum indicates the state of DisMo in which no coherent rotation is observed in the system. Introducing a normalized variable,

$$\xi_N(t) = |\Omega_N(t)/\overline{\Omega}_N|, \tag{5.2}$$

a common threshold of $\xi_{\text{th}} = 1/4$ was defined for all cell numbers, N, such that for $\xi_N(t) < \xi_{\text{th}}$ the motion within a system was classified as DisMo, whereas for $\xi_N(t) \geq \xi_{\text{th}}$ it was classified

---

[1] The migration of a cell in close vicinity of the common rotation axis can lead to artifacts in $\varphi(t)$ as evident in Figure 5.3(b). Therefore, the cell closest to the rotation axis was dynamically excluded in the calculation of $\Omega_N(t)$ (see Section A.5.2 for details). Data analysis using $n_f = 4$ or $n_f = 15$ had no substantial qualitative influence on the results (data not shown).

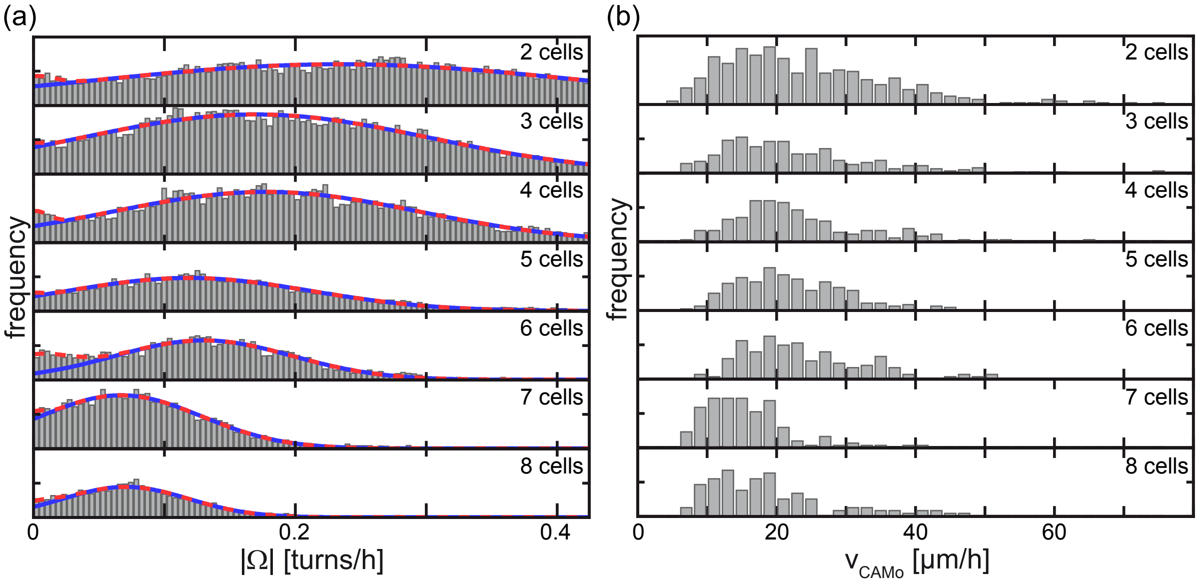

FIGURE 5.4.: Velocity distributions. (a) Distribution of the absolute mean angular velocity, $|\Omega_N|$, for systems containing two to eight cells. The distributions, $P_N(|\Omega_N|)$, are fitted by a single Gaussian function (blue) and a mixture of two Gaussian functions (dashed red). The deviation between the two curves reveals a second maximum at $\Omega_N = 0$ for most cell numbers. (b) Distribution of the mean velocity, v_{CAMo}, of the fastest cell during a period of CAMo. Figure adapted with permission from Reference [38]. Copyrighted by the American Physical Society.

as CAMo (Fig. 5.3(b)).[2]

In order to verify that the two states obtained via the threshold, ξ_{th}, are truly distinct with regards to the migration behavior of the cells, we calculated the angular MSD within each state as:

$$\mathrm{MSD}(t) = \langle[\langle\varphi_i(t)\rangle_N - \langle\varphi_i(0)\rangle_N]^2\rangle_{\mathrm{int}}. \tag{5.3}$$

Here, $t = 0$ signifies the starting point of the corresponding interval, while the averages, $\langle\ldots\rangle_N$ and $\langle\ldots\rangle_{\mathrm{int}}$, were taken over all N cells within a system and over all observed intervals of CAMo or DisMo, respectively. In Figure 5.5, the time evolution of $\mathrm{MSD}(t)$ within periods of CAMo and DisMo is shown in log-log representation. It can be seen that within periods of CAMo, $\mathrm{MSD}(t) \propto t^2$ holds true for all cell numbers, indicating "ballistic", and hence persistent, angular motion. In contrast, within periods of DisMo, $\mathrm{MSD}(t) \gtrsim t$, indicating rather "diffusive", and hence erratic, motion in azimuthal direction. Together, these findings illustrate that the CAMo/DisMo classification scheme as described above is suitable to dissect the different migration patterns within a system (rather than just dissecting periods of slow rotation from periods of faster rotation).

---

[2] As this classification scheme via a threshold in $\xi_N(t)$ is rather heuristic, an alternative approach to dissect periods of CAMo from periods of DisMo was also tested to crosscheck the presented results and diminish the risk of drawing wrong conclusions due to artifacts of the algorithm. This alternative approach and its results, which are in agreement with the results of the classification via ξ_{th} shown in this chapter, are shown in Section A.5.4 of the supplement.

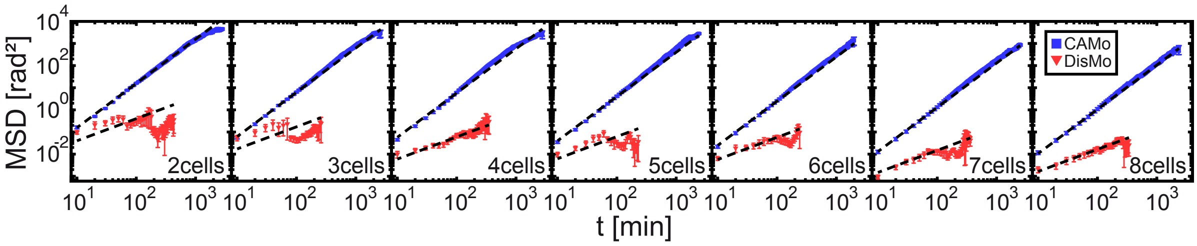

FIGURE 5.5.: Characterization of cell motion within states of CAMo and DisMo. Log-log plot of the angular MSD calculated according to Equation 5.3 for periods of CAMo (blue) and DisMo (red) and for assemblies consisting of two to eight cells. Black dashed lines indicate a slope of one ($\propto t$) or two ($\propto t^2$), respectively. Error bars indicate the standard error of the mean. Figure adapted with permission from Reference [38]. Copyrighted by the American Physical Society.

5.3. DISTRIBUTION OF ROTATION DIRECTIONS

The onset of CAMo in an assembly of non or rather isotropic polarized cells can be considered as a symmetry breaking event. This symmetry break can potentially result in a clockwise (cw) or a counterclockwise (ccw) rotation of the confined cells. The presented setup can hence be used to reveal an eventual intrinsic bias towards one of these rotation directions in the emergence of vortex states in cell migration.

In order to check if such a trend is present in the system, the direction of rotation within periods of CAMo was evaluated for all cell numbers. As depicted in Figure 5.6(a), CAMo periods showing cw rotation appeared slightly more frequently than those showing rotation in ccw direction. This bias was observed for systems of all analyzed cell numbers, N. Summing over all states of CAMo regardless of the number of involved cells, 839 periods showed cw rotation, while 753 periods showed ccw rotation. Assuming a null hypothesis of an equal probability to rotate in cw or ccw direction, resulting in a binomial distribution for the probability density, this result corresponds to a p-value of 0.033 an hence can be considered significant.

Still, the risk of drawing false conclusions due to a bias in the experimental setup or the data evaluation scheme should always be considered when evaluating subtle trends. One assumption that potentially might not be entirely fulfilled here is that the individual periods of CAMo observed in the time course of a single system are statistically independent. If the rotation direction within a period of CAMo is affected by the proceeding CAMo period, this condition is not met. In order to crosscheck if the observed bias towards cw rotation is merely due to a correlation of the individual states of CAMo within a system, the data was additionally evaluated such that the rotation directions within the individual systems, rather than the direction of CAMo states within the time course of a system, were treated as stochastically independent measures. Figure 5.6(b) shows the frequency of analyzed systems exclusively rotating in cw or ccw direction and those alternating between both rotation directions. With 164 systems solely rotating in cw direction, 105 systems solely rotating in ccw direction, and 337 systems changing the direction of rotation at least once, the trend towards cw rotation is also evident

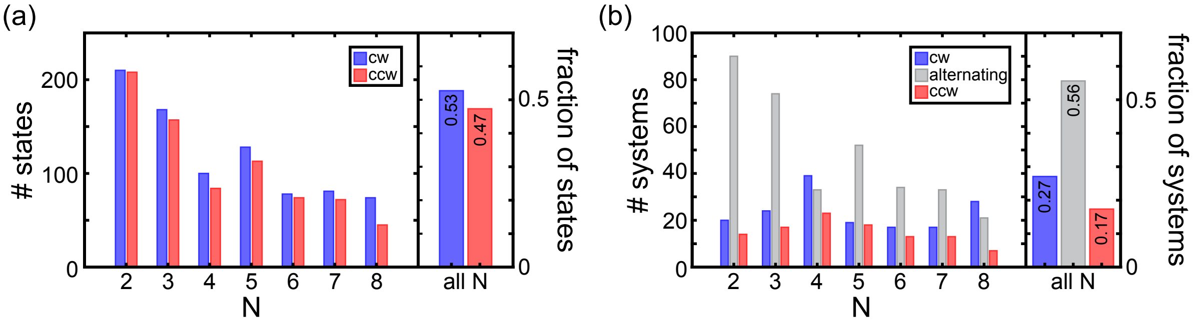

FIGURE 5.6.: Distribution of the direction of rotation. (a) Frequency of CAMo states showing clockwise (blue) or counterclockwise (red) rotation for systems containing $N = 2 \dots 8$ cells. The overall fraction of CAMo periods in the respective direction is plotted to the right. (b) Frequency of analyzed systems rotating solely in clockwise (blue) or counterclockwise (red) direction during periods of CAMo and systems that show at least one CAMo period for each direction (gray) for systems containing $N = 2 \dots 8$ cells. The overall fraction of systems showing the respective behavior is plotted to the right.

in this way of analysis (p-value < 0.01 if systems changing their rotation direction are not considered). Although a systematic bias resulting from subtle inhomogeneities in the experimental conditions can never be entirely excluded, these results strongly suggest an intrinsic chirality in cell migration.

Such left-right asymmetries are a known phenomenon in the development of organs and whole organisms.[197–199] However, how they emerge on the scale of individual cells and below is still unknown. The studies of Wan *et al.*[200] and Chen *et al.*[201] revealed a bias in cell alignment at mechanical and chemical interfaces. Whether these asymmetries favored cw or ccw alignment was found to be dependent on the corresponding cell type. Furthermore, drugs interfering with actin function were found to be capable of reversing these asymmetries for certain cell types. The involvement of the actin apparatus in the emergence of left-right asymmetries is also backed up by studies that reveal asymmetries in the self-organization of the actin cytoskeleton within micropatterns.[202] In these studies the emergence of the asymmetries is suggested to be a consequence of the polar and helical properties of actin filaments. Also here, the expression level of the aktin-crosslinking protein α-actinin-1 was found to affect the handedness of the observed chiral patterns.

The fact that MDCK cells were not tested for intrinsic chirality in all these studies makes a direct comparison to the observations of this thesis impossible. Still, the results presented in this section show that the used setup is suitable to detect cell-intrinsic asymmetries and reveals a directional bias in the migration of MDCK cells.

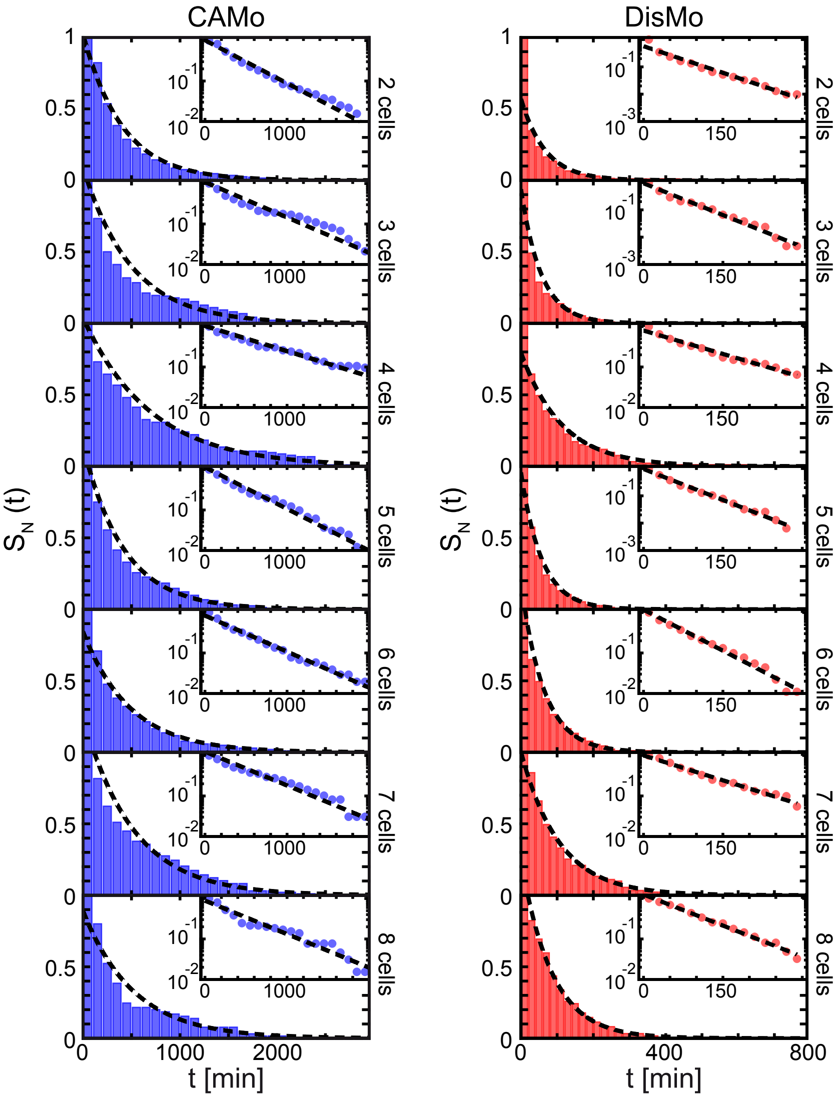

FIGURE 5.7.: Distribution of the lifetimes of states showing CAMo and DisMo. Survival function, $S_N(t) = P_N(T > t)$, of states showing CAMo (blue) and DisMo (red). Insets show corresponding log-lin plots. Black dashed lines indicate exponential fits. Figure adapted with permission from Reference [38]. Copyrighted by the American Physical Society.

5.4. PERSISTENCE OF CAMO AND DISMO STATES

In the beginning of this chapter, the circular pattern was introduced as a setup to study how the number of participating cells affects the emergence and persistence of collectivity in cell migration. In order to approach this question and find suitable measures to grasp collectivity in the system, we evaluated the lifetimes of periods showing CAMo or DisMo, respectively.

Figure 5.7 shows the survival function, $S_N(t) = P_N(T > t)$, indicating the fraction of CAMo or DisMo periods of a duration, T, exceeding a time t for systems containing two to eight cells. For both states and all analyzed cell numbers, the survival functions are well-fitted by an exponential function, $S_N(t) \propto e^{-t/\tau}$. This finding suggests that the process underlying the emergence and collapse of both states is Poissonian, implying a constant decay probability for each state.

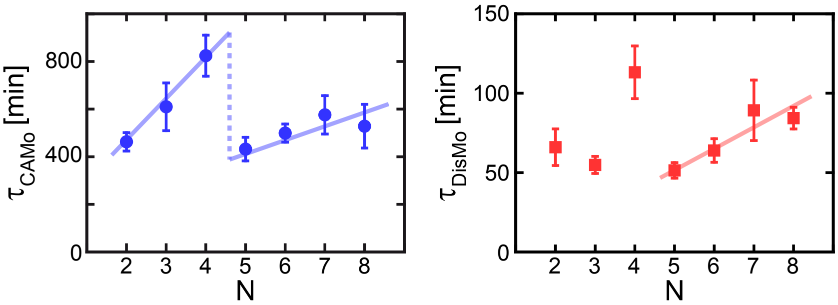

FIGURE 5.8.: Average lifetime of motion states. Mean persistence times, τ, as a function of the cell number, N, for states of CAMo (blue) and DisMo (red). Values are derived from the exponential fits of the survival functions shown in Figure 5.7. Error bars indicate confidence bounds of 99 % within the fits. Lines serve to highlight eventual trends. Figure adapted with permission from Reference [38]. Copyrighted by the American Physical Society.

The exponential behavior of $S_N(t)$ allows to evaluate the average lifetimes, τ_{CAMo} and τ_{DisMo}, of the respective states. Their corresponding values as a function of the number of cells in a system are plotted in Figure 5.8. The persistence time of the coherent state, $\tau_{\mathrm{CAMo}}(N)$, shows an increasing tendency with increasing cell number, interrupted by a pronounced discontinuity between systems containing four and systems containing five cells. For $\tau_{\mathrm{DisMo}}(N)$, an increasing trend with increasing cell number is only distinguishable for systems containing five to eight cells, while for $N = 2 \ldots 4$ no clear trend can be identified. Still, in accordance with $\tau_{\mathrm{CAMo}}(N)$, the most pronounced drop-off is observed between four- and five-cell systems.

5.5. COMPARISON TO NUMERICAL MODELING

So far, it remains to be shown that the phenomena observed for MDCK cells in micropatterns as discussed in the last section are generic and do naturally emerge from the interaction of polarizable and interacting cells in a circular confinement geometry. Furthermore, an explanation for the trends in the lifetimes of the CAMo and DisMo states is not yet at hand. Hence, in order gain a more fundamental understanding of the dynamics within the system, a computational model for cellular migration was developed by Thüroff *et al.*[203,204] and used to simulate cell migration in circular confinements.

The model is a generalization of the cellular Potts model (CPM) which is extended to account for an intracellular polarization as well as intercellular communication via mechanotransduction. In brief, the dynamics of the cell internal polarization field is coupled to the protrusions and retractions of the cell boundaries over a finite signaling range. This feature results in a feedback loop between intracellular polarization and external mechanical stimuli (see Section A.6 for more details and Reference [203] for a comprehensive description of the model). To find a suitable set of parameters for the model, sampling was performed by varying cell-cell adhesion strength, the signaling range over which mechanical stimuli affect the cell internal polarization field, and the strength of cytoskeletal forces relative to contractile forces (see Section A.6).

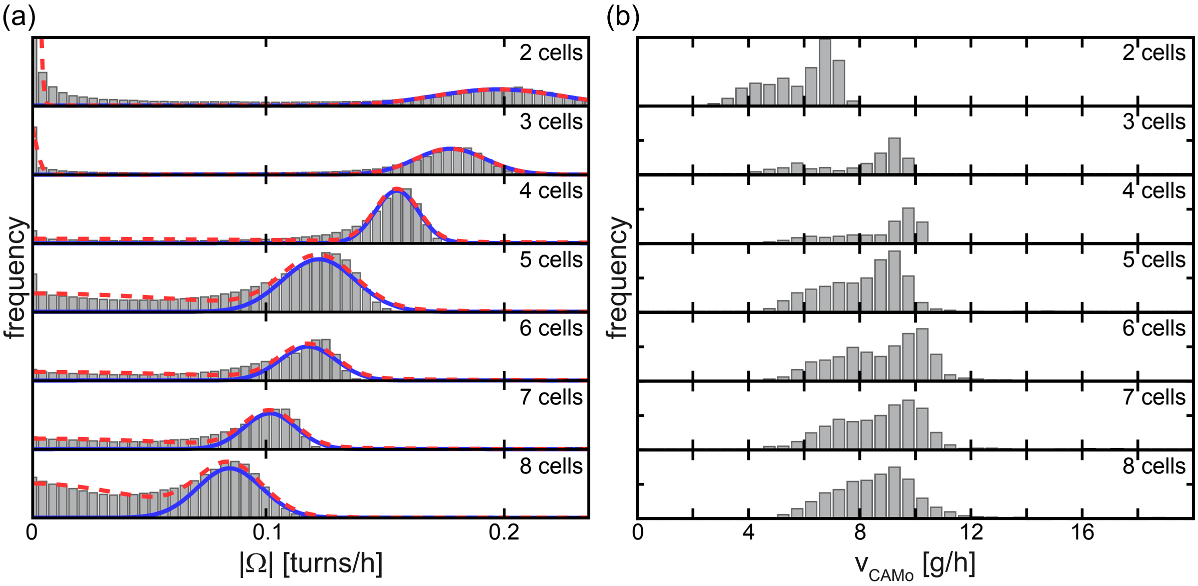

FIGURE 5.9.: Velocity distributions for the simulation runs. (a) Distribution of the absolute mean angular velocity, $|\Omega_N|$, for systems containing two to eight cells for the data obtained from the CPM. The distributions, $P_N(|\Omega_N|)$, are fitted by a single Gaussian function (blue) and a mixture of two Gaussian functions (dashed red). Note that for $N = 2$, the y-scale was chosen such that the maximum at $\Omega = 0$ is well above the field of view of the graph in order to provide visibility of the peak corresponding to CAMo at around $|\Omega| = 0.2$. (b) Distribution of the mean velocity, v_{CAMo}, of the fastest cell during a period of CAMo obtained from the CPM. g is defined as the distance between two grid sites. Figure adapted with permission from Reference [38]. Copyrighted by the American Physical Society.

The modeling approach was applied to simulate from two to eight cells within a circular confinement. For each cell number, N, 100 simulation runs of 10000 Monte Carlo steps (MCSs) each were performed. We found periods of CAMo as well as periods of DisMo represented in the motion patterns within the simulation runs (see movies concerning simulation runs[165]). The resulting tracks of the centers of mass of the individual cells were evaluated and analyzed analogously to the cell tracks obtained in experiment. In agreement to the experimental data, the distribution of the absolute system angular velocity, $|\Omega_N|$, shows two peaks corresponding to CAMo and DisMo (Fig. 5.9(a)). Again, the peak position corresponding to CAMo shifts to slower angular velocities with increasing number of cells in the system. As for the experimental data, this shift can be explained from geometry-based arguments due to the increased distance of the outermost cells from the system center. As seen in Figure 5.9(b), the mean velocity, v_{CAMo}, of the fastest cell during a period of CAMo is approximately the same for all cell numbers, $N > 2$. For $N = 2$, slightly slower migration speeds are observed which are most likely due to the dynamic adaptation of the polarization direction necessary for the migration in small circles. It is likely that in the simulation runs a cell migrating in these small patterns is not able to fully polarize due to the fact that the migration direction is constantly changing. As the circle size increases, the migration direction is changed more slowly and consequently more time is given for each cell to establish a strong internal polarization, resulting in faster migration speeds. In contrast to the experiment, the distribution of the absolute system angular velocity, $|\Omega_N|$, shows no clear trend for the width of the CAMo peak. Furthermore, for systems containing but a small number of cells ($N = 2, 3$) the peak at $\Omega = 0$, corresponding to DisMo, seems strongly pronounced. Closer examination of the simulation runs of such systems revealed that this increased representation of the DisMo state is due to a deadlocked configuration appearing in some of the runs (see movies c5_sim_2c and c5_sim_3c[165]). In these configurations, all cells within the system are polarized in the radial direction, pointing away from the system center, leading to an overall arrest of cell motion.

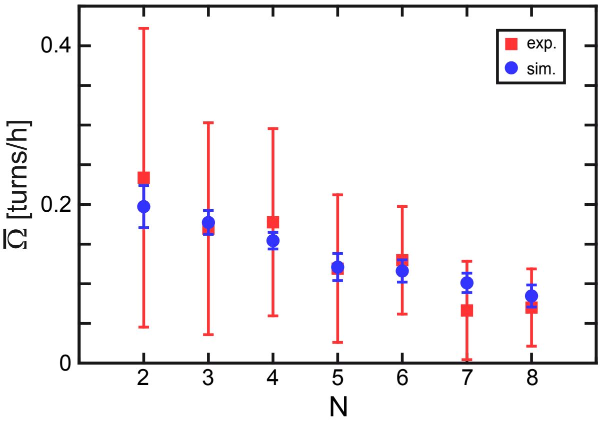

FIGURE 5.10.: Adjustment of MCS to real time. The positions of the peaks corresponding to CAMo, $\overline{\Omega}_N$, in the distribution of the system angular velocity, $P_N(|\Omega_N|)$, plotted against the number of cells, $N = 2 \ldots 8$, in the system for experiment and CPM. Error bars indicate the standard deviation. The translation of MCSs to real time was performed so that the best match for all peak positions was achieved. This matching resulted in a conversion of 1 MCS = 1.85 min. Figure adapted with permission from Reference [38]. Copyrighted by the American Physical Society.

Adjustment of the MCSs of the model to real time was performed such as to achieve the best match for the peak positions corresponding to CAMo, $\overline{\Omega}_N$, between numerical simulations and experiment. As illustrated in Figure 5.10, this matching resulted in a conversion of 1 MCS = 1.85 min.

Next, we dissected states of CAMo from states of DisMo by applying the same threshold of $\xi_{\text{th}} = 1/4$ as used for the experimental data. To check whether this classification scheme results in states of distinct motion patterns, the angular MSD was evaluated according to Equation 5.3 for each state. In Figure 5.11, the corresponding curves of the MSD are presented in log-log representation. Consistently, a slope corresponding to persistent rotational motion is observed for the MSD(t) within the CAMo state, while the MSD(t) within states of DisMo exhibits a slope corresponding to diffusive to sub-diffusive motion in azimuthal direction. Interestingly, the MSD of CAMo indicates a super-ballistic regime at around $t \cong 100$ min for all cell numbers. This characteristic shape of the MSD function might indicate a period of acceleration in the rotational motion, which can be explained by the dynamics of the cell internal polarization field. At timescales prior to the acceleration period, cells within the system are already aligned with regards to their internal polarization fields (resulting in CAMo) but have not yet reached their maximal degree of polarization. As CAMo goes on, the feedback between physical motion and intracellular polarization results in an increase in the degree of polarization of each cell and hence in the overall rotation velocity. This trend ceases when all cells in the system reach their maximal degree of polarization and the overall rotation consequently stabilizes at a constant angular velocity (since following a circular path, each cell adapts the direction of its internal polarization axis dynamically and hence this maximal degree of polarization does not necessarily correspond to a polarization to the implemented limit of q/Q (see Section A.6) for the polarization field at the cells rear/front, but might as well be limited by the speed of the adjustment to the direction of motion). For the MSD(t) of DisMo, the cease of motion resulting from deadlocked configurations manifests in a sub-diffusive regime at longer timescales for systems of small cell numbers.

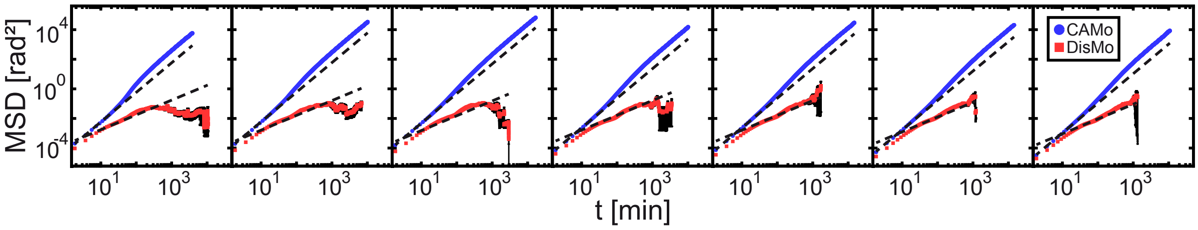

FIGURE 5.11.: Characterization of cell motion within periods of CAMo and DisMo for the simulation data. Log-log plot of the angular MSD calculated according to Equation 5.3 for periods of CAMo (blue) and DisMo (red) and assemblies consisting of two to eight cells. Black dashed lines indicate a slope of one ($\propto t$) or two ($\propto t^2$), respectively. Error bars indicate the standard error of the mean. Figure adapted with permission from Reference [38]. Copyrighted by the American Physical Society.

Next, the rotation direction as well as the lifetimes of the migrational states were evaluated. As to be expected, no significant left-right asymmetry manifesting in a bias towards cw or ccw direction was observed for the CAMo states of the simulations. The survival functions, $S_N(t)$, of both states are shown in Figure 5.12. In agreement with the experimental data, the lifetime distributions of the CAMo states exhibit exponential shape for all cell numbers. For states of DisMo, $S_N(t)$ generally shows exponential character, but for small cell numbers, it shows different trends on short and long timescales. This behavior is highlighted in Figure 5.13, where the survival functions of the DisMo states are plotted over a longer time period. Most evident for systems containing two to three cells, $S_N(t)$ decreases more slowly for $t \gtrsim 1000$ min than on short timescales. This second regime is due to the deadlocked configurations observed in the simulations. It can be seen that once such a configuration has established, it can take over

6000 min (> 3000 MCSs) until the system repolarizes into a state of CAMo. For higher cell numbers, no second regime in $S_N(t)$ is observed and the longest DisMo states observed do not exceed 4000 min ($\cong$ 2150 MCSs).

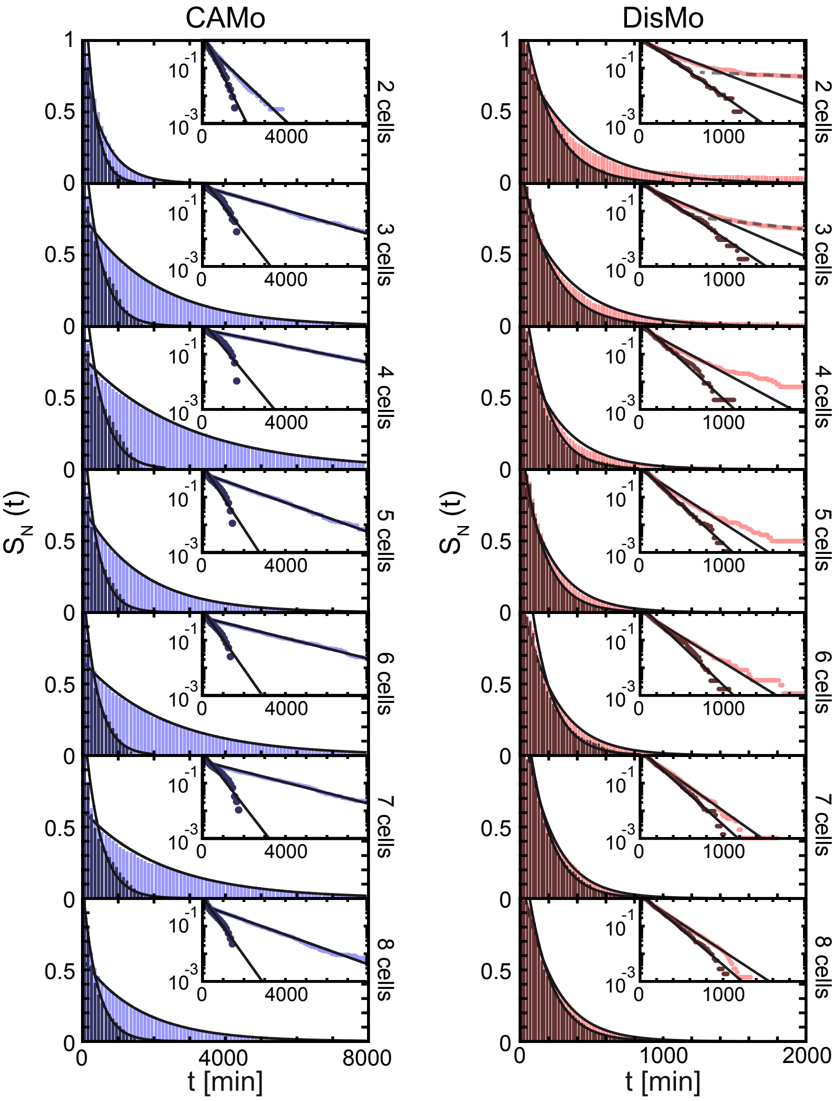

FIGURE 5.12.: Distribution of the lifetimes of motion states for the data obtained from the CPM. Survival function, $S_N(t) = P_N(T > t)$, of states showing CAMo (blue) and DisMo (red) for systems containing $N = 2 \ldots 8$ cells. Insets show corresponding log-lin plots. Black lines indicate exponential fits. The survival times are evaluated for the full length (of 10000 MCSs = 18500 min) of the corresponding simulation runs (light blue/light red) and for simulation runs which were constrained to the average experimental observation times for each cell number according to Table 5.2 (dark blue/dark red). For small N, the survival function of the DisMo states for the full simulation runs exhibits two regimes, manifesting in a change of the slopes in the log-lin representation (highlighted by dashed lines in the insets for $N = 2, 3$). The exponential fits for the the DisMo states are hence calculated solely in the interval of $t = 1, \ldots, 1000$ min. Figure adapted with permission from Reference [38]. Copyrighted by the American Physical Society.

The average lifetimes of the CAMo states show a similar qualitative trend with cell number as observed for the experimental data. In Figure 5.14 it can be seen that τ_{CAMo} increases with the cell number for $N = 2 \ldots 4$. In accordance to the experimental results, a clear drop off in CAMo persistence is observed between systems containing four and systems containing five cells. For $N \geq 5$, no clear trend in $\tau_{\text{CAMo}}(N)$ is discernible. $\tau_{\text{DisMo}}(N)$ shows a decrease with cell number for $N = 2 \ldots 5$. This trend can most likely be attributed to the contribution of deadlocked states for small cell numbers. Similar to $\tau_{\text{CAMo}}(N)$, no trend of $\tau_{\text{DisMo}}(N)$ is discernible for $N \geq 5$.

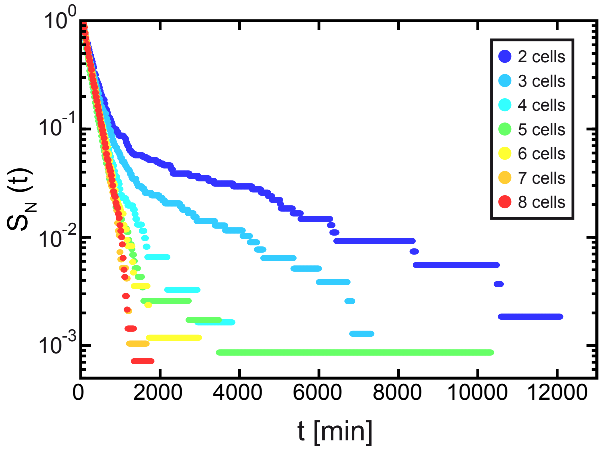

FIGURE 5.13.: Survival function of states showing DisMo for systems containing $N = 2 \ldots 8$ cells in log-lin representation.

In general, the lifetimes, τ_{CAMo} and τ_{DisMo}, evaluated from the simulation data exceed the lifetimes observed in experiment. This finding might not necessarily be attributed to more stable periods of CAMo or DisMo in the simulations, but might be due to the shorter timescales a system is observed in experiment. Since all systems are analyzed at a constant number of cells, N, the time-span between two cell divisions limited the period over which a system was analyzed in experiment. In order to check if and how this limited observation time effects the lifetimes, τ_{CAMo} and τ_{DisMo}, the simulation runs were artificially restricted to the observation times as given in Table 5.2 and analyzed analogously to the the full runs. The corresponding survival functions are plotted in Figure 5.12. As to be expected, for both states, the resulting lifetimes are closer to the ones observed in experiment (Fig. 5.14). For $\tau_{\text{CAMo}}(N)$ the increasing trend for $N = 2 \ldots 4$, as well as the discontinuity between $N = 4$ and $N = 5$ are still well represented. While not present in the data of the full simulation runs, the increasing trend of $\tau_{\text{CAMo}}(N)$ for $N = 5 \ldots 8$, as it was observed in experiment, is present in the data of the shortened simulation runs. (It might be important to mention, however, that the survival functions $S_N(t)$ for the restricted simulation runs are not as well fitted by an exponential function as they are for the full runs. Such small relative shifts in $\tau_{\text{CAMo}}(N)$ should hence not be overinterpreted.) The lifetimes of the DisMo state for restricted simulation runs show no clear trend with cell number except for an increased lifetime for $N = 2, 3$, which is most likely due to deadlocked configurations.

Taken together, the experimentally observed cell motion is well-reproduced by the numerical

TABLE 5.2.: Average time a system is observed in experiment.

Cells per system	2 cells	3 cells	4 cells	5 cells	6 cells	7 cells	8 cells
Mean observation time [min]	1760	1850	1820	1670	1570	1940	1680

simulations. In both systems, stochastic switching between collective rotation and disordered motion, exhibiting exponentially distributed persistence times is observed. However, the tendency of the simulated systems to fall into a deadlocked cell conformation is yet a feature which has not been observed in experiment and complicates the comparison and interpretation of the DisMo lifetimes. An adjustment of the parameters used for the CPM might help to overcome such conformations in future simulation runs. For the rotational state, however, experiment and simulation exhibit very similar trends in the rotation persistence as a function of the cell number. For both datasets, an increase of $\tau_{\mathrm{CAMo}}(N)$ for systems containing two to four cells is observed, which is followed by a drop off in persistence between $N = 4$ and $N = 5$.

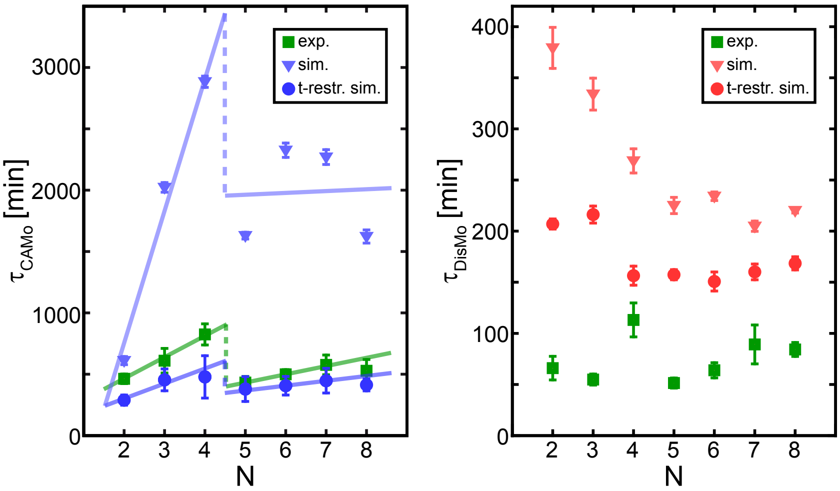

FIGURE 5.14.: Average lifetime of the motion states observed in the simulation. Mean lifetimes, $\tau_{\mathrm{CAMo/DisMo}}$, as a function of the cell number, N, for experiment and simulations based on the CPM. For the simulation data, triangles indicate results derived from the analysis of the full simulation runs, while for the data indicated by circles the observation time of the simulation runs was restricted to the average observation times of the experiments as given in Table 5.2. All values are derived from the exponential fits of the survival functions shown in Figure 5.7 and Figure 5.12. Error bars indicate confidence bounds of 99 % within the fits. Lines serve to highlight eventual trends. Figure adapted with permission from Reference [38]. Copyrighted by the American Physical Society.

5.6. INTERPLAY OF CELLULAR ARRANGEMENT AND COUPLING OF POLARIZATION

So far, the dependence of the state lifetimes, τ_{CAMo} and τ_{DisMo}, on the number of cells confined to the system has only been discussed on a descriptive level. The reason behind the observed general increase in CAMo persistence with cell number and its drop-off for systems containing more than four cells are not yet identified.

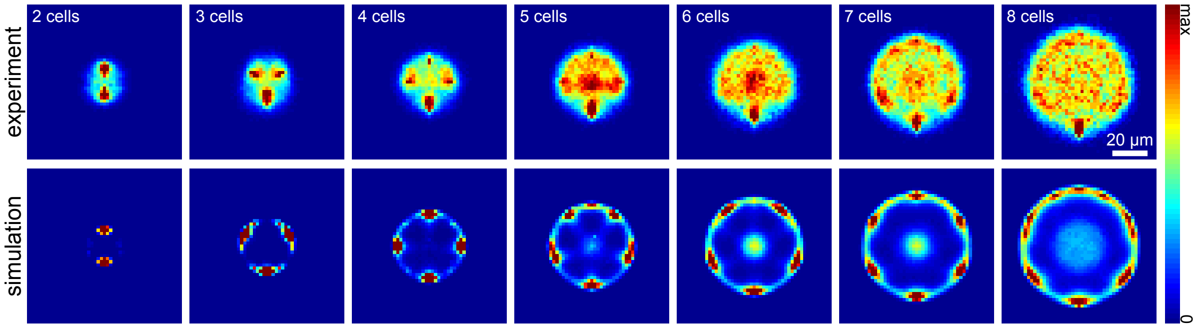

FIGURE 5.15.: Relative arrangement of cells within the micropatterns for experiment and numerical modeling. Heat map of the relative positions of the cells with respect to a reference cell position at the lower border of the system (see Section A.5.3 for details on the plot generation). Figure adapted with permission from Reference [38]. Copyrighted by the American Physical Society.

In order to get a better understanding of the dynamics in the system and to reveal the mechanisms behind these observations, the relative topological arrangement of cells within the circular micropatterns was studied. In Figure 5.15, the distribution of the relative cell positions with respect to a reference cell is shown for experiment and numerical modeling. It becomes evident that in systems containing two to four cells, all cells are predominantly located in topologically equivalent positions close to the outline of the circle pattern. For systems containing more than four cells, the average geometric arrangement of the cells within the pattern is changed to a conformation in which it is likely to find a cell at the system center. In fact, both types of arrangement can be identified within the plot of the five-cell systems of the numerical simulations, as highlighted in Figure 5.16.

As illustrated in Figure 5.17, a cell located in the system center is not able to direct its internal axis of polarization in such a way that it is aligned to the polarization axes of all of its neighbors simultaneously during a period of CAMo. Hence, a stable axis of polarization cannot be established by a cell located in the center of CAMo. This lack of orientation is likely to cause the drop off in $\tau_{\mathrm{CAMo}}(N)$ observed between $N = 4$ and $N = 5$. Applying this line of argument, rotational motion within the system is more persistent for more favorable alignments of polarization axes. In conformations in which the cells are able to migrate one after another in a head-to-tail fashion, an increased number of cells leads to an increase in CAMo persistence, since single cells which are not polarized in alignment with the majority can be counterbal-

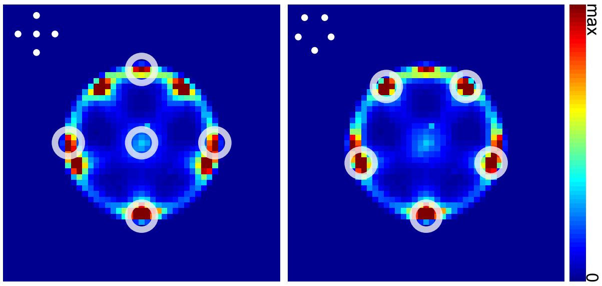

FIGURE 5.16.: Relative arrangement of five cells within a circular confinement for the simulation data. Heat map of the relative positions of five cells with respect to a reference cell position at the lower border of the system (see Section A.5.3 for details on the plot generation). As highlighted by the white circles, the observed maxima correspond to a mixture of two different geometric arrangements of cells within the system. A geometry featuring a four-fold rotational symmetry and a cell in the system center (left) and a five-fold rotational-symmetric geometry where all cells are located in topological equivalent positions in the outer regions of the circle (right). Figure adapted with permission from Reference [38]. Copyrighted by the American Physical Society.

anced by a greater number of favorably polarized cells. Such a trend is observed in experiment and simulations for systems containing two to four cells. A cell sitting in the system center however drastically decreases CAMo persistence as it disturbs the overall alignment of polarization axes, resulting in the drop-off in persistence between systems containing four and systems containing five cells. As cell number is increased further, the lack of orientation due to cells located in the center can be counterbalanced by the greater number of cells migrating in the outer parts of the circle, resulting in an increase of rotational persistence. Such a trend is observed in experiment for $N = 5 \ldots 8$. (In fact, the heatmaps of $N = 8$ indicate a contribution of arrangements in which two cells are located close to the system center, which might result in the slight drop in $\tau_{\mathrm{CAMo}}(N)$ between $N = 7$ and $N = 8$.) However, with higher cell numbers, the possible topological arrangements within the system increase (as e.g. indicated by the more "smeared out" maxima), which is likely to result in the fact that $\tau_{\mathrm{CAMo}}(N)$ shows no clear trend in the simulation runs for $N \geq 5$.

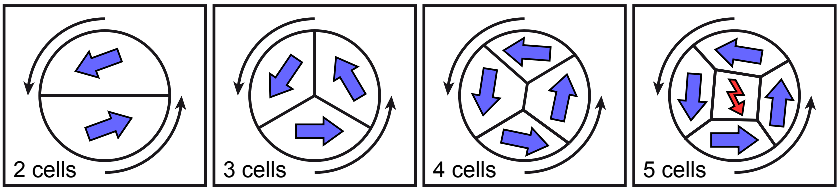

FIGURE 5.17.: Alignment of internal cell polarization axes during CAMo. Schematic of possible polarization alignments for systems containing two to five cells. For five cell systems in which a cell is located in the system center, the centered cell is not able to align its axis of polarization to the axes of its neighbors. Figure adapted with permission from Reference [38]. Copyrighted by the American Physical Society.

In order to check whether a correlation between polarization of a cell and its position along the radial direction of the system exists, we evaluated the mean magnitude of the front-rear polarization of the confined cells in the simulation runs. In Figure 5.18, the average cell polarization is plotted as a function of the radial position, r, of the corresponding cell with respect to the system center at $r = 0$. In general, the magnitude of polarization increases with r until it reaches a maximum near the outermost positions cells are located at. This maximum corresponds to the (half of) the typical cell width in the simulation. The only exception to this rule is observed for systems of three cells, which exhibit a high average polarization around $r = 0$. The data indicates, however, that for $N = 3$, conformations in which a cell is located near the system center are rather rare. Hence, the increased polarization of such cells is more likely to resemble the transient event of a single cell migrating through the system center than a stable cell conformation. Taken together, these findings support the suggestion that a cell located near the center of the pattern is unable to establish a stable axis of polarization and hence destabilizes collective behavior throughout the system.

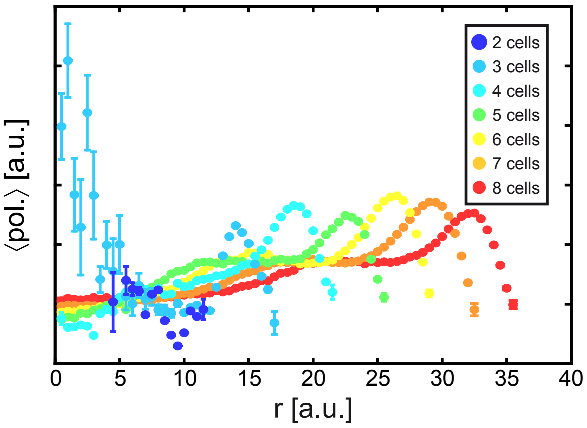

FIGURE 5.18.: Cell polarization as a function cell position. From the numerical simulations, the mean magnitude of polarization is evaluated and plotted against the radial cell position r. Error bars indicate the standard error of the mean. Figure adapted with permission from Reference [38]. Copyrighted by the American Physical Society.

The observations for the trend of $\tau_{\text{DisMo}}(N)$ with cell number are more difficult to interpret. On the one hand, this is because they are less obvious than the trends of $\tau_{\text{CAMo}}(N)$. On the other hand, the deadlocked conformation observed in the simulations make it difficult to compare theoretical with experimental results. In experiment, the values for $N = 2 \ldots 4$ might indicate that an odd number of cells polarizes faster into CAMo than an even number. Such an observation could be supported by the fact that “draw” conformations in which the polarization directions within a system are roughly balanced are less likely to occur for odd cell numbers (Figure 5.19). The polarization signal of a cell located in the system center might help to overcome such balanced situations, possibly explaining the drop-off in $\tau_{\text{DisMo}}(N)$ between four and five cell systems and the increasing trend for $N = 5 \ldots 8$. This trend might indicate that for systems composed of a larger amount of cells, it needs more time until the polarization axes of all cells are aligned in such a way that CAMo emerges (assuming similar arrangement of cells in the system). However, these thoughts are only suggestions. Simulations runs in which the parameters are adjusted such that the emergence of deadlocked configurations is at the least less likely might be used to obtain further insights into the dynamics of the disordered motion state in future studies.

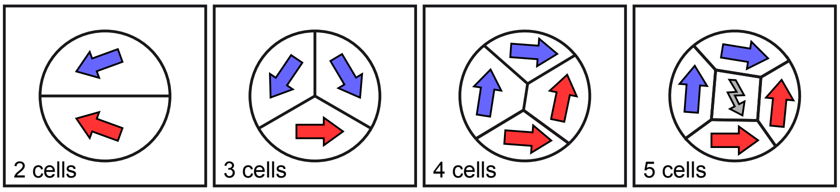

FIGURE 5.19.: Alignment of internal cell polarization axes during DisMo. Schematic of possible polarization arrangements for systems containing two to five cells. Systems consisting of an even number of cells can establish balanced polarization arrangements in which each cell receives opposing signals regarding the polarization direction from its neighbors. An additional cell located in the system center might help to overcome such balanced situations.

In conclusion, the results of this chapter show that the circular confinement of a micropattern can be exploited to study the emergence and persistence of collective cell rotation as a function of cell number. The experimental results are reproduced well by the numerical model accounting for intracellular polarization and intercellular coupling via mechanotransduction. Both experiment and simulation showed consistently that the persistence of collective rotation states increases with the number of confined cells for small cell numbers, but drops abruptly when the cellular conformation in the system changes to an arrangement featuring a centered cell. This finding illustrates the decisive role of the interplay between the local arrangement of neighboring cells and the cell-internal polarization in collective migration.

One might argue that the features of the motion patterns described in this chapter remind strongly of the results obtained from the analysis of single-cell tracks discussed in Chapter 4. In both cases bimodality exhibiting a directional persistent state and a state characterized by random (or disordered) motion is found. Furthermore the lifetimes of the individual states observed in both setups are distributed exponentially, showing typical persistence times on the same order of magnitude. It hence could be suggested that the bimodality in the motion of small cell assemblies directly emerges from the bimodality in the migration of the individual participating cells. The fact that both CAMo and DisMo states are also observed in the numerical simulations might, however, give a hint in this regard. In the applied model, no explicit bimodality for the cell internal polarization and migration dynamics is implemented. Therefore, a bimodal behavior is, at least, not directly to be expected for the migration of a single cell on a ring pattern. The fact that it, nonetheless, emerges in the simulated migration of multiple cells hence indicates that an intrinsic bimodality on single-cell level is not the key driver of the bimodality observed on the level of small cell assemblies.

CHAPTER 6

CONCLUSION AND OUTLOOK

In this thesis, micropattern techniques were developed and applied to study single-cell motion as well as the emergence of collective cell migration.

In Chapter 3, μPIPP, a novel technique for micropatterning, was introduced and discussed. Since the technique is rather easy to implement and does not require advanced and expensive equipment, it should enable a broad range of cell labs to profit from the advantages of micropattern-based experimental setups. The fact that μPIPP works on a variety of biocompatible substrates without an adjustment of any of the parameters of the protocol further increases its applicability. Additionally, the introduced variations of the protocol extend the set of achievable pattern designs and hence permit the realization of a broad range of highly specialized microenvironments. This way, surface-bound protein gradients become accessible, hence enabling the study of chemotactic aspects in cell behavior. Furthermore, as illustrated in Figure 6.1, the chemotaxis chamber used in the protocol provides the possibility to establish a second, solute gradient of guidance cues in the solution surrounding the cells. This way, multi-cue situations which combine the guidance cues provided by a surface-bound protein gradient, by a protein gradient in the surrounding solution, and by the individual micro-patten geometry can be combined. While, so far, there are many publications focusing on cell responses to the exposure to a single guidance cue[16,77–79,82–87], little is known about eventual synergy or competition effects between cellular guidance cues[205]. However, cells migrating *in vivo* are likely to be confronted to multi-cue situations. The lack of corresponding studies does hence not reflect the irrelevance of the topic but is at least partly due to the fact that multi-cue environments are difficult to implement *in vitro*. The method described in this thesis is a step towards making such elaborate setups more accessible and hence might provide a useful tool in this regard.

Moreover, the introduced protocols combining μPIPP with μCP enable the creation of patterns composed of multiple protein components. Such patterns provide the possibility to directly compare cell behavior on different protein coatings. In addition, the fact that the different coatings are placed readily adjacent to each other allows to study cell behavior at the interface between the coatings. While cell spreading and motion is usually characterized on different surface coatings individually[17,152,153], the possibilities to directly capture and study the be-

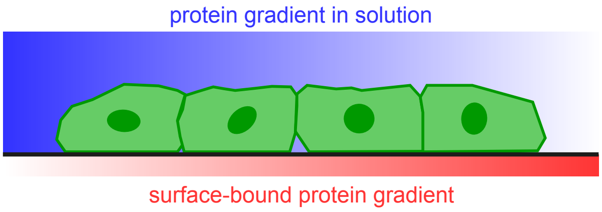

FIGURE 6.1.: Cells in an artificial multi-cue environment. The µPIPP protocol in combination with a chemotaxis chamber can be used to create a combination of surface bound and soluble protein gradients for cell guidance.

havior of a cell when encountering the interface between two different coatings might reveal further insights into the dynamic adaption of a cell to abrupt changes in the composition of the underlying substrate. Furthermore, sophisticated pattern designs including gradients and multiple protein components might help to more closely mimic the complex environments a cell encounters *in vivo* in future studies.

In Chapter 4, guiding microlanes were introduced as an assay to characterize and quantify single-cell migration. In these patterns, we found bimodality in form of changes between phases of directional persistent (run state) and phases of rather erratic (rest state) migration. The typical lifetimes of both states were measured using an algorithm detecting characteristic changes in cell motion. In combination with the cell velocity in the run state these lifetimes were used to characterize and quantify single-cell migration. The analysis scheme allowed to independently assess both the directional persistence and the actual migration velocity independently. This independent measure of both quantities is advantageous compared with conventional methods, in which the migration velocity is measured over the whole track of a cell and hence is biased by stops and changes in the direction of cell migration. The bimodal analysis yielded detailed insights into the effects of different pharmaceutics on cell migration and revealed that, in contrast to suggestions of other studies[13,42], migration speed and directional persistence do not necessarily correlate.

By integrating PEGylated barriers of different width into the setup, cell migration at chemical interfaces was studied, revealing an exponential decrease of the probability for a cell to overcome the obstacle with barrier width. The probability for a cell to reverse direction when encountering a barrier as well as the probability for a cell to reverse direction in the absence of a barrier were used as additional measures to characterize cell migration. Taken together, the analysis of cells in our setup hence yielded five parameters characterizing single-cell migration similar to a “migratory fingerprint”. The used assay thus is a step towards establishing a standardized tool to characterize, quantify, and compare the migration behavior of different cell types as well as the effect of different pharmaceutics or pathological conditions. Such systematic assessment of migration might finally result in databases serving as a reference in pharmacy and diagnostics.

Deeper insights into the intracellular processes affecting the phenomenological measures extracted in our analysis might be gained by comparing the experimental results to theoretical models. By simulating cell migration within ring-shaped patterns, the effect of specific model parameters on quantities such as the run/rest persistence or the run velocity could be studied. This way, the underlying mechanisms determining the migration behavior of different cell types might be revealed. In addition, the quantitative readout of cell migration provided by our setup should prove useful as a basis to parameterize and validate such theoretical models.

Obviously, the “migratory fingerprint” introduced in this thesis is extendable and the amount of included measures could easily be increased in future experiments. For instance, it could be investigated how barriers of other surface coatings than PEG affect the migration of a cell within the pattern. As components of the natural cell environment, ECM proteins might be interesting candidates in this regard. A possible way to accomplish the corresponding experimental setups is provided by the multi-component patterning approach developed in the course of this thesis. Of course, such studies would not only serve the characterization of migration but might also give new insights into the cell-ECM interaction and its relation to the migration process.

Another aspect which could be addressed in future experiments is how the geometrical shape of a barrier affects the repolarization process when a cell changes direction at the interface. In fact, several studies have shown that actin arrangement and the orientation of the polarization axis are strongly influenced by the confinement geometry[30,31,206]. Studying the effect of different barrier shapes on the speed of the repolarization process might complement these studies with insights into the dynamic aspect in the formation process of cellular polarization. A suitable pattern geometry addressing this issue is proposed in Figure 6.2(a).

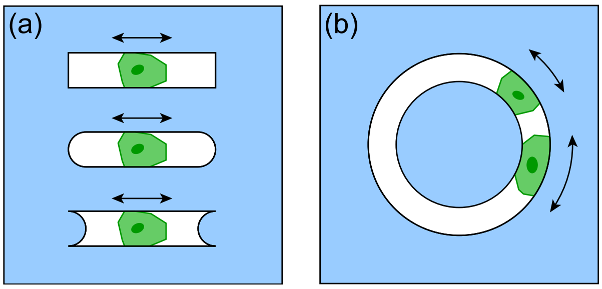

Figure 6.2.: Experimental setups suggested for future studies on single-cell migration. (a) Arrays of short linear lanes featuring different end designs to study cellular repolarization and cytoskeletal dynamics in dependence of the barrier shape. (b) Ring setup confining two cells to study cell-cell interaction.

Furthermore, the confinement provided by the ring pattern would be suitable to study the encounter and resulting interaction of one cell with another (Fig. 6.2(b)). Similar experiments performed on straight-lane patterns indicated that contact inhibition of locomotion (CIL) occurs not always but probabilistically at a cell-cell encounter[40]. Once two cells are confined, the closed geometry of the ring pattern would allow to measure multiple cell-cell encounters within one experiment. The resulting large sample sizes could hence be used to determine the probability of the occurrence of CIL for different cell types. In addition, the effect of cell-cell and cell-barrier encounters on the migration behavior of a cell could be compared. Using barriers composed of different membrane proteins (or protein motives mimicking these proteins), the key players causing CIL might be revealed. Taken together, the assay of ring shaped patterns and its extension by chemically modified barriers has proven useful to study single-cell migration and provides multiple possibilities for extensions and future experiments.

In Chapter 5, circular micropatterns are introduced to study the emergence and persistence of collective migration in form of coherent rotational motion as a function of the number of confined cells. Similar to the observations for single-cell migration, we find two distinct motion states in the system; one state featuring coherent angular motion (CAMo) of all confined cells while the other state is characterized by disordered motion (DisMo). The typical persistence time of the CAMo state increases with cell number but shows a pronounced drop between systems containing four and those containing and five cells. We compared the experimental results to numerical simulations based on a CPM and showed that the drop in persistence can be attributed to a change in the topological arrangement of the cells within the system. Taken together, we revealed the decisive role of the interplay between the local arrangement of neighboring cells and the internal cell polarization in collective migration.

It is still not clear if the bimodality in the motion of small cell assemblies directly emerges from the bimodality in the migration of the individual, participating cells. The fact that both CAMo and DisMo states are also observed in numerical simulations however shows that at least no cell-intrinsic bimodality is necessary for the emergence of bimodal migration behavior on the scale of cell assemblies. Further experiments using the same cell line for both experimental setups and comparing the corresponding persistence times might, nonetheless, help to clarify these points. Also, simulation runs of single cells migrating in circular lanes might be of interest in this regard.

Another aspect which would be interesting to address is the detailed polarization dynamics in the system during the emergence of CAMo. In our studies, we showed that the typical time until CAMo emerges depends on the number of cells in the system. But how exactly does the alignment of the polarization axes of all cells in the system develop? A possible course of events would be that the eventual polarization of a single cell causes the aligned polarization of its adjacent neighbors. Traveling through the system from cell to cell, this polarization cascade could finally lead to the overall polarization alignment in azimuthal required for the emergence of CAMo. Another possibility would be that all cells within the system spontaneously polarize in one direction or the other until, by chance, the polarization axes of the majority of the cells are aligned according to CAMo. Once this majority is reached, the remaining cells could be physically forced into the direction of motion. In order to shed light on this process, it would be useful to have a marker at hand which indicates the polarization axis of a cell, ideally doing so before the cell is starting to move correspondingly. Such a marker would allow to track the "polarization signal" through the system and hence illuminate the dynamics of intercellular coordination. One possible candidate for the visualization of cellular polarization would for example be to read out the axis from a cell's nucleus to its centrosome.[30,33,207,208] The information gained from the system would increase even further if, in addition, intercellular forces were recorded by one of the methods provided in other publications[64,209,210]. By comparing and measuring eventual delay times between the propagation of intercellular forces and the propagation of the polarization signal within the system, such experiments could shed light on the question to what extend intercellular signals regarding polarization are transmitted either mechanically or chemically. This kind of experiment would probably profit from an adjustment of the setup towards a ring-shaped geometry as shown in Figure 6.3(a). Since in course of this thesis, we found that cells positioned in the system center disturb CAMo within the patterns, rendering the system center cell-repellent might simplify the analysis. Furthermore, if the ring width (like in Chapter 4) is adjusted to the cell size, each cell ideally possesses two neighbors, and intercellular signaling can be tracked from one cell to the next along the lane.

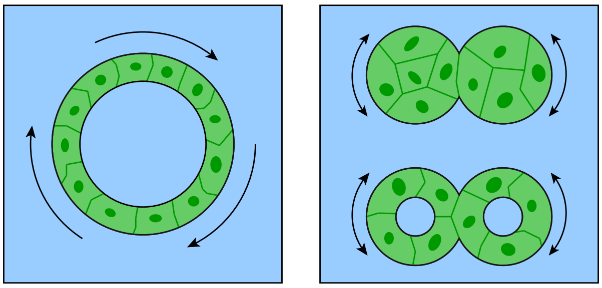

FIGURE 6.3.: Experimental setups suggested for future studies on collective migration. (a) Ring pattern confining a "chain" of cells to study the transmission of intercellular signals. (b) Connected circle or ring setup confining small cell assemblies to study the effect of "coupling" on collective cell rotation.

Another interesting modification of the setup would be to introduce a "coupling" between two rotating systems as illustrated in Figure 6.3(b). In such systems, it could be studied how the parallel or antiparallel alignment of the cells polarization axes at the overlapping region affects the persistence of CAMo states within each of the systems. By varying the length of the overlap, the "coupling strength" could be tuned and the resulting effect on CAMo emergence and persistence could be quantified. Also, the dynamic formation and breaking of cell-cell contacts could be systematically studied at the interface between both systems.

In conclusion, the results of this thesis shed new light on the process of single-cell migration and the interaction rules involved in the emergence of collective migration. Additionally, the introduced assays are a further step towards establishing micropatterning assays as a standard tool for cell science. In this regard, the development of µPIPP as a new patterning approach, which is easy to implement and versatile with regards to the achievable pattern designs, should increase the accessibility of patterning techniques in the field. All in all, the techniques and results described here hence contribute to the understanding of one of the fundamental processes in the development and maintenance of multicellular organisms.

APPENDIX A

METHODS AND EXPERIMENTAL DETAILS

A.1. PATTERNING PROTOCOLS*

A.1.1. PREPARATION OF STAMP MASTERS

A master of the desired pattern was prepared on silicone using photolithography. An adhesion promoter (TI-Prime, MicroChemicals GmbH) was applied to a silicon wafer (Si-Mat) by spin-coating, first at 500 rpm for 5 s and then accelerating to 5000 rpm for 30 s. The wafer was baked for 2 min at 120°C on a hot plate. Then, a 15 µm thick layer of negative photoresist (SU-8 100, micro resist technology GmbH) was applied by spin-coating first at 500 rpm for 5 s and then accelerating to 2000 rpm for 35 s. Next, the wafer was soft baked at 65°C for 2 min and then at 95°C for 5 min. In the following step, the wafer was exposed to UV light (wavelength peaks: 365 nm, 405 nm, 436 nm) which was passed through a photo mask (e.g. Zitzmann GmbH) of the desired pattern (alternatively, a laser lithography device can be used to write the desired pattern directly in the photoresist). A 5 min post-exposure baking step was performed at 95°C in order to selectively crosslink the UV-exposed portions of the resist. Afterwards, the wafer was placed in a developer bath (mr-Dev 600, micro resist technology GmbH) for approximately 2 min. To inhibit crack formation in the photoresist layer, the wafer was baked again for 5 min at 95°C. Finally, the surface was silanized with perfluorotrichlorosilane (Sigma Aldrich) by silane evaporation. Masters for stamp preparation can also be created by following established protocols such as those provided by photoresist producers like MicroChem. Once prepared, each master can be used to make multiple generations of stamps.

A.1.2. PREPARATION OF PDMS STAMPS

To create stamps, PDMS monomer and crosslinker (DC 184 elastomer kit, Biesterfeld Spezialchemie GmbH) were mixed in a 10:1 ratio, poured onto the stamp master, degassed in a des-

---

*This section is partly based on the publications Segerer *et al.* [135], Schreiber and Segerer *et al.* [36], and Schuster *et al.* [37].

iccator, and cured overnight at 50°C.

A.1.3. CONVENTIONAL μCP

A PDMS stamps of the desired pattern was activated in a UV-ozone cleaner (novascan) for 5 min. Afterwards, the stamp was incubated for about 1 h with a 50 μg/ml solution of the desired protein (40 μg/ml fibronectin (Yo proteins) and 10 μg/ml fibronectin labeled with Alexa-488 (Life Technologies) for the ring patterns used in Chapter 4). Next, stamps were washed with ultrapure water, dried and placed on a cell dish (Ibidi) which had been activated with UV light for 15 min. A droplet of a 1 mg/ml PLL(20 kDa)-g[3.5]-PEG(2 kDa) (PLL-PEG) solution dissolved in 10 mM HEPES containing 150 mM NaCl was placed at the edge of the stamps and drawn into the spaces between surface and stamp by capillary action. Stamps were removed and a glass coverslip was placed on the dish surface to ensure complete coverage of the surface with the PEG solution. After 30 min of incubation, the coverslip was removed and the sample was washed three times with phosphate-buffered saline (PBS) and stored in PBS until cells were seeded. (For experiments discussed in Chapter 4, an area of up to 1.5 cm^2 was patterned, resulting in up to 5000 ring patterns per dish.)

A.1.4. CONVENTIONAL μPIPP

A PDMS stamp of the desired pattern was placed on the surface to be patterned (see Figure 3.1). The assembly was then exposed to O_2 plasma at a pressure of 0.2 mbar in a plasma cleaner (Femto, diener electronics) at 40 W for 3 min, thus activating the exposed parts of the surface. A droplet of a 2 mg/ml PLL(20 kDa)-g[3.5]-PEG(2 kDa) (PLL-PEG) (SuSoS) solution in 10 mM HEPES (pH 7.4) and 150 mM NaCl was then placed at the edge of the stamp, and was drawn into the spaces between surface and stamp by capillary action. After 30 min at room temperature, the stamp was removed, and the substrate was rinsed with PBS. Finally, a (50 μg/ml) solution of the desired protein (e.g. fibronectin, fibrinogen) dissolved in PBS was added for 30-60 min (if not noted otherwise) and the substrate was rinsed three times with PBS.

A.1.5. GRADIENT PATTERNING

To set up a protein density gradient in the final pattern, the μPIPP protocol was applied to a chemotaxis slide. Therefore, the bottom surface of a chemotaxis slide (ibidi, sticky-Slide Chemotaxis3D) was first patterned with PLL-PEG according to the standard μPIPP protocol (steps 1 and 2 in Fig. 3.1(a)). Afterwards, the upper part of the “sticky chamber” was attached and filled with PBS. The PBS on one side of each chamber was then replaced by 45 μl of a 100 μg/ml solution of protein in PBS according to the manufacturer’s instructions[150] to create a gradient in the concentration of the protein solution. The patterned surface was incubated in this gradient for 40 min. Finally, the surface was rinsed by flooding the chamber three times with PBS.

A.1.6. MULTI-COMPONENT PATTERNING

APPLYING μPIPP AND μCP SIMULTANEOUSLY

To obtain a pattern consisting of three different components, the basic μPIPP protocol was extended as illustrated in Figure 3.8. This way of combining both techniques works for all stamp geometries that provide enclosed cavities. Initially, the PDMS stamp was activated for 5 min in an UV-ozone cleaner (novascan) and incubated for about 1 h with a 50 μg/ml solution of the first protein. Incubated stamps were rinsed once with ultrapure water and dried for about 6 min. Afterwards, a COC substrate (ibidi) was activated for 3 min in the UV-ozone cleaner before setting the stamp in place.[1] The subsequent procedure followed the standard μPIPP protocol. If a third protein instead of PLL-PEG was used, the plasma treatment was omitted.

APPLYING μPIPP AND μCP SUCCESSIVELY

In order to extend the set of achievable multi-component pattern designs, μPIPP was also combined to μCP in a successive manner. In doing so, the pattern created via μCP was partially removed by the plasma used for μPIPP (see Figure 3.10 for illustration). Analogously to the aforementioned protocol to create multi-component patterns, a PDMS stamp (in this case a stripe pattern) was activated for 5 min in an UV-ozone cleaner (novascan) and incubated for about 1 h in a 50 μg/ml solution of the first protein. The incubated stamp was rinsed with ultrapure water and dried for about 6 min. Afterwards, a COC substrate (ibidi) was activated for 3 min in the UV-ozone cleaner before setting the stamp in place. In order to ensure the transfer of protein from the stamp to the surface, a droplet of PBS was applied to the margins of the stamp were it was drawn underneath by capillary action. The sample was kept in PBS for 1 h. Afterwards, the stamp was removed and the surface dried in the airflow of the cell bench. Another stamp (in this case of the same stripe pattern as used for printing) was placed on the surface such that the stripes of the new stamp were orthogonal to the stripes created via μCP. The subsequent procedure followed the standard μPIPP protocol.

---

[1] This UV activation step was found to be critical, since the surface has to be sufficiently hydrophilic to allow the printed protein to be properly transferred from the stamp yet hydrophobic enough to ensure that the protein is adsorbed from the incubation solution.

A.2. CELL CULTURE

If not noted otherwise, cells were grown in supplemented medium in a humidified atmosphere, at 37°C with 5 % CO_2 level. Cells were maintained at about 80 % confluence and trypsinized for passaging as well as prior to experiments. The used cell lines as well as the corresponding culture media and supplements are given in Table A.1. For time-lapse experiments, about 10,000 cells were seeded in one dish (μ-dish, ibidi). In order to fluorescently label the nuclei, the cell medium was replaced about 2 h after cell seeding by 1 ml L15 medium (c.c.pro) containing 25 nM Hoechst 33342 dye (Invitrogen).

TABLE A.1.: Cell lines and their corresponding media used in this thesis.

cell type	organism	tissue	medium & supplements
HuH7	human	liver	RPMI, 2 mM L-Glu, 10 % FCS
HUVEC	human	umbilical vein	ECGM, 1 % PSA, 10 % FCS
MDA-MB-436	human	mammary gland	DMEM-F12, 2.5 mM L-Glu, 10 % FCS
MDCK	canine	kidney	MEM, 4 mM L-Glu, 10 % FCS

A.2.1. INHIBITOR TREATMENT OF HUVECS

In Section 4.4, the effects of different pharmaceutics on HUVEC migration were tested. Therefore, cells were treated about 2 h after seeding on the corresponding setups using 10 μM blebbistatin (Sigma), 250 pM calyculin A (Tocris Bioscience), or 10 μM Y-27632 (Sigma), respectively. Controls did not contain more than 0.5 % DMSO. One hour after treatment, live cell imaging was started.

A.2.2. PREPARATION OF CELLS FOR SCANNING ELECTRON MICROSCOPY

For the images shown in Figure 3.3, cells and substrate were pretreated as follows. Cells adhered to a micropatterned glass slides were washed in PBS and subsequently incubated for 30 min in a solution containing 0.5 % glutaraldehyde in 75 mM cacodylate buffer (pH 7) for fixation. Afterwards, the sample was once washed in cacodylate buffer and five times in distilled water for 10 min each. Now, the sample was dehydrated by exchanging the water by ethanol in a stepwise manner. In order to achieve a conducting surface, the specimen was sputter-coated with layer of a gold-palladium mixture before microscopy.

A.3. MICROSCOPY

A.3.1. PHASE-CONTRAST AND FLUORESCENCE MICROSCOPY

Phase-contrast and fluorescence images were taken on a TI Eclipse (Nikon) or an iMIC (Till Photonics) inverted microscope, respectively. Confocal microscopy was performed using a SP8 microscope (Leica).

A.3.2. TIME-LAPSE MICROSCOPY

Scanning time-lapse measurements were performed using an automated inverted microscope (iMIC, Till Photonics). The microscope was equipped with a 10x Zeiss phase-contrast objective, a Oligochrome lamp (Till Photonics) and an ORCA-03G camera (HAMAMATSU). A temperature-controlled mounting frame (ibidi temperature controller, ibidi) was used to maintain cells at 37°C during the measurements. If not noted otherwise, phase-contrast and fluorescent images were acquired in intervals of $\Delta t = 10\,\mathrm{min}$ length. To analyze the membrane protrusions at the interface of the micropatterns as described in Section 4.2, a 40x objective was used and bright-field images were acquired within intervals of $\Delta t = 5\,\mathrm{sec}$ length.

A.3.3. SCANNING ELECTRON MICROSCOPY

The scanning-electron-microscopy images of Figure 3.3 were taken on a LEO Gemini DSM 982 (Zeiss) microscope.

A.4. EVALUATION AND ANALYSIS OF SINGLE-CELL TRACKS*

A.4.1. SINGLE-CELL TRACKING

For image data processing and cell tracking the image-processing software ImageJ[211] was used. Fluorescence images of the cell nuclei were preprocessed by first applying a bandpass frequency filter and subsequently transforming the data into binary images by using a threshold for the fluorescence intensity. Afterwards, the geometric center of mass of each nucleus was evaluated. For cells migrating within micropatterns, cell tracking was stopped at the occurrence of cell division or when cells migrated out of the pattern. For cells migrating in ring-shaped patterns, cell tracks shorter than 18 h, as well as tracks of dead or non-moving cells were excluded from further analysis. For the evaluation of cell tracks in the course of the motility analysis on different surface coatings described in Section 3.5, the Cell Evaluator software[212] was used.

A.4.2. BIMODAL CLASSIFICATION SCHEME

In order to dissect run and rest periods in the migration of individual cells on line and ring patterns, an classification scheme based on cumulative sum (CUSUM) statistics in combination with a motion analysis via fitting the MSD was implemented. The classification scheme is illustrated for a typical cell track in Figure A.1. In the first step, the CUSUM of the angular velocity, $\omega(t)$,[1] measured via the displacement of the cell nucleus between two adjacent frames of the time lapse measurement, was calculated as:

$$C(t) = \sum_{i=0}^{t} \left[\omega(i) - \bar{\omega}\right]. \tag{A.1}$$

Here, $\bar{\omega}$ denotes the average angular velocity within the period of observation, $t = 0, \ldots, T$. In order to estimate the likelihood that a change in the trend of $\omega(t)$ occurred within the given time interval, a confidence level for the existence of a change point (CP) was evaluated via a bootstrap analysis. To this end, an estimator for the magnitude of the change was defined as:

$$C_{\text{diff}} = (\max_{t=0,\ldots,T} C(t)) - (\min_{t=0,\ldots,T} C(t)). \tag{A.2}$$

This estimator was evaluated for the CUSUM of the actually measured angular velocity order as well as for a set of bootstrapped CUSUMs for which the consecutive order of $\omega(t) : t \in$

---

*This section partly based on the publication by Schreiber and Segerer *et al.*[36].

[1] For the straight-lane patterns used in Section 4.4, the cell velocity, $v(t)$, rather than the angular cell velocity, $\omega(t)$, was used for the calculation of $C(t)$.

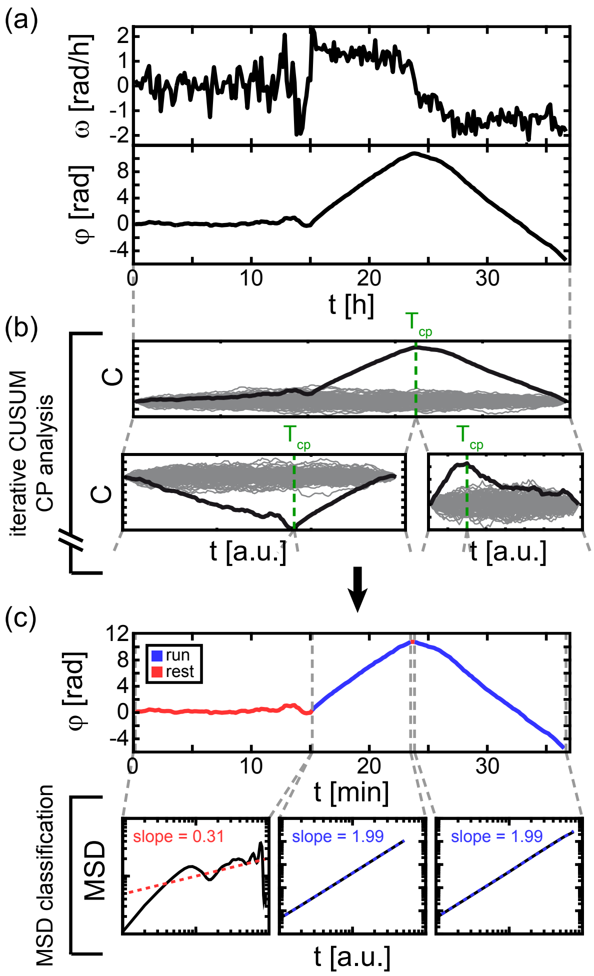

FIGURE A.1.: Bimodal analysis of quasi-one-dimensional cell tracks. (a) Time evolution of the angular velocity, $\omega(t)$, and the azimuthal position, $\varphi(t)$, (with respect to the initial position, $\varphi(0) = 0$) of an exemplary track of a cell migrating in a ring-shaped micropattern. (b) CUSUM function, $C(t)$, (black) and bootstrapped CUSUM functions (gray). The estimated time point, T_{CP}, at which the CP occurred is indicated by the green dashed line. The procedure is repeated iteratively for the resulting intervals. (c) Classification of cell motion within via evaluating and fitting the corresponding MSD within the intervals. The MSDs (black) of the intervals indicated in the upper graph are plotted in log-log representation and fitted by a function, $f(t) = a \cdot t^b$ (blue/red dashed lines). The slope of the fit, b, indicates if the motion within the interval is classified as rest state ($b < b_{\mathrm{th}}$) or run state ($b \geq b_{\mathrm{th}}$).

$\{0, \cdots, T\}$ was permuted randomly (Fig. A.1(b)). The confidence level for the occurrence of at least one CP within the analyzed time interval was now calculated as:

$$L_{\mathrm{conf}} = \frac{N_{(C_{\mathrm{diff}} < C^0_{\mathrm{diff}})}}{N_{\mathrm{perm}}}. \tag{A.3}$$

Here, $N_{(C_{\mathrm{diff}} < C^0_{\mathrm{diff}})}$ denotes the number of bootstrap CUSUMs for which the estimator C_{diff} is smaller than the estimator C^0_{diff} of the original CUSUM and N_{perm} denotes the overall number of bootstrap samples used. Throughout this work the number of permuted samples was chosen to be $N_{\mathrm{perm}} = 10000$. Now, a threshold level, L_{th}, was chosen such that for $L_{\mathrm{conf}} > L_{\mathrm{th}}$ the position of a CP was evaluated while for $L_{\mathrm{conf}} \leq L_{\mathrm{th}}$ the interval was considered as to exhibit now CP. As a trade-off between sensitivity and liability to small fluctuations, the threshold level was chosen as $L_{\mathrm{th}} = 0.7$ in this work. For $L_{\mathrm{conf}} > L_{\mathrm{th}}$, the position of a CP was evaluated via the CUSUM estimator:

$$T_{\mathrm{CP}} = \left\{ t \,\middle|\, C(t) = \max_{t=0,\ldots,T} |C(t)| \right\}. \tag{A.4}$$

Afterwards, the whole procedure was iteratively repeated for the two resulting intervals adjacent to the found CP until no further CPs with confidence $L_{\mathrm{conf}} > L_{\mathrm{th}}$ were detected.

In order to identify the cell motion within the intervals between adjacent CPs as run or rest periods, the time averaged MSD was calculated for each interval as:

$$\mathrm{MSD}(t) = \frac{1}{T - t + 1} \cdot \sum_{\tau=0}^{T-t} \left[\varphi(\tau + t) - \varphi(\tau)\right]^2. \tag{A.5}$$

Here, $\varphi(t)$ indicates the azimuthal position of the cell with respect to the initial cell position, $\varphi(0) = 0$, at the start of the corresponding interval. The MSD was now fitted by a function, $f(t) = a \cdot t^b$, in which a and b indicate fitting parameters. In this type of motion analysis, the exponent b indicates whether a motion pattern has to be considered as normal ($b = 1$) or anomalous ($b \neq 1$) diffusion. A value of $b = 2$ would correspond to ballistic motion. In order to identify periods in which the cells show directionally persistent (ballistic) motion (along the circular lane), a threshold was chosen at $b_{\mathrm{th}} = 1.75$ such that all intervals in which $b < b_{\mathrm{th}}$ were classified as rest state periods whereas all intervals in which $b \geq b_{\mathrm{th}}$ were classified as run state periods. The fits in log-log presentation and the resulting classification for the example track shown in Figure A.1(a) are depicted in Figure A.1(c). The distribution of the fitting parameter, b, evaluated for all analyzed intervals between adjacent CPs is shown in Figure A.2.The threshold value of $b_{\mathrm{th}} = 1.75$ was chosen such as to include the peak corresponding to directionally persistent motion. It is important to mention, that for very short time intervals ($T < 60\,\mathrm{min}$) for which only a very limited set of data points is accessible, a fit of the MSD is not a very robust measure. Hence, for these short intervals the criterion for a period to be classified as a run state period was chosen such that $\omega(t)$ had to be strictly increasing or decreasing within the borders of the interval. Consequently, if this criterion was not met, the corresponding interval was classified as rest state period.

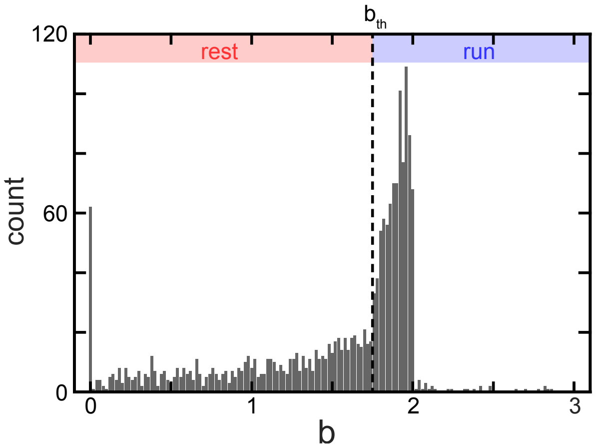

FIGURE A.2.: Dissection into run and rest states. Distribution of the MSD-fitting parameter, b, for all intervals found within the tracks of MDA-MB-436 cells migrating on ring shaped micropatterns. The value for the threshold, $b_{\mathrm{th}} = 1.75$, dissecting run states from rest states is indicated by the black dashed line.

Finally, all CPs separating two adjacent rest state periods or two adjacent run state periods in which the cell moved in the same direction were removed. The analysis was automated using an algorithm implemented in MATLAB[213].

A.4.3. EVALUATION OF PHENOMENOLOCICAL MEASURES CHARACTERIZING SINGLE-CELL MIGRATION

In Chapter 4, various phenomenological measures were introduced to characterize and quantify single-cell motion as well as the interaction of cells with chemical interfaces. In the following, the detailed calculations of the persistence times, τ_{run} and τ_{rest}, as well as of the turning probability, $P_{\mathrm{turn}}(d_{\mathrm{gap}})$, are described.

The persistence times, τ_{run} and τ_{rest}, are calculated by fitting the logarithm of the survival function, $\log\left[S(t)\right]$, of the corresponding state by a linear function, $f(t) = \frac{-t}{\tau} + c$. For MDA-MB-436 cells, the trend of $S(t)$ differs for short and long timescales as can be seen in Figure 4.3(c). Consequently, the linear fit of $\log\left[S(t)\right]$ was solely performed in regions where $S(t)$ exhibited exponential behavior ($t > 5\,\mathrm{h}$ for the run state and $t > 2.5\,\mathrm{h}$ for the rest state). Furthermore, for the calculation of $S(t)$, only run and rest states starting at least 20 h (8 h for HUVECs) before the end of the corresponding cell track were evaluated while the times $t > 20\,\mathrm{h}$ ($t > 8\,\mathrm{h}$ for HUVECs) were not included in the fit. This way it was ensured that the limited observation time of the experiment did not affect the resulting values of τ_{run} and τ_{rest}. (All states of a duration $T < 20\,\mathrm{h}$ appearing within the period of observation do contribute to the analysis, while states of a duration $T \geq 20\,\mathrm{h}$ which possibly exceed the time of observation do not affect the trend of $S(t)$ within the range of fitting.) The error for τ_{run} and τ_{rest} indicates a 99 % confidence interval in the fit of $S(t)$.

The turning probability, $P_{\text{turn}}(d_{\text{gap}})$, was evaluated by counting how often cells reverse their direction of motion within a region of 50 µm before the corresponding barrier edge. $P_{\text{turn}}(d_{\text{gap}})$ thus corresponds to the fraction of times the cell leaves this region to the same side (away from the barrier) as it entered. In the case of $P_{\text{turn}}(0)$, this fraction was evaluated averaged over eight arbitrarily chosen 50 − µm regions along a ring pattern without a barrier. The error range of $P_{\text{turn}}(d_{\text{gap}})$ was calculated as the Clopper-Pearson 95 %-confidence interval for binomial distributions. For barrier widths of 3, 8, 13, and 19 µm, a number of 158, 265, 209 and 296 barrier encounters of MDA-MB-436 cells were evaluated, respectively. For HuH7 cells and salinomycin-treated MDA-MB-436 cells, 101 and 303 encounters with a barrier of 8 µm width were evaluated, respectively. The analysis was automated using an algorithm implemented in MATLAB[213].

A.5. EVALUATION AND ANALYSIS OF COLLECTIVE ROTATION *

A.5.1. MULTI-CELL TRACKING

In order to track the positions of the individual nuclei within the circular systems described in Chapter 5, a tracking algorithm was developed and implemented within the framework of a bachelor thesis.[214] In brief, the fluorescence images were first processed to evaluate the position of each nucleus within an image using the image-processing software ImageJ[211]. Therefore, the microscopy images were first converted to binary images by applying a threshold for the fluorescence intensity. Afterwards, the built in "fill holes" and "watershed" algorithms were applied to eliminate dark regions within the nucleus in underexposed images as well as separate seemingly merged nuclei in overexposed images, respectively. Subsequently, the geometric center of mass was evaluated for each nucleus. Finally, the assignment of cell identities from one frame to the next was accomplished by an optimization algorithm implemented in the C++ programming language[215]. Cell tracking and analysis was stopped at the occurrence of cell division or cell death, or when cells migrated out of the pattern.

A.5.2. EVALUATION OF COLLECTIVE ROTATION

In Sections 5.1 and 5.2, the evaluation of the angular positions, $\varphi_i(t)$ for $i \in \{1, \ldots, N\}$, and the total angular velocity, $\Omega_N(t)$, for all N cells within a circular micropattern was described briefly. The detailed calculations involved in this process are shown in the following.

In the first step, the center of a system was defined as the time averaged geometric center of mass of the individual cell positions, $\vec{r}_i(t)$, within a system according to:

$$\vec{r}_{\mathrm{CM}} = \langle \langle \vec{r}_i(t) \rangle_T \rangle_N . \tag{A.6}$$

Here, $\langle \ldots \rangle_T$ indicates the mean over the full time, T, the system is analyzed and $\langle \ldots \rangle_N$ indicates the mean over all cells , c_i where $i \in \{1, \ldots, N\}$, within a system. Using polar coordinates with respect to $\vec{r}_{\mathrm{CM}}$, the angular position of each cell was evaluated from its azimuthal displacements, $\Delta\varphi_i(t) = \omega_i(t) \cdot \Delta t$, between two successive frames,

$$\varphi_i(t) = \sum_{\tau=0}^{t} \Delta\varphi_i(\tau), \tag{A.7}$$

where $t = 0$ indicates point in time from which on the system was analyzed (e.g. the start of the time-lapse measurement or a cell-division event) and Δt indicates the time interval

---

*This section is to a large part based on the publication Segerer *et al.*[38].

between two successive frames of the time-lapse measurement (e.g. $\Delta t = 10\,\mathrm{min}$). As indicated in Figure 5.3, the movement of a cell, c_i, (more precisely of the geometric center off its nucleus) in the close vicinity of $\vec{r}_{\mathrm{CM}}$ can lead to comparatively large values of $\Delta\varphi_i(t)$ (and $\omega_i(t)$). Such increased values of $\Delta\varphi$ for individual cells can possibly compromise the system angular velocity, $\Omega_N(t)$, in its role as a measure for the overall angular velocity in a system. Hence, at each time, t, the cell closest to $\vec{r}_{\mathrm{CM}}$ was excluded when calculating $\Omega_N(t)$ according to Equation 5.1.

A.5.3. CALCULATION OF RELATIVE CELL POSITIONS

In Section 5.6 heat maps of the relative positions of cells within circular micropatterns were shown and discussed. In the following, the generation of these graphs is explained in more detail.

For each frame of the time-lapse measurement of systems of the same cell number, N, all cell positions were rotated by an angle, α, around the system center $\vec{r}_{\mathrm{CM}}$. Thereby the angle, α, was chosen such that the azimuth of the cell with the second largest radial coordinate became zero[1] (corresponding to a position exactly below $\vec{r}_{\mathrm{CM}}$). Afterwards, by applying an iterative closest point (ICP) algorithm, the cell positions of the successive frame were commonly rotated around $\vec{r}_{\mathrm{CM}}$ as to best match these positions. These rotated positions were now used for the location statistics and consequently for the final heat map. This procedure was conducted for every frame of each system using an in-house algorithm implemented in MATLAB[213].

A.5.4. ALTERNATIVE DISMO-CAMO CLASSIFICATION SCHEME

The classification to dissect periods of CAMo from periods of DisMo as it is described in Section 5.2 is a heuristic approach and as such may results in artifacts in form of wrongly associated motion behavior. Hence, in order to crosscheck and validate the results discussed in Chapter 5, an alternative approach to discriminate collective behavior from disordered motion was implemented. This alternative approach, which was adapted from an approach to quantify collectivity in locust swarms[216], is described in the following.

For each cell, c_i, where $i \in \{1, \dots, N\}$ a cell orientation angle, γ_i, was defined as:

$$\gamma_i(t) = -\arcsin\left(|\hat{v}_i(t) \times \hat{r}_i(t)|\right). \tag{A.8}$$

Here, $\hat{v}_i$ denotes the unit vector in direction of the cell velocity, $\vec{v}_i$, defined as the displacement of a cell from the current frame to the succeeding one and $\hat{r}_i$ denotes the unit vector in direction of the cell position $\vec{r}_i$ within the actual frame with regards to the system center, $\vec{r}_{\mathrm{CM}}$. As

---

[1] The choice of the cell for the definition of α is arbitrary, using another cell as reference had no qualitative influence on the result.

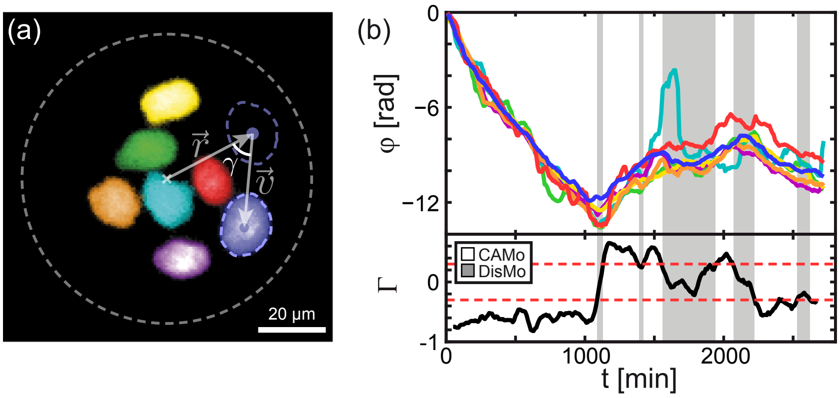

FIGURE A.3.: Alternative dissection of CAMo and DisMo periods. (a) False-color fluorescence image of the nuclei of seven cells within a circular micropattern. For each cell, the orientation angle, γ, is calculated from the velocity vector, $\vec{v}$, and the position vector, $\vec{r}$. (b) Angular positions, $\varphi_i(t)$, of each cell (in colors corresponding to the colors of the nuclei in (a)) and the average orientation, Γ, calculated according to Equation A.9. The threshold, $\Gamma_c = \pm 0.3$, dissecting CAMo from DisMo is indicated by the red dashed lines. Periods classified as DisMo are highlighted in gray. Figure adapted with permission from Reference [38]. Copyrighted by the American Physical Society.

illustrated in Figure A.3(a), $\gamma(t)$ hence denotes the smaller angle between the motion direction of a cell and a line drawn from its current position to the system center. For cell motion in clockwise direction γ gives negative values while it gives positive values for motion in counterclockwise direction.

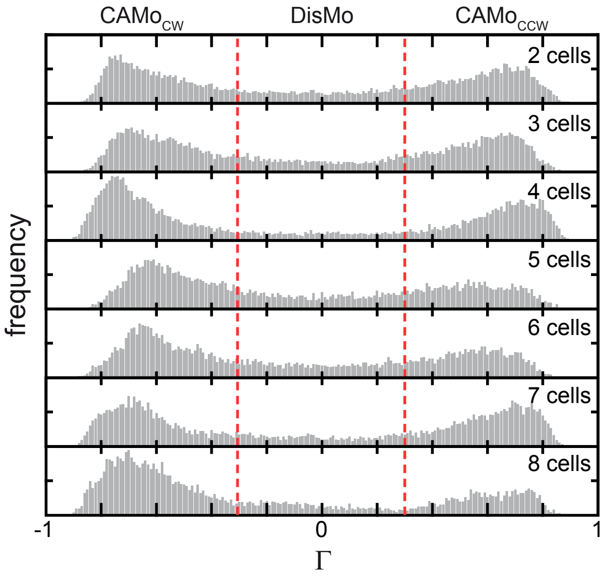

FIGURE A.4.: Distribution of the average orientation, $\Gamma_N(t)$, for systems containing two to eight cells. The threshold, $\Gamma_c = \pm 0.3$, dissecting CAMo from DisMo is indicated by the red dashed lines. Figure adapted with permission from Reference [38]. Copyrighted by the American Physical Society.

In the next step, the overall alignment of cell orientation was quantified as:

$$\Gamma_N(t) = \frac{2}{\pi \cdot N} \sum_{i=1}^{N} \gamma_i(t), \tag{A.9}$$

where N denotes the number of cells within the system. Hence, a value of $\Gamma_N(t) = 1$ would correspond to a perfect circular alignment of the cell motion in ccw direction whereas $\Gamma(t) = -1$ would correspond to a perfect alignment in cw direction. A value of $\Gamma(t) = 0$ would correspond to no alignment in azimuthal direction or no cell motion at all. For all analyzed cell numbers, $N = 2 \dots 8$, the distribution $P(\Gamma_N)$ showed bimodal character exhibiting maxima corresponding to clockwise and counterclockwise rotation as it can be seen in Figure A.3(c).

In order to dissect collective from uncorrelated motion, a threshold of $\Gamma_c = \pm 0.3$ was defined such that for $|\Gamma_N(t)| < |\Gamma_c|$ the motion in the system was classified as DisMo while for $|\Gamma_N(t)| \geq |\Gamma_c|$ it was classified as CAMo, respectively. Note that the value of $\Gamma_c = \pm 0.3$ was heuristically chosen from the distribution $P(\Gamma)$ and the time evolution of the MSD of the resulting intervals of CAMo and DisMo. An alternative choice of $\Gamma_c = \pm 0.2$ and $\Gamma_c = \pm 0.4$, respectively, had only little influence on the results though and did not alter the fundamental trends in the persistence times of the motion states (data not shown). In order to filter out noise in form of high frequency fluctuations of $\Gamma_N(t)$, a rolling average over an interval of 9 data points (corresponding to 90 min) was applied to $\Gamma_N(t)$. The analysis was automated using an algorithm implemented in MATLAB[213].

A typical time course of $\Gamma_N(t)$ for the example system shown in Figure 5.3 is shown in Figure A.3(b). As can be seen, the classification via Γ_N resulted in very similar intervals of CAMo and DisMo as the classification via ξ_N as described in Section 5.2.

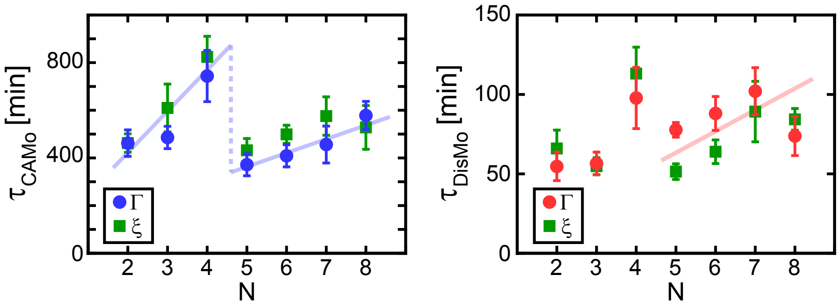

FIGURE A.5.: Average lifetime of CAMo/DisMo states for the alternative motion-classification scheme. Mean persistence times, τ, as a function of the cell number, N, for states of CAMo and DisMo. Values are derived from the exponential fits of the survival functions obtained via the average orientation, $\Gamma_N(t)$, (blue/red) and via the normalized total angular velocity, $\xi_N(t)$, (green). Error bars indicate confidence bounds of 99 % within the fits. Thick lines serve to highlight trends. Figure adapted with permission from Reference [38]. Copyrighted by the American Physical Society.

In agreement with the lifetimes of the motion states obtained via the normalized total angular velocity, ξ_N, the survival frequencies obtained via the average orientation, Γ_N, exhibit an exponential distribution (data not shown). As shown in Figure A.5 also the average survival times, τ_{CAMo} and τ_{DisMo}, show the same characteristics for both classification schemes.

Note that the classification via a threshold in the average orientation, Γ_N, is not less heuristic than the scheme described in the main text. Unlike the approach via ξ_N, the approach via Γ_N does, however, not depend on the magnitude of velocity of the individual cells, but only on its orientation. Both methods hence resemble clearly distinct approaches. The fact that both result in the same trends for $\tau_{\mathrm{CAMo}}(N)$ (also for alternative values for the corresponding thresholds, ξ_c and Γ_c) strongly indicates that the these trends are inherent in the system and do not resemble artifacts resulting from the data evaluation.

A.6. Implementation of the Cellular Potts Model[*]

In Chapter 5 the experimental results were discussed in comparison to the data obtained by an agent based numerical model developed and implemented by Thüroff *et al.*[203,204]. In order to fully grasp the implications of the simulation results and their comparison to the experiments, an understanding of the basic assumptions and rules of the CPM is needed. Hence, the basic principles of the modeling approach are outlined briefly in this section. For a more detailed description of the model and its discussion in the context of more general phenomena in cell migration see Reference [203].

The model is a generalization of the CPM shortly introduced in Section 2.4.2. Hence, each cell is defined as a set of connected lattice sites ("domains"), $\mathcal{D}^{(\alpha)} = \left\{\vec{x}_k \,\middle|\, c(\vec{x}_k) = \alpha\right\}$, where the function $c(\vec{x}_k)$ gives the index of the cell occupying grid site $\vec{x}_k$. At each time, each grid site can only be occupied by one cell at the most. The dynamics of the system are implemented by a succession of retraction and protrusion events diminishing or increasing the grid sites assigned to a particular cell. In more detail, these "elementary events",$\mathcal{T}$, for an exemplary cell, α, are implemented as follows:

In a protrusion event, cell α incorporates one of the directly adjacent grid sites, $\vec{x}_t \in \mathcal{N}^{(\alpha)}$, ("target grid site") such that: $\mathcal{D}^{(\alpha)}_{\text{old}} \rightarrow \mathcal{D}^{(\alpha)}_{\text{new}} = \mathcal{D}^{(\alpha)}_{\text{old}} \cup \{\vec{x}_t\}$. In a retraction event, cell α expels one the grid sites at its border, $\vec{x}_s \in \mathcal{B}^{(\alpha)}$, ("source grid site") such that: $\mathcal{D}^{(\alpha)}_{\text{old}} \rightarrow \mathcal{D}^{(\alpha)}_{\text{new}} = \mathcal{D}^{(\alpha)}_{\text{old}} \setminus \{\vec{x}_s\}$. The corresponding grid-site sets and processes are illustrated in Figure A.6.

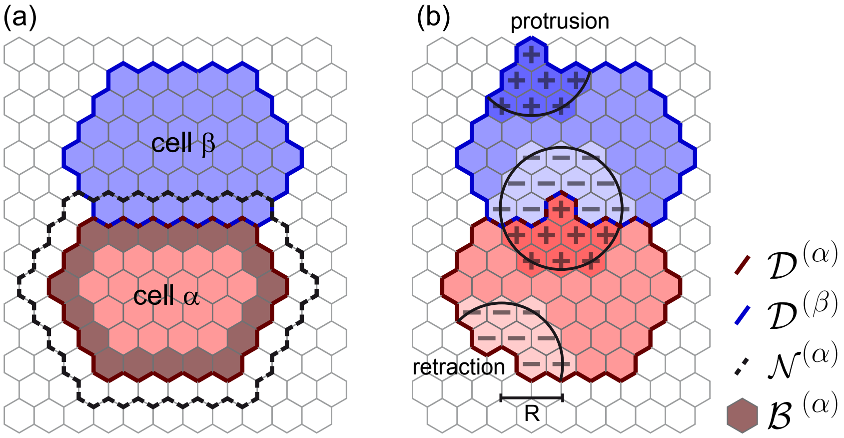

FIGURE A.6.: Mechanism of the CPM as used in this thesis. (a) Illustration of the grid-site sets defined in the model. Colored grid sites are occupied by cell α (red) and cell β (blue), respectively. For cell α, the membrane sites, $\mathcal{B}^{(\alpha)}$, available for retraction events are indicated by grayish red color. Grid sites, $\mathcal{N}^{(\alpha)}$, available for a protrusions of cell α are indicated by the dashed black line. (b) Elementary events of protrusion and retraction. Within a range, R, of a successful elementary event of protrusion or retraction the regulatory factors, $F(\vec{x}_n)$, are incremented ($+$) or decremented ($-$) for each grid site, respectively. Figure adapted with permission from Reference [38]. Copyrighted by the American Physical Society.

---

[*] This section is to a large part based on the publication Segerer and Thüroff *et al.*[38].

The simulation is performed in a Monte-Carlo procedure in which individual MCSs serve as the temporal unit. Within each MCS a number, K, of elementary event trials for randomly chosen membrane grid sites (e.g. $\mathcal{B}^{(\alpha)}$ for cell α) for randomly chosen cells is performed. The number of performed trials K was chosen as the overall number of membrane grid sites in the system. The probability, $p(\mathcal{T})$, for such elementary events, $\mathcal{T}$, to be successful is determined by a "Hamiltonian":

$$\mathcal{H} = \mathcal{H}_{\text{cont}} + \mathcal{H}_{\text{adh}} + \mathcal{H}_{\text{cyto}}. \tag{A.10}$$

Here, $\mathcal{H}_{\text{cont}}$ accounts for the effect of cell contractility, $\mathcal{H}_{\text{adh}}$ accounts for the effect of cell-cell adhesion, and $\mathcal{H}_{\text{cyto}}$ accounts for the effect of polymerization and depolymerization of the cytoskeleton. The acceptance probability of elementary events is hence calculated as:

$$p(\mathcal{T}) = \min\{1,\ \exp[-\Delta\mathcal{H}_{\text{cont}}(\mathcal{T}) - \Delta\mathcal{H}_{\text{adh}}(\mathcal{T}) - \Delta\mathcal{H}_{\text{cyto}}(\mathcal{T})]\}. \tag{A.11}$$

The contractile "energy" of a cell, α, is determined as a function of its perimeter, P_α, and its area, A_α, as:

$$\mathcal{H}_{\text{cont}} = \sum_{\alpha} \left[m\, P_\alpha^2 + a\, A_\alpha^2\right]. \tag{A.12}$$

The parameters m and a hence characterize the contractility of a cell.

To account for the gain or loss of of "energy" in the system caused by the formation or breaking of cell-cell adhesions, adhesion matrices were defined. The matrix $A_{\alpha,\beta}$ determines the change in energy due to the formation of a new cell-cell contact between cells α and β while the matrix $B_{\alpha,\beta}$ determines the change in energy due to the breaking of a pre-existing cell-cell contact between both cells by a third "intruder" party $\gamma \neq \alpha, \beta$. Note that the index γ does not necessarily denote a cell but can also resemble unoccupied grid sites (corresponding to $\gamma < 0$).

The formation of new cell-cell contacts is implemented to be energetically favored while the breaking of existing cell-cell contacts is energetically penalized. This lead to a set of adhesion matrices of:

$$\begin{aligned}
A_{\alpha,\beta} &= A_{\beta,\alpha} \geq 0, && \text{(A.13a)}\\
B_{\alpha,\beta} &= B_{\beta,\alpha} \geq 0, && \text{(A.13b)}\\
A_{\alpha,\alpha} &= B_{\alpha,\alpha} = 0, && \text{(A.13c)}\\
A_{\alpha,\beta} &= B_{\alpha,\beta} = 0, \qquad \text{if } \alpha < 0 \vee \beta < 0. && \text{(A.13d)}
\end{aligned}$$

In order to account for the non-reversible character of cell adhesion, the energy penalty resulting from the break of an existing cell-cell adhesion was chosen larger than the energy gain of a newly formed adhesion, $B_{\alpha,\beta} \geq A_{\alpha,\beta}$. The energy difference for a given elementary event, $\mathcal{T}$, is hence calculated as

$$\Delta\mathcal{H}_{\text{adh}}(\mathcal{T}_{\text{pro}}) = -\sum_{\vec{x}_j \in \mathcal{N}_t} \left[A_{\alpha,c(\vec{x}_j)} - \delta_{\alpha,c(\vec{x}_j)}\, A_{\alpha,\beta}\right] + \sum_{\vec{x}_j \in \mathcal{N}_t} B_{\beta,c(\vec{x}_j)}(1 - \delta_{\alpha,c(\vec{x}_j)}), \tag{A.14a}$$

for protrusion events and

$$\Delta\mathcal{H}_{\mathrm{adh}}(\mathcal{T}_{\mathrm{ret}}) = -\sum_{\vec{x}_j \in \mathcal{N}_s} \left[A_{\beta,c(\vec{x}_j)} - \delta_{\beta,c(\vec{x}_j)}\, A_{\alpha,\beta}\right] + \sum_{\vec{x}_j \in \mathcal{N}_s} B_{\alpha,c(\vec{x}_j)}(1-\delta_{\beta,c(\vec{x}_j)}), \tag{A.14b}$$

for retraction events, respectively. Here, $\mathcal{N}_s$ and $\mathcal{N}_t$ denote the set of all directly adjacent grid sites to the source grid site, $\vec{x}_s$, and the target grid site, $\vec{x}_t$, respectively. In these equations, the first sum accounts for the formation of new cell-cell contacts and the remodeling of the interface between source cell, α, and target cell, β. The second sum accounts for the breaking of existing cell-cell contacts involving a third party $\gamma \neq \alpha, \beta$.

To account for intracellular polarization and the emergent active migration of living cells, the cell internal high-level features of the cytoskeletal dynamics are implemented in a third contribution to $p(\mathcal{T})$. This contribution is realized by a scalar field, $\rho(\vec{x}_n)$, $\vec{x}_n \in \mathcal{D}^{(\alpha)}$, resembling cytoskeletal activity within each cell. The actualization and dynamics of this cell internal field are determined by the following rules:

- ρ is limited by a upper and lower boundary $q \leq \rho(\vec{x}_n) \leq Q$.
- The actualization, ρ, is determined by "regulatory factors", $F(\vec{x}_n)$, for each grid site, $\vec{x}_n \in \mathcal{D}^{(\alpha)}$, of a cell, α. For these regulatory factors $F(\vec{x}_n) > 0$ corresponds to local conditions enhancing cytoskeleton assembly while $F(\vec{x}_n) \leq 0$ represents conditions under which the cytoskeleton is predominantly degraded.
- The regulatory factors, $F(\vec{x}_n)$, are coupled to the mechanical stimuli at the periphery of a cell α, $\mathcal{B}^{(\alpha)}$, across a finite spatial distance, R.
- For an accepted protrusion event the integer variable signifying regulatory factors of all grid sites within range R of the source grid site, $\vec{x}_s \in \mathcal{B}^{\alpha}$, is incremented for grit sites associated to source cell α and decremented for grit sites associated to target cell β:

$$F(\vec{x}_n) \to \begin{cases} F(\vec{x}_n) + 1, & \vec{x}_n \in \mathcal{D}^{(\alpha)}, \\ F(\vec{x}_n) - 1, & \vec{x}_n \in \mathcal{D}^{(\beta)}. \end{cases} \tag{A.15a}$$

- Correspondingly, for a accepted retraction event the integer variable signifying regulatory factors of all grid sites within range R of the source grid site, $\vec{x}_s \in \mathcal{B}^{\alpha}$, is decremented for grit sites associated to source cell α and decremented for grit sites associated to target cell β:

$$F(\vec{x}_n) \to \begin{cases} F(\vec{x}_n) - 1, & \vec{x}_n \in \mathcal{D}^{(\alpha)}, \\ F(\vec{x}_n) + 1, & \vec{x}_n \in \mathcal{D}^{(\beta)}. \end{cases} \tag{A.15b}$$

- In the case that a retraction event has been accepted at the source site, $\vec{x}_s \in \mathcal{B}^{\alpha}$, and the cell-cell contact between source cell α and target cell β is locally broken, the regulatory factors are only reduced for the retracting cell, α, while they are not affected for cell β (whose shape is not altered):

$$F(\vec{x}_n) \to \begin{cases} F(\vec{x}_n) - 1, & \vec{x}_n \in \mathcal{D}^{(\alpha)}, \\ \text{no update}, & \text{else}. \end{cases} \tag{A.15c}$$

If no second cell is involved and the target grid site, $\vec{x}_t$, is hence not occupied by any cell before the elementary event is taking place, only the first lines of Equations A.15 apply.

At the end of each MCS, the values of $F(\vec{x}_n)$ are used to update $\rho(\vec{x}_n)$ for each grid site, $\vec{x}_n$, within a cell. For $F(\vec{x}_n) > 0$ the value of $\rho(\vec{x}_n)$ is increased by an amount proportional to the deviation of $\rho(\vec{x}_n)$ from its upper bound Q:

$$\rho(\vec{x}_n, t + \Delta t) = \rho(\vec{x}_n, t) + \mu\,[Q - \rho(\vec{x}_n, t)]. \tag{A.16a}$$

Accordingly for $F(\vec{x}_n) \leq 0$ the value of $\rho(\vec{x}_n)$ is decreased by an amount proportional to the deviation of $\rho(\vec{x}_n)$ from its lower bound q:

$$\rho(\vec{x}_n, t + \Delta t) = \rho(\vec{x}_n, t) + \mu\,[q - \rho(\vec{x}_n, t)]. \tag{A.16b}$$

In these equations the parameter μ determines the rate at which the "cytoskeletal structure" of a cell responds to the regulatory factors, F. Finally, after the values of $\rho(\vec{x}_n)$ are updated, all regulatory factors are reset, $F(\vec{x}_n) = 0,\ \forall\, n$.

To allow the implementation of locally varying cell-substrate affinity, a second scalar field variable, $\varphi(\vec{x}_n)$, was introduced. In the course of this thesis, $\varphi(\vec{x}_n)$ was used to implement the restriction of cell adhesion and migration to the circular micropattern. The "energy difference" due to cytoskeletal remodeling is hence calculated as:

$$\Delta\mathcal{H}_{\text{cyto}}(\mathcal{T}) = \begin{cases} \rho(\vec{x}_t) - \rho(\vec{x}_s), & \mathcal{T} \mathrel{\widehat{=}} \mathcal{T}_{\text{pro}} \wedge \beta \geq 0, \\ \rho(\vec{x}_s) - \rho(\vec{x}_t), & \mathcal{T} \mathrel{\widehat{=}} \mathcal{T}_{\text{ret}} \wedge \beta \geq 0, \\ -\big[\rho(\vec{x}_s) + \varphi(\vec{x}_t)\big], & \mathcal{T} \mathrel{\widehat{=}} \mathcal{T}_{\text{pro}} \wedge \beta < 0, \\ \rho(\vec{x}_s) + \varphi(\vec{x}_t), & \mathcal{T} \mathrel{\widehat{=}} \mathcal{T}_{\text{ret}} \wedge \beta < 0. \end{cases} \tag{A.17}$$

Here, $\mathcal{T}_{\text{pro}}$ and $\mathcal{T}_{\text{ret}}$ indicate protrusion and retraction events, respectively. $\vec{x}_s$ and $\vec{x}_t$ denote the corresponding source and target grid sites while $\beta < 0$ indicates that $\vec{x}_t$ is not occupied by any cell prior to the elementary event.

The parameter values as they are used for the simulation runs relevant for this thesis are displayed in Table A.2.

TABLE A.2.: Parameter values used for the simulation runs in this thesis. As the simulated experimental conditions involved only a single cell type, the parameters values were the same for all cells in the simulation.

Name	Function	Value
R	signaling radius	4
A	adhesion strength (bond making)	0
B	adhesion strength (bond breaking)	7
m	cell contractility (perimeter stiffness)	0.021
a	cell contractility (area stiffness)	0.02
q / Q	lower / upper bound for cytoskeletal field	212 / 250
μ	cytoskeletal response rate	0.1

ASSOCIATED PUBLICATIONS

In the following, the publications associated with this thesis are listed.

1. **Emergence and Persistence of Collective Cell Migration on Small Circular Micropatterns**
   Felix J. Segerer*, Florian Thüroff*, Alicia Piera Alberola, Erwin Frey, and Joachim O. Rädler.
   In: *Physical Review Letters*, 114 (2015), 22, 228102.
2. **A versatile method to generate multiple types of micropatterns**
   Felix J. Segerer, Peter J. F. Röttgermann, Simon Schuster, Alicia Piera Alberola, Stefan Zahler, and Joachim O. Rädler.
   In: *Biointerphases*, 11 (2016), 1, 011005.
3. **Ring-Shaped Microlanes and Chemical Barriers as a Platform for Probing Single-Cell Migration**
   Christoph Schreiber*, Felix J. Segerer*, Ernst Wagner, Andreas Roidl, and Joachim O. Rädler.
   In: *Scientific Reports*, 6 (2016), 26858.
4. **Contractility as a global regulator of cellular morphology, velocity, and directionality in low-adhesive fibrillary micro-environments**
   Simon Schuster, Felix J. Segerer, Florian A. Gegenfurtner, Kerstin Kick, Christoph Schreiber, Max Albert, Angelika M. Vollmar, Joachim O. Rädler, and Stefan Zahler.
   In: *Biomaterials*, 102 (2016), 137-147.
5. **Cell motility on polyethylene glycol block copolymers correlates to fibronectin surface adsorption**
   Peter J. F. Röttgermann, Samira Hertrich, Ida Berths, Max Albert, Felix J. Segerer, Jean-François Moulin, Bert Nickel, and Joachim O. Rädler.
   In: *Macromolecular Bioscience*, 14 (2014), 12, 1755–1763.
6. **Phenomenological approaches to collective behavior in epithelial cell migration**
   Matthias L. Zorn, Anna-Kristina Marel, Felix J. Segerer, and Joachim O. Rädler.
   In: *Biochimica et Biophysica Acta (BBA) - Molecular Cell Research*, 1853 (2015), 11 B, 3143-3152.

---

*These authors contributed equally.

LIST OF ABBREVIATIONS

CAMo: Coherent Angular Motion

ccw: counterclockwise

CIL: Contact Inhibition of Locomotion

COC: Cyclic Olefin Copolymer

CP: Change Point

CPM: Cellular Potts Model

CUSUM: Cumulative Sum

cw: clockwise

DisMo: Disordered Motion

DMSO: Dimethyl Sulfoxide

ECM: Extracellular Matrix

EDTA: Ethylenediaminetetraacetic acid

FCS: Fetal Calf Serum

HUVEC: Human Umbilical Vein Endothelial Cell

L-Glu: L-Glutamine

MCS: Monte Carlo Step

MDCK: Madin-Darby Canine Kidney

mM: milli Molar

MSD: Mean Squared Displacement

MTOC: Microtubule Organizing Center

µCP: Micro Contact Printing

µPIP: Plasma-Induced Protein Patterning

MW: Molecular Weight

PBS: Phosphate-Buffered Saline

PDMS: Poly(Dimethyl-Siloxane)

PEG: Poly(Ethylene-Glycol)

PLL: Poly(L-Lysine)

PPO: Poly(Propylene-Oxide)

PSA: penicillin/streptavidin/amphotericin B

px: Pixels

tc-PS: Tissue Culture Poly(Styrene)

UV: Ultraviolet

BIBLIOGRAPHY

[1] MADRI, J. A. ; GRAESSER, D.: Cell migration in the immune system: the evolving inter-related roles of adhesion molecules and proteinases. In: *Dev. Immunol.* 7 (2000), 2-4, 103–116

[2] NOURSHARGH, S. ; ALON, R.: Leukocyte migration into inflamed tissues. In: *Immunity* 41 (2014), 5, 694–707

[3] DEVOTO, S. H.: Neuronal growth cone migration. In: *Experientia* 46 (1990), 9, 916–922

[4] COOPER, J. A.: Cell biology in neuroscience: mechanisms of cell migration in the nervous system. In: *J. Cell Biol.* 202 (2013), 5, 725–34

[5] EWALD, A. J. ; BRENOT, A. ; DUONG, M. ; CHAN, B. S. ; WERB, Z.: Collective epithelial migration and cell rearrangements drive mammary branching morphogenesis. In: *Dev. Cell.* 14 (2008), 4, 570–81

[6] VASILYEV, A. ; LIU, Y. ; MUDUMANA, S. ; MANGOS, S. ; LAM, P. Y. ; MAJUMDAR, A. ; ZHAO, J. ; POON, K. L. ; KONDRYCHYN, I. ; KORZH, V. ; DRUMMOND, I. A.: Collective cell migration drives morphogenesis of the kidney nephron. In: *PLoS Biol.* 7 (2009), 1, e9

[7] LECAUDEY, V. ; GILMOUR, D.: Organizing moving groups during morphogenesis. In: *Curr. Opin. Cell Biol.* 18 (2006), 1, 102–7

[8] ARIMA, S. ; NISHIYAMA, K. ; KO, T. ; ARIMA, Y. ; HAKOZAKI, Y. ; SUGIHARA, K. ; KOSEKI, H. ; UCHIJIMA, Y. ; KURIHARA, Y. ; KURIHARA, H.: Angiogenic morphogenesis driven by dynamic and heterogeneous collective endothelial cell movement. In: *Development* 138 (2011), 21, 4763–76

[9] SHAW, T. J. ; MARTIN, P.: Wound repair at a glance. In: *J. Cell Sci.* 122 (2009), Pt 18, 3209–13

[10] POUJADE, M. ; GRASLAND-MONGRAIN, E. ; HERTZOG, A. ; JOUANNEAU, J. ; CHAVRIER, P. ; LADOUX, B. ; BUGUIN, A. ; SILBERZAN, P.: Collective migration of an epithelial monolayer in response to a model wound. In: *Proc. Natl. Acad. Sci. USA* 104 (2007), 41, 15988–15993

[11] DEISBOECK, T. S. ; COUZIN, I. D.: Collective behavior in cancer cell populations. In: *BioEssays* 31 (2009), 2, 190–7

[12] FRIEDL, P. ; WOLF, K.: Tumour-cell invasion and migration: diversity and escape mechanisms. In: *Nat. Rev. Cancer* 3 (2003), 5, 362–374

[13] MAIURI, P. ; TERRIAC, E. ; PAUL-GILLOTEAUX, P. ; VIGNAUD, T. ; MCNALLY, K. ; ONUFFER, J. ; THORN, K. ; NGUYEN, P. A. ; GEORGOULIA, N. ; SOONG, D. ; JAYO, A. ; BEIL, N. ; BENEKE, J. ; HONG LIM, J. C. ; PEI-YING SIM, C. ; CHU, Y.-S. ; JIMÉNEZ-DALMARONI, A. ; JOANNY, J.-F. c. ; THIERY, J.-P. ; ERFLE, H. ; PARSONS, M. ; MITCHISON, T. J. ; LIM, W. A. ; LENNON-DUMÉNIL, A.-M. ; PIEL, M. ; THÉRY, M.: The first World Cell Race. In: *Curr. Biol.* 22 (2012), 17, R673–R675

[14] CHARRAS, G. ; SAHAI, E.: Physical influences of the extracellular environment on cell migration. In: *Nat. Rev. Mol. Cell Biol.* 15 (2014), 12, 813–24

[15] WONG, I. Y. ; JAVAID, S. ; WONG, E. A. ; PERK, S. ; HABER, D. A. ; TONER, M. ; IRIMIA, D.: Collective and individual migration following the epithelial-mesenchymal transition. In: *Nat. Mater.* 13 (2014), 11, 1063–1071

[16] LO, C.-M. ; WANG, H.-B. ; DEMBO, M. ; WANG, Y.-l.: Cell Movement Is Guided by the Rigidity of the Substrate. In: *Biophys. J.* 79 (2000), 1, 144–152

[17] MAHESHWARI, G. ; BROWN, G. ; LAUFFENBURGER, D. ; WELLS, A. ; GRIFFITH, L.: Cell adhesion and motility depend on nanoscale RGD clustering. In: *J. Cell Sci.* 113 (2000), 10, 1677–1686

[18] PETITJEAN, L. ; REFFAY, M. ; GRASLAND-MONGRAIN, E. ; POUJADE, M. ; LADOUX, B. ; BUGUIN, A. ; SILBERZAN, P.: Velocity Fields in a Collectively Migrating Epithelium. In: *Biophys. J.* 98 (2010), 9, 1790–1800

[19] ANGELINI, T. E. ; HANNEZO, E. ; TREPAT, X. ; FREDBERG, J. J. ; WEITZ, D. A.: Cell Migration Driven by Cooperative Substrate Deformation Patterns. In: *Phys. Rev. Lett.* 104 (2010), 16, 168104

[20] GARCIA, S. ; HANNEZO, E. ; ELGETI, J. ; JOANNY, J.-F. c. ; SILBERZAN, P. ; GOV, N. S.: Physics of active jamming during collective cellular motion in a monolayer. In: *Proc. Natl. Acad. Sci. USA* 112 (2015), 50, 15314–15319

[21] RUBINSTEIN, B. ; JACOBSON, K. ; MOGILNER, A.: Multiscale Two-Dimensional Modeling of a Motile Simple-Shaped Cell. In: *Multiscale Model Simul.* 3 (2005), 2, 413–439

[22] NONAKA, S. ; NAOKI, H. ; ISHII, S.: A multiphysical model of cell migration integrating reaction-diffusion, membrane and cytoskeleton. In: *Neural Netw.* 24 (2011), 9, 979–989

[23] Shao, D. ; Levine, H. ; Rappel, W.-J.: Coupling actin flow, adhesion, and morphology in a computational cell motility model. In: *Proc. Natl. Acad. Sci. USA* 109 (2012), 18, 6851–6856

[24] Löber, J. ; Ziebert, F. ; Aranson, I. S.: Collisions of deformable cells lead to collective migration. In: *Sci. Rep.* 5 (2015), 9172

[25] Szabó, B. ; Szöllösi, G. J. ; Gönci, B. ; Jurányi, Z. ; Selmeczi, D. ; Vicsek, T.: Phase transition in the collective migration of tissue cells: Experiment and model. In: *Phys. Rev. E Stat. Nonlin. Soft. Matter Phys.* 74 (2006), 6 Pt 1, 061908

[26] Basan, M. ; Elgeti, J. ; Hannezo, E. ; Rappel, W.-J. ; Levine, H.: Alignment of cellular motility forces with tissue flow as a mechanism for efficient wound healing. In: *Proc. Natl. Acad. Sci. USA* 110 (2013), 7, 2452–2459

[27] Sepulveda, N. ; Petitjean, L. ; Cochet, O. ; Grasland-Mongrain, E. ; Silberzan, P. ; Hakim, V.: Collective cell motion in an epithelial sheet can be quantitatively described by a stochastic interacting particle model. In: *PLoS Comput. Biol.* 9 (2013), 3, e1002944

[28] Ferizi, M. ; Leonhardt, C. ; Meggle, C. ; Aneja, M. K. ; Rudolph, C. ; Plank, C. ; Rädler, J. O.: Stability analysis of chemically modified mRNA using micropattern-based single-cell arrays. In: *Lab Chip* 15 (2015), 3561–3571

[29] Théry, M. ; Racine, V. ; Pépin, A. ; Piel, M. ; Chen, Y. ; Sibarita, J. B. ; Bornens, M.: The extracellular matrix guides the orientation of the cell division axis. In: *Nat. Cell Biol.* 7 (2005), 10, 947–53

[30] Théry, M. ; Racine, V. ; Piel, M. ; Pépin, A. ; Dimitrov, A. ; Chen, Y. ; Sibarita, J.-B. ; Bornens, M.: Anisotropy of cell adhesive microenvironment governs cell internal organization and orientation of polarity. In: *Proc. Natl. Acad. Sci. USA* 103 (2006), 52, 19771–19776

[31] Jiang, X. ; Bruzewicz, D. A. ; Wong, A. P. ; Piel, M. ; Whitesides, G. M.: Directing cell migration with asymmetric micropatterns. In: *Proc. Natl. Acad. Sci. USA* 102 (2005), 4, 975–978

[32] Tseng, Q. ; Duchemin-Pelletier, E. ; Deshiere, A. ; Balland, M. ; Guillou, H. ; Filhol, O. ; Théry, M.: Spatial organization of the extracellular matrix regulates cell-cell junction positioning. In: *Proc. Natl. Acad. Sci. USA* 109 (2012), 5, 1506–1511

[33] Desai, R. A. ; Gao, L. ; Raghavan, S. ; Liu, W. F. ; Chen, C. S.: Cell polarity triggered by cell-cell adhesion via E-cadherin. In: *J. Cell Sci.* 122 (2009), 7, 905–911

[34] MAHMUD, G. ; CAMPBELL, C. J. ; BISHOP, K. J. M. ; KOMAROVA, Y. A. ; CHAGA, O. ; SOH, S. ; HUDA, S. ; KANDERE-GRZYBOWSKA, K. ; GRZYBOWSKI, B. A.: Directing cell motions on micropatterned ratchets. In: *Nature Phys.* 5 (2009), 8, 606–612

[35] YOON, S. H. ; KIM, Y. K. ; HAN, E. D. ; SEO, Y. H. ; KIM, B. H. ; MOFRAD, M. R.: Passive control of cell locomotion using micropatterns: the effect of micropattern geometry on the migratory behavior of adherent cells. In: *Lab Chip* 12 (2012), 13, 2391–402

[36] SCHREIBER, C. ; SEGERER, F. J. ; WAGNER, E. ; ROIDL, A. ; RADLER, J. O.: Ring-Shaped Microlanes and Chemical Barriers as a Platform for Probing Single-Cell Migration. In: *Sci. Rep.* 6 (2016), 26858

[37] SCHUSTER, S. L. ; SEGERER, F. J. ; GEGENFURTNER, F. A. ; KICK, K. ; SCHREIBER, C. ; ALBERT, M. ; VOLLMAR, A. M. ; RÄDLER, J. O. ; ZAHLER, S.: Contractility as a global regulator of cellular morphology, velocity, and directionality in low-adhesive fibrillary micro-environments. In: *Biomaterials* 102 (2016), 137–147

[38] SEGERER, F. J. ; THÜROFF, F. ; PIERA ALBEROLA, A. ; FREY, E. ; RÄDLER, J. O.: Emergence and Persistence of Collective Cell Migration on Small Circular Micropatterns. In: *Phys. Rev. Lett.* 114 (2015), 22, 228102

[39] MAREL, A. K. ; ZORN, M. ; KLINGNER, C. ; WEDLICH-SÖLDNER, R. ; FREY, E. ; RÄDLER, J. O.: Flow and diffusion in channel-guided cell migration. In: *Biophys. J.* 107 (2014), 5, 1054–64

[40] DESAI, R. A. ; GOPAL, S. B. ; CHEN, S. ; CHEN, C. S.: Contact inhibition of locomotion probabilities drive solitary versus collective cell migration. In: *J. R. Soc. Interface* 10 (2013), 88, 20130717

[41] DOYLE, A. D. ; WANG, F. W. ; MATSUMOTO, K. ; YAMADA, K. M.: One-dimensional topography underlies three-dimensional fibrillar cell migration. In: *J. Cell Biol.* 184 (2009), 4, 481–90

[42] MAIURI, P. ; RUPPRECHT, J. F. ; WIESER, S. ; RUPRECHT, V. ; BENICHOU, O. ; CARPI, N. ; COPPEY, M. ; DE BECO, S. ; GOV, N. ; HEISENBERG, C. P. ; LAGE CRESPO, C. ; LAUTENSCHLAEGER, F. ; LE BERRE, M. ; LENNON-DUMENIL, A. M. ; RAAB, M. ; THIAM, H. R. ; PIEL, M. ; SIXT, M. ; VOITURIEZ, R.: Actin Flows Mediate a Universal Coupling between Cell Speed and Cell Persistence. In: *Cell* 161 (2015), 2, 374–86

[43] HUANG, S. ; BRANGWYNNE, C. P. ; PARKER, K. K. ; INGBER, D. E.: Symmetry-breaking in mammalian cell cohort migration during tissue pattern formation: Role of random-walk persistence. In: *Cell Motil. Cytoskeleton* 61 (2005), 4, 201–213

[44] DOXZEN, K. ; VEDULA, S. R. K. ; LEONG, M. C. ; HIRATA, H. ; GOV, N. ; KABLA, A. J. ; LADOUX, B. ; LIM, C. T.: Guidance of collective cell migration by substrate geometry. In: *Integr. Biol.* 5 (2013), 1026–1035

[45] DEFORET, M. ; HAKIM, V. ; YEVICK, H. G. ; DUCLOS, G. ; SILBERZAN, P.: Emergence of collective modes and tri-dimensional structures from epithelial confinement. In: *Nat. Commun.* 5 (2014), 3747, 3747

[46] FLETCHER, D. A. ; MULLINS, R. D.: Cell mechanics and the cytoskeleton. In: *Nature* 463 (2010), 7280, 485–492

[47] ALLEN, C. ; BORISY, G. G.: Structural polarity and directional growth of microtubules of Chlamydomonas flagella. In: *J. Mol. Biol.* 90 (1974), 2, 381–402

[48] LUDERS, J. ; STEARNS, T.: Microtubule-organizing centres: a re-evaluation. In: *Nat. Rev. Mol. Cell Biol.* 8 (2007), 2, 161–167

[49] DESAI, A. ; MITCHISON, T. J.: Microtubule Polymerization Dynamics. In: *Annu. Rev. Cell Dev. Biol.* 13 (1997), 1, 83–117

[50] GOODE, B. L. ; DRUBIN, D. G. ; BARNES, G.: Functional cooperation between the microtubule and actin cytoskeletons. In: *Curr. Opin. Cell Biol.* 12 (2000), 1, 63–71

[51] WATANABE, T. ; NORITAKE, J. ; KAIBUCHI, K.: Regulation of microtubules in cell migration. In: *Trends Cell Biol.* 15 (2005), 2, 76–83

[52] ETIENNE-MANNEVILLE, S.: Polarity proteins in migration and invasion. In: *Annu. Rev. Cell Dev. Biol.* 27 (2008), 55, 6970–80

[53] ALBERTS, B. ; JOHNSON, A. ; LEWIS, J. ; RAFF, M. ; ROBERTS, K. ; WALTER, P.: *Molecular biology of the cell*. Garland Science, 2002

[54] SACKMANN, E. ; MERKEL, R.: *Lehrbuch der Biophysik*. Weinheim : WILEY-VCH Verlag & Co., 2010

[55] POLLARD, T. D. ; BORISY, G. G.: Cellular Motility Driven by Assembly and Disassembly of Actin Filaments. In: *Cell* 112 (2003), 4, 453–465

[56] LAUFFENBURGER, D. A. ; HORWITZ, A. F.: Cell Migration: A Physically Integrated Molecular Process. In: *Cell* 84 (1996), 3, 359–369

[57] FRANTZ, C. ; STEWART, K. M. ; WEAVER, V. M.: The extracellular matrix at a glance. In: *J. Cell Sci.* 123 (2010), 24, 4195–4200

[58] HUTTENLOCHER, A. ; HORWITZ, A. R.: Integrins in cell migration. In: *Cold Spring Harb. Perspect. Biol.* 3 (2011), 9, a005074

[59] CAVEY, M. ; LECUIT, T.: Molecular Bases of Cell-Cell Junctions Stability and Dynamics. In: *Cold Spring Harb. Perspect. Biol.* 1 (2009), 5

[60] LECKBAND, D. E. ; ROOIJ, J. de: Cadherin adhesion and mechanotransduction. In: *Annu. Rev. Cell Dev. Biol.* 30 (2014), 291–315

[61] SCHWARTZ, M. A.: Integrins and extracellular matrix in mechanotransduction. In: *Cold Spring Harb. Perspect. Biol.* 2 (2010), 12, a005066

[62] WATERMAN-STORER, C. M. ; SALMON, E. D.: Positive feedback interactions between microtubule and actin dynamics during cell motility. In: *Curr. Opin. Cell Biol.* 11 (1999), 1, 61–67

[63] CLARK, A. G. ; VIGNJEVIC, D. M.: Modes of cancer cell invasion and the role of the microenvironment. In: *Curr. Opin. Cell Biol.* 36 (2015), 13–22

[64] TREPAT, X. ; WASSERMAN, M. R. ; ANGELINI, T. E. ; MILLET, E. ; WEITZ, D. A. ; BUTLER, J. P. ; FREDBERG, J. J.: Physical forces during collective cell migration. In: *Nat. Phys.* 5 (2009), 6, 426–430

[65] TAMBE, D. T. ; COREY HARDIN, C. ; ANGELINI, T. E. ; RAJENDRAN, K. ; PARK, C. Y. ; SERRA-PICAMAL, X. ; ZHOU, E. H. ; ZAMAN, M. H. ; BUTLER, J. P. ; WEITZ, D. A. ; FREDBERG, J. J. ; TREPAT, X.: Collective cell guidance by cooperative intercellular forces. In: *Nat. Mater.* 10 (2011), 6, 469–475

[66] TREPAT, X. ; FREDBERG, J. J.: Plithotaxis and emergent dynamics in collective cellular migration. In: *Trends Cell Biol.* 21 (2011), 11, 638–46

[67] HAEGER, A. ; WOLF, K. ; ZEGERS, M. M. ; FRIEDL, P.: Collective cell migration: guidance principles and hierarchies. In: *Trends Cell Biol.* 25 (2015), 9, 556–66

[68] SCARPA, E. ; MAYOR, R.: Collective cell migration in development. In: *J. Cell Biol.* 212 (2016), 2, 143–55

[69] CAI, D. ; MONTELL, D. J.: Diverse and dynamic sources and sinks in gradient formation and directed migration. In: *Curr. Opin. Cell Biol.* 30 (2014), 91–8

[70] THEVENEAU, E. ; MARCHANT, L. ; KURIYAMA, S. ; GULL, M. ; MOEPPS, B. ; PARSONS, M. ; MAYOR, R.: Collective Chemotaxis Requires Contact-Dependent Cell Polarity. In: *Dev. Cell* 19 (2010), 1, 39–53

[71] ABERCROMBIE, M. ; HEAYSMAN, J. E. M.: Observations on the social behaviour of cells in tissue culture. In: *Exp. Cell. Res.* 6 (1954), 2, 293–306

[72] ABERCROMBIE, M.: Contact inhibition in tissue culture. In: *In Vitro* 6 (1970), 2, 128–142

[73] MAYOR, R. ; CARMONA-FONTAINE, C.: Keeping in touch with contact inhibition of locomotion. In: *Trends Cell Biol.* 20 (2010), 6, 319–28

[74] OMELCHENKO, T. ; VASILIEV, J. M. ; GELFAND, I. M. ; FEDER, H. H. ; BONDER, E. M.: Rho-dependent formation of epithelial "leader" cells during wound healing. In: *Proc. Natl. Acad. Sci. USA* 100 (2003), 19, 10788–10793

[75] VEDULA, S. R. K. ; LEONG, M. C. ; LAI, T. L. ; HERSEN, P. ; KABLA, A. J. ; LIM, C. T. ; LADOUX, B.: Emerging modes of collective cell migration induced by geometrical constraints. In: *Proc. Natl. Acad. Sci. USA* (2012)

[76] ANGELINI, T. E. ; HANNEZO, E. ; TREPAT, X. ; MARQUEZ, M. ; FREDBERG, J. J. ; WEITZ, D. A.: Glass-like dynamics of collective cell migration. In: *Proc. Natl. Acad. Sci. USA* (2011)

[77] ZHAO, M.: Electrical fields in wound healing–An overriding signal that directs cell migration. In: *Sem. Cell Dev. Biol.* 20 (2009), 6, 674–682

[78] COHEN, D. J. ; JAMES NELSON, W. ; MAHARBIZ, M. M.: Galvanotactic control of collective cell migration in epithelial monolayers. In: *Nat. Mater.* 13 (2014), 4, 409–417

[79] DRISCOLL, M. K. ; SUN, X. ; GUVEN, C. ; FOURKAS, J. T. ; LOSERT, W.: Cellular Contact Guidance through Dynamic Sensing of Nanotopography. In: *ACS Nano* 8 (2014), 4, 3546–3555

[80] ROCA-CUSACHS, P. ; SUNYER, R. ; TREPAT, X.: Mechanical guidance of cell migration: lessons from chemotaxis. In: *Curr. Opin. Cell Biol.* 25 (2013), 5, 543–9

[81] LAMALICE, L. ; LE BOEUF, F. ; HUOT, J.: Endothelial cell migration during angiogenesis. In: *Circ. Res.* 100 (2007), 6, 782–94

[82] SHAMLOO, A. ; MA, N. ; POO, M. M. ; SOHN, L. L. ; HEILSHORN, S. C.: Endothelial cell polarization and chemotaxis in a microfluidic device. In: *Lab Chip* 8 (2008), 8, 1292–9

[83] ZHENG, J. Q. ; FELDER, M. ; CONNOR, J. A. ; POO, M.-m.: Turning of nerve growth cones induced by neurotransmitters. In: *Nature* 368 (1994), 6467, 140–144

[84] MING, G.-l. ; WONG, S. T. ; HENLEY, J. ; YUAN, X.-b. ; SONG, H.-j. ; SPITZER, N. C. ; POO, M.-m.: Adaptation in the chemotactic guidance of nerve growth cones. In: *Nature* 417 (2002), 6887, 411–418

[85] SMITH, J. T. ; TOMFOHR, J. K. ; WELLS, M. C. ; BEEBE, T. P. ; KEPLER, T. B. ; REICHERT, W. M.: Measurement of Cell Migration on Surface-Bound Fibronectin Gradients. In: *Langmuir* 20 (2004), 19, 8279–8286

[86] Liu, L. ; Ratner, B. D. ; Sage, E. H. ; Jiang, S.: Endothelial Cell Migration on Surface-Density Gradients of Fibronectin, VEGF, or Both Proteins. In: *Langmuir* 23 (2007), 22, 11168–11173

[87] Cai, K. ; Kong, T. ; Wang, L. ; Liu, P. ; Yang, W. ; Chen, C.: Regulation of endothelial cells migration on poly(D, L-lactic acid) films immobilized with collagen gradients. In: *Colloids Surf., B* 79 (2010), 1, 291–7

[88] King, S. J. ; Asokan, S. B. ; Haynes, E. M. ; Zimmerman, S. P. ; Rotty, J. D. ; Alb, J. J. G. J. G. ; Tagliatela, A. ; Blake, D. R. ; Lebedeva, I. P. ; Marston, D. ; Johnson, H. E. ; Parsons, M. ; Sharpless, N. E. ; Kuhlman, B. ; Haugh, J. M. ; Bear, J. E.: Lamellipodia are critical for haptotactic sensing and response. In: *J. Cell. Sci.* (2016)

[89] Nakanishi, K. ; Sakiyama, T. ; Imamura, K.: On the adsorption of proteins on solid surfaces, a common but very complicated phenomenon. In: *J. Biosci. Bioeng.* 91 (2001), 3, 233–244

[90] Roach, P. ; Farrar, D. ; Perry, C. C.: Interpretation of Protein Adsorption: Surface-Induced Conformational Changes. In: *Journal of the American Chemical Society* 127 (2005), 22, 8168–8173

[91] Ballet, T. ; Boulange, L. ; Brechet, Y. ; Bruckert, F. ; Weidenhaupt, M.: Protein conformational changes induced by adsorption onto material surfaces: an important issue for biomedical applications of material science. In: *Bull. Pol. Acad. Sci., Tech. Sci.* 58 (2010), 2, 303

[92] Fitchmun, M. I. ; Falk-Marzillier, J. ; Marshall, E. ; Cruz, G. ; Jones, J. C. R. ; Quaranta, V.: Mode of Adsorption and Orientation of an Extracellular Matrix Protein Affect Its Cell-Adhesion-Promoting Activity. In: *Anal. Biochem.* 265 (1998), 1, 1–7

[93] Cooke, M. J. ; Phillips, S. R. ; Shah, D. S. ; Athey, D. ; Lakey, J. H. ; Przyborski, S. A.: Enhanced cell attachment using a novel cell culture surface presenting functional domains from extracellular matrix proteins. In: *Cytotechnology* 56 (2008), 2, 71–9

[94] Michel, R. ; Pasche, S. ; Textor, M. ; Castner, D. G.: Influence of PEG Architecture on Protein Adsorption and Conformation. In: *Langmuir* 21 (2005), 26, 12327–12332

[95] Pozzi, D. ; Colapicchioni, V. ; Caracciolo, G. ; Piovesana, S. ; Capriotti, A. L. ; Palchetti, S. ; De Grossi, S. ; Riccioli, A. ; Amenitsch, H. ; Laganà,

A.: Effect of polyethyleneglycol (PEG) chain length on the bio-nano-interactions between PEGylated lipid nanoparticles and biological fluids: from nanostructure to uptake in cancer cells. In: *Nanoscale* 6 (2014), 5, 2782

[96] RÖTTGERMANN, P. J. ; HERTRICH, S. ; BERTS, I. ; ALBERT, M. ; SEGERER, F. J. ; MOULIN, J. F. ; NICKEL, B. ; RADLER, J. O.: Cell motility on polyethylene glycol block copolymers correlates to fibronectin surface adsorption. In: *Macromol. Biosci.* 14 (2014), 12, 1755–1763

[97] WILBUR, J. L. ; KUMAR, A. ; KIM, E. ; WHITESIDES, G. M.: Microfabrication by microcontact printing of self-assembled monolayers. In: *Adv. Mater.* 6 (1994), 7-8, 600–604

[98] ALOM RUIZ, S. ; CHEN, C. S.: Microcontact printing: A tool to pattern. In: *Soft Matter* 3 (2007), 2, 168

[99] THÉRY, M. ; PIEL, M.: Adhesive micropatterns for cells: a microcontact printing protocol. In: *Cold Spring Harb. Protoc.* 4 (2009), 7, pdb.prot5255

[100] NAKANISHI, J. ; KIKUCHI, Y. ; TAKARADA, T. ; NAKAYAMA, H. ; YAMAGUCHI, K. ; MAEDA, M.: Photoactivation of a Substrate for Cell Adhesion under Standard Fluorescence Microscopes. In: *J. Am. Chem. Soc.* 126 (2004), 50, 16314–16315

[101] AZIOUNE, A. ; STORCH, M. ; BORNENS, M. ; THÉRY, M. ; PIEL, M.: Simple and rapid process for single cell micro-patterning. In: *Lab Chip* 9 (2009), 11, 1640–1642

[102] KIM, M. ; CHOI, J.-C. ; JUNG, H.-R. ; KATZ, J. S. ; KIM, M.-G. ; DOH, J.: Addressable Micropatterning of Multiple Proteins and Cells by Microscope Projection Photolithography Based on a Protein Friendly Photoresist. In: *Langmuir* 26 (2010), 14, 12112–12118

[103] ROLLI, C. G. ; NAKAYAMA, H. ; YAMAGUCHI, K. ; SPATZ, J. P. ; KEMKEMER, R. ; NAKANISHI, J.: Switchable adhesive substrates: Revealing geometry dependence in collective cell behavior. In: *Biomaterials* 33 (2012), 8, 2409–2418

[104] BÉLISLE, J. M. ; KUNIK, D. ; COSTANTINO, S.: Rapid multicomponent optical protein patterning. In: *Lab Chip* 9 (2009), 24, 3580–5

[105] LANGOWSKI, B. A. ; UHRICH, K. E.: Microscale Plasma-Initiated Patterning (μPIP). In: *Langmuir* 21 (2005), 23, 10509–10514

[106] CHENG, Q. ; KOMVOPOULOS, K.: Integration of plasma-assisted surface chemical modification, soft lithography, and protein surface activation for single-cell patterning. In: *Appl. Phys. Lett.* 97 (2010), 4, 043705

[107] JUNKIN, M. ; WONG, P. K.: Probing cell migration in confined environments by plasma lithography. In: *Biomaterials* 32 (2011), 7, 1848–1855

[108] TOUROVSKAIA, A. ; BARBER, T. ; WICKES, B. T. ; HIRDES, D. ; GRIN, B. ; CASTNER, D. G. ; HEALY, K. E. ; FOLCH, A.: Micropatterns of Chemisorbed Cell Adhesion-Repellent Films Using Oxygen Plasma Etching and Elastomeric Masks. In: *Langmuir* 19 (2003), 11, 4754–4764

[109] PICONE, R. ; BAUM, B. ; MCKENDRY, R.: Plasma Microcontact Patterning (PμCP): A Technique for the Precise Control of Surface Patterning at Small-Scale. In: PIEL, M. (editor) ; THÉRY, M. (editor): *Methods Cell Biol.* Vol. 119. Academic Press, 2014, Kapitel 5, 73–90

[110] KIM, J. H. ; SEO, S. ; MIN, J.: Epithelial cell patterns on a PDMS polymer surface using a micro plasma structure. In: *J. Biotechnol.* 155 (2011), 3, 308–11

[111] BERNARD, A. ; RENAULT, J. P. ; MICHEL, B. ; BOSSHARD, H. R. ; DELAMARCHE, E.: Microcontact Printing of Proteins. In: *Advanced Materials* 12 (2000), 14, 1067–1070

[112] EICHINGER, C. D. ; HSIAO, T. W. ; HLADY, V.: Multiprotein microcontact printing with micrometer resolution. In: *Langmuir* 28 (2012), 4, 2238–43

[113] GROPEANU, M. ; BHAGAWATI, M. ; GROPEANU, R. A. ; RODRIGUEZ MUNIZ, G. M. ; SUNDARAM, S. ; PIEHLER, J. ; CAMPO, A. del: A versatile toolbox for multiplexed protein micropatterning by laser lithography. In: *Small* 9 (2013), 6, 838–45

[114] CRANK, J.: *The Mathematics of Diffusion (Oxford Science Publications).* Oxford University Press, 1980

[115] LARSSON, U. ; BLOMBÄCK, B. ; RIGLER, R.: Fibrinogen and the early stages of polymerization to fibrin as studied by dynamic laser light scattering. In: *Biochim. Biophys. Acta (BBA) - Protein Struct. M.* 915 (1987), 2, 172–179

[116] UHLENBECK, G. E. ; ORNSTEIN, L. S.: On the Theory of the Brownian Motion. In: *Phys. Rev. E* 36 (1930), 5, 823–841

[117] GAIL, M. H. ; BOONE, C. W.: The Locomotion of Mouse Fibroblasts in Tissue Culture. In: *Biophys. J.* 10 (1970), 10, 980–993

[118] STOKES, C. L. ; LAUFFENBURGER, D. A. ; WILLIAMS, S. K.: Migration of individual microvessel endothelial cells: stochastic model and parameter measurement. In: *J. Cell Sci.* 99 (1991), 2, 419–430

[119] WRIGHT, A. ; LI, Y. H. ; ZHU, C.: The differential effect of endothelial cell factors on in vitro motility of malignant and non-malignant cells. In: *Ann. Biomed. Eng.* 36 (2008), 6, 958–69

[120] LEMONS, D. S.: Paul Langevin's 1908 paper "On the Theory of Brownian Motion" ["Sur la théorie du mouvement brownien," C. R. Acad. Sci. (Paris) 146, 530-533 (1908)]. In: *Am. J. Phys.* 65 (1997), 11, 1079

[121] FÜRTH, R.: Die Brownsche Bewegung bei Berücksichtigung einer Persistenz der Bewegungsrichtung. Mit Anwendungen auf die Bewegung lebender Infusorien. In: *Z. Phys.* 2 (1920), 3, 244–256

[122] EINSTEIN, A.: Über die von der molekularkinetischen Theorie der Wärme geforderte Bewegung von in ruhenden Flüssigkeiten suspendierten Teilchen. In: *Ann. Phys. (Berlin)* 322 (1905), 8, 549–560

[123] SELMECZI, D. ; LI, L. ; PEDERSEN, L. I. I. ; NRRELYKKE, S. F. ; HAGEDORN, P. H. ; MOSLER, S. ; LARSEN, N. B. ; COX, E. C. ; FLYVBJERG, H.: Cell motility as random motion: A review. In: *Eur. Phys. J. Special Topics* 157 (2008), 1, 1–15

[124] DIETERICH, P. ; KLAGES, R. ; PREUSS, R. ; SCHWAB, A.: Anomalous dynamics of cell migration. In: *Proc. Natl. Acad. Sci. USA* 105 (2008), 2, 459–63

[125] TAKAGI, H. ; SATO, M. J. ; YANAGIDA, T. ; UEDA, M.: Functional Analysis of Spontaneous Cell Movement under Different Physiological Conditions. In: *PLoS ONE* 3 (2008), 7, e2648

[126] CAMPOS, D. ; MENDEZ, V. ; LLOPIS, I.: Persistent random motion: uncovering cell migration dynamics. In: *J. Theor. Biol.* 267 (2010), 4, 526–34

[127] POTDAR, A. A. ; JEON, J. ; WEAVER, A. M. ; QUARANTA, V. ; CUMMINGS, P. T.: Human Mammary Epithelial Cells Exhibit a Bimodal Correlated Random Walk Pattern. In: *PLoS ONE* 5 (2010), 3, e9636

[128] GRUVER, J. S. ; POTDAR, A. A. ; JEON, J. ; SAI, J. ; ANDERSON, B. ; WEBB, D. ; RICHMOND, A. ; QUARANTA, V. ; CUMMINGS, P. T. ; CHUNG, C. Y.: Bimodal analysis reveals a general scaling law governing nondirected and chemotactic cell motility. In: *Biophys. J.* 99 (2010), 2, 367–76

[129] METZNER, C. ; MARK, C. ; STEINWACHS, J. ; LAUTSCHAM, L. ; STADLER, F. ; FABRY, B.: Superstatistical analysis and modelling of heterogeneous random walks. In: *Nat. Commun.* 6 (2015), 7516

[130] GRANER, F. ; GLAZIER, J. A.: Simulation of biological cell sorting using a two-dimensional extended Potts model. In: *Phys. Rev. Lett.* 69 (1992), 13, 2013

[131] GLAZIER, J. A. ; GRANER, F.: Simulation of the differential adhesion driven rearrangement of biological cells. In: *Phys. Rev. E* 47 (1993), 3, 2128

[132] MARÉE, A. F. ; JILKINE, A. ; DAWES, A. ; GRIENEISEN, V. A. ; EDELSTEIN-KESHET, L.: Polarization and movement of keratocytes: a multiscale modelling approach. In: *Bull. Math. Biol.* 68 (2006), 5, 1169–211

[133] SZABÓ, A. ; ÜNNEP, R. ; MÉHES, E. ; TWAL, W. O. ; ARGRAVES, W. S. ; CAO, Y. ; CZIRÓK, A.: Collective cell motion in endothelial monolayers. In: *Phys. Biol.* 7 (2010), 4, 046007

[134] KABLA, A. J.: Collective cell migration: leadership, invasion and segregation. In: *J. R. Soc. Interface* 9 (2012), 77, 3268–78

[135] SEGERER, F. J. ; ROTTGERMANN, P. J. ; SCHUSTER, S. ; PIERA ALBEROLA, A. ; ZAHLER, S. ; RADLER, J. O.: Versatile method to generate multiple types of micropatterns. In: *Biointerphases* 11 (2016), 1, 011005

[136] BEAULIEU, I. ; GEISSLER, M. ; MAUZEROLL, J.: Oxygen plasma treatment of polystyrene and Zeonor: substrates for adhesion of patterned cells. In: *Langmuir* 25 (2009), 12, 7169–76

[137] LIM, K.-B. ; LEE, D.-C.: Surface modification of glass and glass fibres by plasma surface treatment. In: *Surf. Interface Anal.* 36 (2004), 3, 254–258

[138] ALAM, A. U. ; HOWLADER, M. M. R. ; DEEN, M. J.: The effects of oxygen plasma and humidity on surface roughness, water contact angle and hardness of silicon, silicon dioxide and glass. In: *J. Micromech. Microeng.* 24 (2014), 3, 035010

[139] HEUBERGER, M. ; DROBEK, T. ; SPENCER, N. D.: Interaction forces and morphology of a protein-resistant poly(ethylene glycol) layer. In: *Biophys. J.* 88 (2005), 1, 495–504

[140] HILLBORG, H. ; ANKNER, J. F. ; GEDDE, U. W. ; SMITH, G. D. ; YASUDA, H. K. ; WIKSTRÖM, K.: Crosslinked polydimethylsiloxane exposed to oxygen plasma studied by neutron reflectometry and other surface specific techniques. In: *Polymer* 41 (2000), 18, 6851–6863

[141] FUARD, D. ; TZVETKOVA-CHEVOLLEAU, T. ; DECOSSAS, S. ; TRACQUI, P. ; SCHIAVONE, P.: Optimization of poly-di-methyl-siloxane (PDMS) substrates for studying cellular adhesion and motility. In: *Microelectron. Eng.* 85 (2008), 5-6, 1289–1293

[142] JENSEN, C. ; GUREVICH, L. ; PATRICIU, A. ; STRUIJK, J. ; ZACHAR, V. ; PENNISI, C. P.: Stable Hydrophilic Polydimethylsiloxane Surfaces Produced by Plasma Treatment for Enhanced Cell Adhesion. In: DREMSTRUP, K. (editor) ; REES, S. (editor) ; JENSEN, M. (editor): *15th Nordic-Baltic Conference on Biomedical Engineering and Medical Physics (NBC 2011): 14-17 June 2011, Aalborg, Denmark.* Berlin, Heidelberg : Springer Berlin Heidelberg, 2011, 105–108

[143] IBIDI: *Labware*. http://ibidi.com/xtproducts/en/ibidi-Labware, 2016

[144] MAHESHWARI, G. ; WELLS, A. ; GRIFFITH, L. G. ; LAUFFENBURGER, D. A.: Biophysical Integration of Effects of Epidermal Growth Factor and Fibronectin on Fibroblast Migration. In: *Biophys. J.* 76 (1999), 5, 2814–2823

[145] RAJAGOPALAN, P. ; MARGANSKI, W. A. ; BROWN, X. Q. ; WONG, J. Y.: Direct comparison of the spread area, contractility, and migration of balb/c 3T3 fibroblasts adhered to fibronectin- and RGD-modified substrata. In: *Biophys. J.* 87 (2004), 4, 2818–27

[146] PHILIPSBORN, A. C. ; LANG, S. ; LOESCHINGER, J. ; BERNARD, A. ; DAVID, C. ; LEHNERT, D. ; BONHOEFFER, F. ; BASTMEYER, M.: Growth cone navigation in substrate-bound ephrin gradients. In: *Development* 133 (2006), 13, 2487–95

[147] LANGMUIR, I.: The adsorption of gases on plane surfaces of glass, mica and platinum. In: *J. Am. Chem. Soc.* 40 (1918), 9, 1361–1403

[148] LATOUR, R. A.: The Langmuir isotherm: a commonly applied but misleading approach for the analysis of protein adsorption behavior. In: *J. Biomed. Mater. Res. A* 103 (2015), 3, 949–58

[149] ZENGEL, P. ; NGUYEN-HOANG, A. ; SCHILDHAMMER, C. ; ZANTL, R. ; KAHL, V. ; HORN, E.: μ-Slide Chemotaxis: A new chamber for long-term chemotaxis studies. In: *BMC Cell Biol.* 12 (2011), 1, 1–14

[150] IBIDI: *sticky-Slide Chemotaxis*. http://ibidi.com/xtproducts/en/ibidi-Labware/sticky-Slides/sticky-Slide-Chemotaxis, 2015

[151] KRAMER, J.: *Herstellung von Proteingradienten auf mikrostrukturierten Oberflächen*, Ludwig-Maximilians-Universität München, Bachelor thesis, 2015

[152] JUNKER, J. L. ; HEINE, U. I.: Effect of Adhesion Factors Fibronectin, Laminin, and Type IV Collagen on Spreading and Growth of Transformed and Control Rat Liver Epithelial Cells. In: *Cancer Res.* 47 (1987), 14, 3802–3807

[153] TOMASELLI, K. J. ; DAMSKY, C. H. ; REICHARDT, L. F.: Interactions of a neuronal cell line (PC12) with laminin, collagen IV, and fibronectin: identification of integrin-related glycoproteins involved in attachment and process outgrowth. In: *J. Cell Biol.* 105 (1987), 5, 2347–58

[154] VROMAN, L. ; ADAMS, A. ; FISCHER, G. ; MUNOZ, P.: Interaction of high molecular weight kininogen, factor XII, and fibrinogen in plasma at interfaces. In: *Blood* 55 (1980), 1, 156–159

[155] ERAT, M. C. ; SLADEK, B. ; CAMPBELL, I. D. ; VAKONAKIS, I.: Structural analysis of collagen type I interactions with human fibronectin reveals a cooperative binding mode. In: *J. Biol. Chem.* 288 (2013), 24, 17441–50

[156] KUBOW, K. E. ; VUKMIROVIC, R. ; ZHE, L. ; KLOTZSCH, E. ; SMITH, M. L. ; GOURDON, D. ; LUNA, S. ; VOGEL, V.: Mechanical forces regulate the interactions of fibronectin and collagen I in extracellular matrix. In: *Nat. Commun.* 6 (2015), 8026

[157] CARLSSON, R. ; ENGVALL, E. ; FREEMAN, A. ; RUOSLAHTI, E.: Laminin and fibronectin in cell adhesion: enhanced adhesion of cells from regenerating liver to laminin. In: *Proc. Natl. Acad. Sci. USA* 78 (1981), 4, 2403–2406

[158] CLYMAN, R. I. ; MCDONALD, K. A. ; KRAMER, R. H.: Integrin receptors on aortic smooth muscle cells mediate adhesion to fibronectin, laminin, and collagen. In: *Circ. Res.* 67 (1990), 1, 175–86

[159] MORALES, D. E. ; MCGOWAN, K. A. ; GRANT, D. S. ; MAHESHWARI, S. ; BHARTIYA, D. ; CID, M. C. ; KLEINMAN, H. K. ; SCHNAPER, H. W.: Estrogen Promotes Angiogenic Activity in Human Umbilical Vein Endothelial Cells In Vitro and in a Murine Model. In: *Circulation* 91 (1995), 3, 755–763

[160] ZARIC, J. ; RUEGG, C.: Integrin-mediated adhesion and soluble ligand binding stabilize COX-2 protein levels in endothelial cells by inducing expression and preventing degradation. In: *J. Biol. Chem.* 280 (2005), 2, 1077–85

[161] RÖTTGERMANN, P. J. F. ; ALBEROLA, A. P. ; RÄDLER, J. O.: Cellular self-organization on micro-structured surfaces. In: *Soft Matter* 10 (2014), 14, 2397–404

[162] SHARMA, S. ; JOHNSON, R. W. ; DESAI, T. A.: Evaluation of the Stability of Nonfouling Ultrathin Poly(ethylene glycol) Films for Silicon-Based Microdevices. In: *Langmuir* 20 (2004), 2, 348–356

[163] PASCHE, S. ; DE PAUL, S. M. ; VÖRÖS, J. ; SPENCER, N. D. ; TEXTOR, M.: Poly(l-lysine)-graft-poly(ethylene glycol) Assembled Monolayers on Niobium Oxide Surfaces: A Quantitative Study of the Influence of Polymer Interfacial Architecture on Resistance to Protein Adsorption by ToF-SIMS and in Situ OWLS. In: *Langmuir* 19 (2003), 22, 9216–9225

[164] WU, S. ; WELLS, A. ; GRIFFITH, L. G. ; LAUFFENBURGER, D. A.: Controlling multipotent stromal cell migration by integrating “course-graining” materials and “fine-tuning” small molecules via decision tree signal-response modeling. In: *Biomaterials* 32 (2011), 30, 7524–7531

[165] *Associated Movies.* Movies are available at http://www.softmatter.physik.uni-muenchen.de/_assets/dissertation_segerer (see end of the bibliography for corresponding QR code) or in the attachment of this file. Movies concerning Chapter 4 and Chapter 5 are also available in the supplementary materials of References [36] and [38], respectively.

[166] ARCIZET, D. ; CAPITO, S. ; GORELASHVILI, M. ; LEONHARDT, C. ; VOLLMER, M. ; YOUSSEF, S. ; RAPPL, S. ; HEINRICH, D.: Contact-controlled amoeboid motility induces dynamic cell trapping in 3D-microstructured surfaces. In: *Soft Matter* 8 (2012), 5, 1473–1481

[167] TAYLOR, W. A.: *Change-Point Analysis: A Powerful New Tool For Detecting Changes.* http://www.variation.com/cpa/tech/changepoint.html, 2000

[168] KASS-HOUT, T. A. ; XU, Z. ; MCMURRAY, P. ; PARK, S. ; BUCKERIDGE, D. L. ; BROWNSTEIN, J. S. ; FINELLI, L. ; GROSECLOSE, S. L.: Application of change point analysis to daily influenza-like illness emergency department visits. In: *J. Am. Med. Inform. Assoc.* 19 (2012), 6, 1075–81

[169] BISAI, D. ; CHATTERJEE, S. ; KHAN, A. ; BARMAN, N. K.: Statistical Analysis of Trend and Change Point in Surface Air Temperature Time Series for Midnapore Weather Observatory, West Bengal, India. In: *Hydrol.: Curr. Res.* 5 (2014), 2157-7587

[170] GEIGER, B. ; SPATZ, J. P. ; BERSHADSKY, A. D.: Environmental sensing through focal adhesions. In: *Nat. Rev. Mol. Cell Biol.* 10 (2009), 1, 21–33

[171] SHEMESH, T. ; VERKHOVSKY, A. B. ; SVITKINA, T. M. ; BERSHADSKY, A. D. ; KOZLOV, M. M.: Role of focal adhesions and mechanical stresses in the formation and progression of the lamellipodium-lamellum interface [corrected]. In: *Biophys. J.* 97 (2009), 5, 1254–64

[172] BREINIG, M. ; KLEIN, F. A. ; HUBER, W. ; BOUTROS, M.: A chemical-genetic interaction map of small molecules using high-throughput imaging in cancer cells. In: *Mol. Syst. Biol.* 11 (2015), 12, 846

[173] POPOWICZ, P. ; ENGEL, G. ; WILKING, N. ; LINDER, S.: Differential-effects of fibroblast coculture on mcf-7 and mda-231 breast-carcinoma cell invasion through matrigel. In: *Oncol. Rep.* 2 (1995), 2, 303–306

[174] THOMPSON, E. W. ; PAIK, S. ; BRÜNNER, N. ; SOMMERS, C. L. ; ZUGMAIER, G. ; CLARKE, R. ; SHIMA, T. B. ; TORRI, J. ; DONAHUE, S. ; LIPPMAN, M. E. ; MARTIN, G. R. ; DICKSON, R. B.: Association of increased basement membrane invasiveness with absence of estrogen receptor and expression of vimentin in human breast cancer cell lines. In: *J. Cell. Physio.* 150 (1992), 3, 534–544

[175] HAYASHI, Y. ; OSANAI, M. ; LEE, G. H.: Fascin-1 expression correlates with repression of E-cadherin expression in hepatocellular carcinoma cells and augments their invasiveness in combination with matrix metalloproteinases. In: *Cancer. Sci.* 102 (2011), 6, 1228–35

[176] KOPP, F. ; HERMAWAN, A. ; OAK, P. S. ; HERRMANN, A. ; WAGNER, E. ; ROIDL, A.: Salinomycin treatment reduces metastatic tumor burden by hampering cancer cell migration. In: *Mol. Cancer.* 13 (2014), 1, 1–6

[177] BOEHMERLE, W. ; ENDRES, M.: Salinomycin induces calpain and cytochrome c-mediated neuronal cell death. In: *Cell Death. Dis.* 2 (2011), e168

[178] WANG, F. ; HE, L. ; DAI, W.-Q. ; XU, Y.-P. ; WU, D. ; LIN, C.-L. ; WU, S.-M. ; CHENG, P. ; ZHANG, Y. ; SHEN, M. ; WANG, C.-F. ; LU, J. ; ZHOU, Y.-Q. ; XU, X.-F. ; XU, L. ; GUO, C.-Y.: Salinomycin Inhibits Proliferation and Induces Apoptosis of Human Hepatocellular Carcinoma Cells In Vitro and In Vivo. In: *PLoS ONE* 7 (2012), 12, e50638

[179] EVANS, J. H. ; FALKE, J. J.: Ca2+ influx is an essential component of the positive-feedback loop that maintains leading-edge structure and activity in macrophages. In: *Proc. Natl. Acad. Sci. USA* 104 (2007), 41, 16176–81

[180] WEI, C. ; WANG, X. ; CHEN, M. ; OUYANG, K. ; SONG, L. S. ; CHENG, H.: Calcium flickers steer cell migration. In: *Nature* 457 (2009), 7231, 901–5

[181] KIM, J. M. ; LEE, M. ; KIM, N. ; HEO, W. D.: Optogenetic toolkit reveals the role of Ca2+ sparklets in coordinated cell migration. In: *Proc. Natl. Acad. Sci. USA* 113 (2016), 21, 5952–5957

[182] LEI, Y. ; ZOUANI, O. F. ; REMY, M. ; AYELA, C. ; DURRIEU, M. C.: Geometrical microfeature cues for directing tubulogenesis of endothelial cells. In: *PLoS ONE* 7 (2012), 7, e41163

[183] KOVACS, M. ; TOTH, J. ; HETENYI, C. ; MALNASI-CSIZMADIA, A. ; SELLERS, J. R.: Mechanism of blebbistatin inhibition of myosin II. In: *J. Biol. Chem.* 279 (2004), 34, 35557–63

[184] LIMOUZE, J. ; STRAIGHT, A. F. ; MITCHISON, T. ; SELLERS, J. R.: Specificity of blebbistatin, an inhibitor of myosin II. In: *J. Muscle Res. Cell. Motil.* 25 (2004), 4, 337–341

[185] ISHIHARA, H. ; OZAKI, H. ; SATO, K. ; HORI, M. ; KARAKI, H. ; WATABE, S. ; KATO, Y. ; FUSETANI, N. ; HASHIMOTO, K. ; UEMURA, D.: Calcium-independent activation of contractile apparatus in smooth muscle by calyculin-A. In: *J. Pharm. Exp. Ther.* 250 (1989), 1, 388–396

[186] FABIAN, L. ; TROSCIANCZUK, J. ; FORER, A.: Calyculin A, an enhancer of myosin, speeds up anaphase chromosome movement. In: *Cell Chromosome* 6 (2007), 1

[187] KRAWETZ, R. J. ; TAIANI, J. ; GREENE, A. ; KELLY, G. M. ; RANCOURT, D. E.: Inhibition of Rho Kinase Regulates Specification of Early Differentiation Events in P19 Embryonal Carcinoma Stem Cells. In: *PLoS ONE* 6 (2011), 11, e26484

[188] RIETDORF, J. ; SIEGERT, F. ; WEIJER, C. J.: Analysis of Optical Density Wave Propagation and Cell Movement during Mound Formation inDictyostelium discoideum. In: *Dev. Biol.* 177 (1996), 2, 427–438

[189] TANNER, K. ; MORI, H. ; MROUE, R. ; BRUNI-CARDOSO, A. ; BISSELL, M. J.: Coherent angular motion in the establishment of multicellular architecture of glandular tissues. In: *Proc. Natl. Acad. Sci. USA* 109 (2012), 6, 1973–8

[190] DOMBROWSKI, C. ; CISNEROS, L. ; CHATKAEW, S. ; GOLDSTEIN, R. E. ; KESSLER, J. O.: Self-concentration and large-scale coherence in bacterial dynamics. In: *Phys. Rev. Lett.* 93 (2004), 9, 098103

[191] BEN-JACOB, E. ; LEVINE, H.: Self-engineering capabilities of bacteria. In: *J. R. Soc. Interface* 3 (2006), 6, 197–214

[192] WIOLAND, H. ; WOODHOUSE, F. G. ; DUNKEL, J. ; KESSLER, J. O. ; GOLDSTEIN, R. E.: Confinement Stabilizes a Bacterial Suspension into a Spiral Vortex. In: *Phys. Rev. Lett.* 110 (2013), 26, 268102

[193] SCHALLER, V. ; WEBER, C. ; SEMMRICH, C. ; FREY, E. ; BAUSCH, A. R.: Polar patterns of driven filaments. In: *Nature* 467 (2010), 7311, 73–7

[194] SUMINO, Y. ; NAGAI, K. H. ; SHITAKA, Y. ; TANAKA, D. ; YOSHIKAWA, K. ; CHATE, H. ; OIWA, K.: Large-scale vortex lattice emerging from collectively moving microtubules. In: *Nature* 483 (2012), 7390, 448–52

[195] NARAYAN, V. ; RAMASWAMY, S. ; MENON, N.: Long-Lived Giant Number Fluctuations in a Swarming Granular Nematic. In: *Science* 317 (2007), 5834, 105–108

[196] KUDROLLI, A. ; LUMAY, G. ; VOLFSON, D. ; TSIMRING, L. S.: Swarming and Swirling in Self-Propelled Polar Granular Rods. In: *Phys. Rev. Lett.* 100 (2008), 5, 058001

[197] SHIBAZAKI, Y. ; SHIMIZU, M. ; KURODA, R.: Body handedness is directed by genetically determined cytoskeletal dynamics in the early embryo. In: *Curr. Biol.* 14 (2004), 16, 1462–7

[198] EDWARDS, W. ; MOLES, A. T. ; FRANKS, P.: The global trend in plant twining direction. In: *Glob. Ecol. Biogeogr.* 16 (2007), 6, 795–800

[199] Levin, M.: Left-right asymmetry in embryonic development: a comprehensive review. In: *Mech. Dev.* 122 (2005), 1, 3–25

[200] Wan, L. Q. ; Ronaldson, K. ; Park, M. ; Taylor, G. ; Zhang, Y. ; Gimble, J. M. ; Vunjak-Novakovic, G.: Micropatterned mammalian cells exhibit phenotype-specific left-right asymmetry. In: *Proc. Natl. Acad. Sci. USA* 108 (2011), 30, 12295–12300

[201] Chen, T.-H. ; Hsu, J. J. ; Zhao, X. ; Guo, C. ; Wong, M. N. ; Huang, Y. ; Li, Z. ; Garfinkel, A. ; Ho, C.-M. ; Tintut, Y. ; Demer, L. L.: Left-Right Symmetry Breaking in Tissue Morphogenesis via Cytoskeletal Mechanics. In: *Circ. Res.* 110 (2012), 4, 551–559

[202] Tee, Y. H. ; Shemesh, T. ; Thiagarajan, V. ; Hariadi, R. F. ; Anderson, K. L. ; Page, C. ; Volkmann, N. ; Hanein, D. ; Sivaramakrishnan, S. ; Kozlov, M. M. ; Bershadsky, A. D.: Cellular chirality arising from the self-organization of the actin cytoskeleton. In: *Nat. Cell Biol.* 17 (2015), 4, 445–57

[203] Thüroff, F. P.: *Collective motion in active matter*, Ludwig-Maximilians-Universität München, Dissertation, 2014

[204] Thüroff, F. ; Reiter, M. ; Frey, E.: Bridging the gap between single cell migration and collective dynamics. In: *Submitted for Publication*

[205] Lara Rodriguez, L. ; Schneider, I. C.: Directed cell migration in multi-cue environments. In: *Integr. Biol.* 5 (2013), 11, 1306–1323

[206] Théry, M. ; Pepin, A. ; Dressaire, E. ; Chen, Y. ; Bornens, M.: Cell distribution of stress fibres in response to the geometry of the adhesive environment. In: *Cytoskeleton* 63 (2006), 6, 341–55

[207] Etienne-Manneville, S. ; Hall, A.: Integrin-Mediated Activation of Cdc42 Controls Cell Polarity in Migrating Astrocytes through PKCξ. In: *Cell* 106 (2001), 4, 489–498

[208] Gomes, E. R. ; Jani, S. ; Gundersen, G. G.: Nuclear movement regulated by Cdc42, MRCK, myosin, and actin flow establishes MTOC polarization in migrating cells. In: *Cell* 121 (2005), 3, 451–63

[209] Dembo, M. ; Wang, Y.-L.: Stresses at the Cell-to-Substrate Interface during Locomotion of Fibroblasts. In: *Biophys. J.* 76 (1999), 4, 2307–2316

[210] Roure, O. du ; Saez, A. ; Buguin, A. ; Austin, R. H. ; Chavrier, P. ; Siberzan, P. ; Ladoux, B.: Force mapping in epithelial cell migration. In: *Proc. Natl. Acad. Sci. USA* 102 (2005), 7, 2390–2395

[211] ABRAMOFF, M. ; MAGALHAES, P. ; RAM, S.: Image Processing with ImageJ. In: *Biophotonics Int.* 11 (2004), 7, 36–42

[212] YOUSSEF, S. ; GUDE, S. ; RADLER, J. O.: Automated tracking in live-cell time-lapse movies. In: *Integr. Biol.* 3 (2011), 11, 1095–101

[213] MATLAB: *version 7.11.1 (R2010b)*. 7.11.1. Natick, Massachusetts, United States : The MathWorks Inc., 2010

[214] PONS DOMENECH, A.: *Tracking cells in confined enviroments*, Ludwig-Maximilians-Universität München, Bachelor thesis, 2012

[215] STROUSTRUP, B.: *The C++ Programming Language*. Addison-Wesley Longman Publishing Co., Inc., 2000. – 1040 S.

[216] BUHL, J. ; SUMPTER, D. J. ; COUZIN, I. D. ; HALE, J. J. ; DESPLAND, E. ; MILLER, E. R. ; SIMPSON, S. J.: From disorder to order in marching locusts. In: *Science* 312 (2006), 5778, 1402–6

Movies available at:
(see also Ref. [165])

DANKSAGUNG

An dieser Stelle will ich mich nochmal herzlichst bei allen die zur Entstehung dieser Arbeit und zur guten Zeit die ich am Lehrstuhl Rädler hatte beigetragen haben bedanken. Insbesondere gilt mein Dank **Joachim O. Rädler** für seine Unterstützung sowie seine Begeisterungsfähigkeit und positive Art, die sowohl die fachlichen Diskussionen angenehm und interessant gestaltet haben, als auch maßgeblich zur guten Atmosphäre am Lehrstuhl beigetragen haben. Ich danke auch **Erwin Frey** für die angenehme Kooperation, die Beiträge und Anregungen und nicht zuletzt die gut gestalteten Vorlesungen durch die mein Interesse an der Biophysik mitbegründet wurde. **Florian Thüroff** und **Simon Schuster** danke ich für die gute Zusammenarbeit und viele ergiebige Diskussionen. Den Kollegen und Organisatoren im **MGK-Programm** des SFB 1032 danke ich für die oft Augenöffnenden Einblicke in die Arbeitsweisen anderer Lehrstühle und die Top Stimmung auf den Exkursionen und Workshops.

Mein Dank gilt freilich auch ganz besonders dem gesamten **Lehrstuhl Rädler** für die entspannte und spaßige Arbeitsatmosphäre.[1] Dabei besonders **Gerlinde**, den **Susis**, **Max**, **Margarete** und **Andrea** dafür, dass sie den Laden am Laufen halten und für das immer wieder geduldige Erklären der verschiedensten labor- oder verwaltungstechnischen Sachverhalte. Den guten alten Kellerkindern **Silvia, Peter, Manu, Matthias, Andreas, Judith, Elisavet, Michi, Stefan** sowie dem neuen Luxusbüro **Daniel, Jan, David, Philipp, Philip[2]** und **Sonja**[3] danke ich für die gute Stimmung in Untergrund und Obergeschoss und das Ertragen der gelegentlich vielleicht etwas lautstarken Arbeitsatmosphäre. Meinen Bachelors **Thomas, Arnau, Björn** und **Jonas** fürs Aushalten meiner "Betreuerqualitäten" und die angenehme Zusammenarbeit. Selbiges gilt insbesondere auch für meinen früheren Masterzögling und späteren Kollegen **Christoph**, der zusätzlich noch durchs Einspringen bei Vorträgen und das Teamwork bei fachlichen Überzeugungsarbeiten geglänzt hat. Den eifrigen Korrekturlesern **Peter[4], Sonja, Kathi[5]** und der **Kommissarin Löwenherz**[6] für Inhaltlichen Input und das Ausbügeln der schlimmsten Patzer. Dem **Team Bumsibär** danke ich für zahlreiche "informal discussions" (freilich alle nach Feierabend!) und nicht zuletzt die Polonaise.

Vor allem gilt mein Dank auch meinen **Freunden** die immer mit einem mehr als ausreichenden Maß an Ausgleich zum Unialltag aufwarten konnten, meiner **Familie** und insbesondere meiner **Mutter**, deren Unterstützung in allen Lebenslagen mich auch im Laufe des letzten Jahre gut durch die stressigeren Phasen dieser Arbeit geleitet hat.

---

[1] Ausdrücklich ausgenommen sind hierbei diejenigen oder derjenige, die mir auf bösartige Weise Kuchenplatte, Weißbierglas, mindestens 3 Salatschüsseln und quasi alle meine Kugelschreiber entwendet haben.

[2] Der mein Ego immer wieder durch sportliche Wettkämpfe und das zur Schau Stellen lustiger Fitkurven aufgebaut hat.

[3] Auch für die Oberaktiven Pausen, die immer gefüllte Süßigkeitenschublade und die Taschentücher.

[4] Der diese Aufgabe trotz seiner offiziell bestätigten sprachlichen Defizite auf sich genommen hat.

[5] Die dafür gesorgt hat, dass mir auch die letzte Zeit des Zusammenschreibens immer in besonders angenehmer Erinnerung bleiben wird.

[6] Deren Unterstützung in den letzten Jahren zur Lösung so manch verzwickten Falls beigetragen hat.

Mit folgender Unterschrift erkläre ich, dass ich die vorliegende Arbeit selbständig verfasst, sowie keine anderen als die angegebenen Quellen und Hilfsmittel benutzt habe.

München, den 30. Juni 2016

Felix Segerer